UNIVERSIDAD NACIONAL DE GENERAL SAN MARTÍN

COMISIÓN NACIONAL DE ENERGÍA ATÓMICA

INSTITUTO DE TECNOLOGÍA

“Prof. Jorge A. Sábato”

Termoelectricidad cuántica y fenómenos de transporte en nanoestructuras topológicas [(*)]

por Lic. Daniel Matías Gresta

Director

Prof. Dra. Liliana Arrachea

Prof. Dra. Alejandra Tonina

[(*)] Tesis para optar al título de Doctor en Ciencia y Tecnología mención Física

República Argentina

2021

UNIVERSIDAD NACIONAL DE GENERAL SAN MARTÍN

COMISIÓN NACIONAL DE ENERGÍA ATÓMICA

INSTITUTO DE TECNOLOGÍA

“Prof. Jorge A. Sábato”

Quantum thermoelectricity and transport phenomena in topological nanostructures [(*)]

by Lic. Daniel Matías Gresta

Advisors

Prof. Dra. Liliana Arrachea

Prof. Dra. Alejandra Tonina

[(*)] Thesis submitted for the degree of Doctor in Science and Technology, Physics

República Argentina

2021

Resumen

En las últimas décadas, el estudio de materiales topológicos se volvió uno de los temas más relevantes en física de materia condensada. Los sistemas son clasificados de acuerdo a un invariante topológico además de las simetrías que poseen y sus propiedades permanecen robustas ante perturbaciones o desorden. Entender tales estados topológicos puede llevar a un próspero camino para una nueva generación de materiales con aplicaciones que abarcan desde metrología cuántica a computación cuántica e inteligencia artificial. Esta tesis doctoral presenta un estudio de los fenómenos térmicos y termoeléctricos que se desarrollan en tres nanoestructuras topológicas.

El primer dispositivo en consideración es una estructura Corbino en el régimen de Hall cuántico. Presentamos un análisis teórico junto con mediciones experimentales. La medición del termovoltaje es cualitativa y cuantitativamente modelada sobre la base de mediciones independientes de la conductividad eléctrica, indicando que los mecanismos de transporte se originan predominantemente en la difusión electrónica. Implementamos una descripción de los coeficientes de Onsager basado en una única función de transmisión, de la cual ambos, termovoltaje y conductividad eléctrica, pueden ser predichos con un solo parámetro de ajuste. Aún más, pudimos predecir grandes valores de la figura de mérito para la eficiencia como una máquina térmica o de enfriado en los niveles de Landau parcialmente llenos. Los resultados de este trabajo fueron publicados en el paper 1 de la lista.

En el segundo dispositivo en consideración, se estudiaron las propiedades termoeléctricas de los pares de Kramers helicoidales en el estado de borde de un aislante topológico en el régimen de spin Hall cuántico. Los estados de borde se encuentran acoplados a un nanomagneto con un componente de la magnetización perpendicular a la dirección de la interacción spin-órbita del material. Mostramos que la función de transmisión de este dispositivo tiene las propiedades deseadas para alcanzar la óptima performance en el régimen cuántico coherente. Para un solo dominio, la potencia generada es casi la máxima alcanzable. Si un segundo dominio se agrega con diferente orientación, la función de transmisión tiene una resonancia. Su origen se debe a que el sistema pasa a una nueva fase topológica albergando un solitón de Jackiw-Rebbi. Proveemos también estimaciones para la fabricación de este dispositivo con un pozo cuántico topológico en HgTe. Los resultados de este trabajo fueron publicados en el paper 2 de la lista.

Finalmente, estudiamos el transporte térmico cuando se le agregan contactos superconductores al sistema anterior. Mostramos que la conductancia térmica es muy sensible a la presencia de una resonancia de Jackiw-Rebbi, a diferencia de la corriente Josephson o el espectro de Andreev. Se presenta un detallado análisis de estas propiedades en el caso de uno y dos dominios magnéticos. Las configuraciones que alberguen un solitón magnético conllevan a un comportamiento peculiar en la conductancia térmica relativa al cuanto térmico, caracterizada por un valor negativo en la pendiente como función de la temperatura, justo por encima de la temperatura crítica del superconductor. Los resultados de este trabajo fueron publicados en el paper 3 de la lista.

Abstract

In the last decades, the study of topological materials became one of the most relevant topics of condensed matter physics. Systems are classified according to a topological invariant in addition to the symmetries and their properties remain robust under perturbation or disorder. Understanding such topological states of matter may lead to an affluent path for a new generation of quantum devices, with applications ranging from quantum metrology to quantum computation and AI. This doctoral thesis presents a study of thermal and thermoelectrical phenomena that develops in three topological nanoestructures.

The first device under consideration is a Corbino structure in the quantum Hall regime. We present a theoretical analysis together with experimental measurements. The measured thermoelectric voltage is qualitatively and quantitatively modeled on the basis of the data recorded from independent measurements of the conductivity. This is consistent with a transport mechanism dominated by electron diffusion. We implement a description of the Onsager coefficients based on a single transmission function, from which both thermovoltage and conductivity can be predicted with a single fitting parameter. Furthermore, we predict a large figure of merit for the efficiency of the thermoelectric performance for the partially filled Landau levels and high magnetic fields. The results of this work were published in paper 1 of the list.

Secondly, we study the thermoelectric properties of a Kramers' pair of helical edge states of a topological insulator in the quantum spin Hall regime. The edge states are coupled to a nanomagnet with a component of the magnetization perpendicular to the direction of the spin-orbit coupling interaction of the host. We show that the transmission function of this device has the desired qualities for optimal thermoelectric performance in the quantum coherent regime. For a single magnetic domain, there is a power generation close to the optimal bound. When a second magnet with different orientation is added, the transmission function has a resonance. Its origin is due to the system transitions to a topological phase hosting a Jackiw-Rebbi soliton. We provide estimates for the fabrication of this device with HgTe quantum-well topological insulator. The results of this work were published in paper 2 of the list.

Finally, we study the thermal transport when two superconducting leads are added to the previous device. We show that the thermal conductance turns out to be very sensitive to the presence of Jackiw-Rebbi resonance, unlike the Josephson current or the Andreev spectrum. A detailed analysis of these properties in the case of a single and two magnetic domains is presented. Configurations hosting solitonic magnetic modes lead to a peculiar behavior of the thermal conductance relative to the thermal quantum, characterized by a negative slope as a function of the temperature, just above the superconducting critical temperature. The results of this work were published in paper 3 of the list.

Dedication and acknowledgements

Thanks to my family, friends, colleagues and advisors who helped me during this years.

List of published papers

The main results of this thesis were published in the following papers

1. Real M., Gresta D., Reichl C., Weis J., Tonina A., Giudici P., Arrachea L., Wegscheider W., and Dietsche W.: " Thermoelectricity in Quantum Hall Corbino Structures " *Physical Review Applied* **14** *034019 (2020)*.

2. Gresta D. , Real M. and Arrachea L.: " Optimal thermoelectricity with Quantum Spin Hall edge states " *Physical Review Letters* **123** *186801 (2019)*.

3. Gresta D., Blasi G., Taddei F., Carrega M., Braggio A. and Arrachea, L.: " Signatures of Jackiw-Rebbi resonance in the thermal conductance of topological Josephson junctions with magnetic islands" *Physical Review B* **103** *075439 (2021)*.

They will be referred as paper 1, 2 or 3 of the list.

TABLE OF CONTENTS

List of Figures

Figure **Page**

CHAPTER 1

SYSTEMS UNDER CONSIDERATION

The aim of this thesis is to study the thermal and thermoelectric transport of three topological nanostructures. For sake of clarity, the main characteristics of those systems are introduced in the present section. Two of them belong to the family of the so-called topological insulators. Those are the quantum Hall (QH) presented in Sec.1.2 and the quantum spin Hall (QSH) presented in Sec.1.2. The third system to be considered in this thesis is a hybrid structure consisting of a two-dimensional topological insulator (2DTI) in the quantum spin Hall regime attached to superconducting leads. Therefore, Sec.1.3, is devoted to review some properties of superconductivity. In chapter 2 the main framework that is going to be used in the following chapters is presented.

1.1 Quantum Hall effect

It was first observed by Edwin Hall in 1879 that when electrons are constrained in a two-dimensional system and in presence of a magnetic field, there exists a voltage drop, V_{xy}, perpendicular to the direction of the applied current, as shown in Fig. 1.1(a). In 1980, Klaus von Klitzing discovered that under conditions such as low temperature and high magnetic field, the resistance associated to $V_{x,y}$ is quantized [1, 2], that is

$$R_H = \frac{V_{x,y}}{J} = \frac{h}{\vartheta e^2} = \frac{1}{\vartheta} 25\,812.807\ \Omega, \tag{1.1}$$

where e is the electron charge, h is the Plank constant and ϑ can be integer or fractional number, hence defining the Integer Quantum Hall Effect (IQHE) or Fractional Quantum Hall Effect (FQHE). A typical measurement of the Hall resistance performed in this case by Instituto Nacional de Tecnología Industrial, Argentina, is presented in Fig.1.1(b).

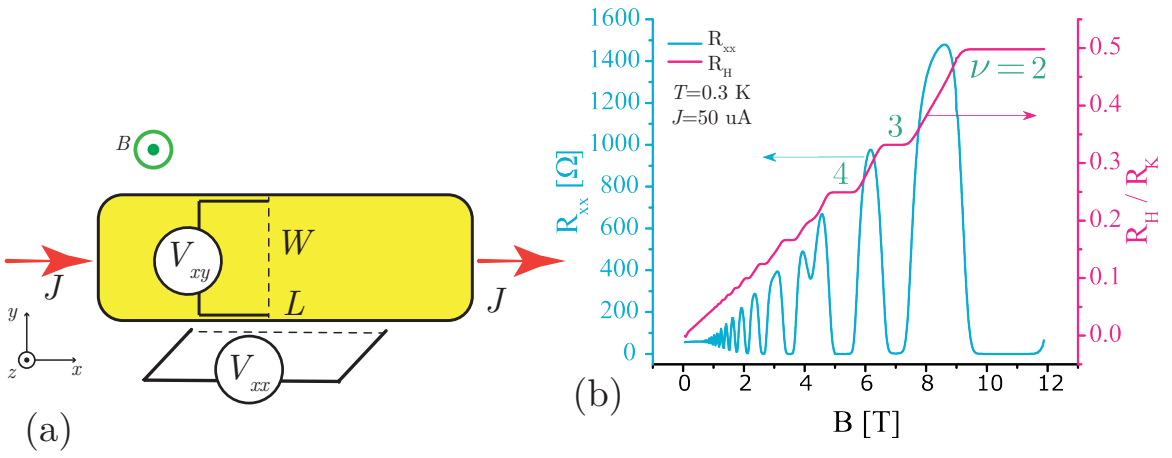

Figure 1.1: A 2DES is polarized with a current J a long its longitudinal direction in presence of a magnetic field B perpendicular to the sample. Then one can measure the voltage drop at a distance L in the longitudinal direction, V_{xx} or at a distance W in the transverse direction.

We can see that when R_H is constant, it corresponds to a value of ϑ. At the same time, R_{xx} goes to zero and has a peak when a change in the value of ϑ occurs. It was also demonstrated both, theoretically and experimentally that it is a very robust effect [3–8]. This turns out to be a consequence of the topological nature of the QHE [9–12]. It is because of this that in 2018 the International Committe for Weights and Measures (CIPM) adopted the value of the von Klitzing constant $R_K = 25\,812.807\,459\,3045\Omega$ as the standard unit for electrical measurements by fixing the value of e and h[13, 14]. The discovery of the QHE has led to a plethora of developments and physics [15–19]. In this section some properties of the IQHE will be reviewed and some useful concepts will be introduced.

1.1.1 Landau levels

We start by reviewing the solution of an 2DES in the presence of a perpendicular magnetic field. It is well known that an electron will go around circular orbits due to the Lorentz force, with a radius $r \propto \sqrt{1/B}$ and the cyclotron frequency, $\omega_C = eB/m$, with e being the electron charge, m its mass and B the magnetic field.

To describe this phenomenon, it is convenient to use a Hamiltonian in the Landau gauge, that is, the potential vector $\vec{A} = xB\check{y}$,

$$H = \frac{1}{2m}\left(p_x^2 + \left(p_y - eBx\right)^2\right).$$

Note that this Hamiltonian does not depend on y. Therefore, it commutes with the associated momentum allowing to choose $p_y = \hbar k$ as a good quantum number. The effective 1D Hamiltonian is

$$H = \frac{1}{2m}\left(p_x^2 + (\hbar k - eBx)^2\right). \tag{1.2}$$

This turns out to be the Hamiltonian of the harmonic oscillator centered in $x_0 = k\frac{\hbar}{eB}$. The wave function is

$$\Psi_{n,k} \propto e^{iky} H_n(x+x_0) e^{-(x+x_0)^2/2x_0^2},$$

where H_n are the Hermite polynomials while the eigenenergies are

$$E_n = \hbar\omega_c \left(n + \frac{1}{2}\right). \tag{1.3}$$

These quantized energy levels of electrons in a magnetic field are called Landau levels. Note that the spectrum is totally degenerated because the Landau levels do not depend on k.

If an electric field, proportional to the $\check{x}$ direction is turned on, so that the potential becomes $V = -eEx$, the Hamiltonian becomes

$$H = p_x^2 + (\hbar k - eBx)^2 - eEx.$$

The solution is similar to the previous situation but with shifted argument $\Psi = \Psi_{n,k}(x + mE/eB^2, y)$, and a shift in the eigenenergies

$$E_{n,k} = E_n - eE\left(kx_0 + \frac{eE}{m\omega_C^2}\right) + \frac{m}{2}\frac{E^2}{B^2}. \tag{1.4}$$

Note that the degeneracy has been lifted because now each level depends linearly on k. Due to this dependence, the states are drifted in the $\check{y}$ direction. Its group velocity is $v_y = \frac{1}{\hbar}\frac{\partial E_{n,k}}{\partial k} = -\frac{E}{B}$. In other words, turning a magnetic field in $\check{z}$ and an electric field in $\check{x}$ makes the electron to move in a direction perpendicular to both, in this case $\check{y}$. This can be also interpreted as follows. The wave function $\Psi_{n,k}$ is localized at $x = x_0 - eR/m\omega_C^2$ and it moves with momentum k, a potential energy $-eE\left(kx_0 + \frac{eE}{m\omega_C^2}\right)$ and a kinetic energy in the $\check{y}$ direction $\frac{1}{2}mv_y^2 = \frac{m}{2}\frac{E^2}{B^2}$.

To close this section let's compute the current. Recall that it is given by the expectation value of the velocity times the electric charge, that is

$$\vec{I} = \frac{e}{m}\sum \left\langle \Psi_{n,k} \left| \left(\vec{p} - e\vec{A}\right) \right| \Psi_{n,k} \right\rangle, \tag{1.5}$$

where the summation is over all the filled states i.e.: $1 \le n \le \nu$ and all the possible momenta k. Recalling that $p_x = -i\hbar\partial_x$, the $x-$ component of the current is

$$I_x = -\frac{e}{m}\sum_{n=1}^{\nu}\sum_k \left\langle \Psi_{n,k} \left| p_x \right| \Psi_{n,k} \right\rangle = 0. \tag{1.6}$$

The summation gives zero due to the orthogonality of the eigenfunctions. On the other hand, the $y-$ component gives

$$I_y = -\frac{e}{m}\sum_{n=1}^{\nu}\sum_k \left\langle \Psi_{n,k} \left| p_y \right| \Psi_{n,k} \right\rangle = -\frac{e}{m}\sum_{n=1}^{\nu}\sum_k \left\langle \Psi_{n,k} \left| \hbar k + eBx \right| \Psi_{n,k} \right\rangle = e\nu\sum_k \frac{E}{B}. \tag{1.7}$$

where the sum over k gives the number of electrons in the sample i.e.: AB/Φ_0 with $\Phi_0 = h/e$, the quantum of flux and A being the area. The density current per unit of area is

$$J_y = e\nu\frac{E_x}{\Phi_0}.$$

Note that despite applying an electric field in the $\check{x}$ direction, there is no current in that direction, while there is in the perpendicular direction, as long as the system is in a Landau level. This explains the plateaus of the pink curve in the Fig. 1.1.

1.1.2 Edge modes and disorder

In this section we will discuss the existence of edge modes in addition to the Landau levels in the bulk. The edges can be modeled as a well-potential that grows very fast at the end of the sample. In order to use some of the arguments presented before and for sake of simplicity it will be considered a finite size sample only in the $\check{x}$ direction. The profile is shown in Fig. 1.2(a). The Hamiltonian is

$$H = \frac{1}{2m}\left[p_x^2 + \left(p_y + eBx\right)^2\right] + V(x). \tag{1.8}$$

If the potential is smooth, it can be Taylor-expanded around the center of the orbit of the eigenfunction,$V(x) \simeq V(X) + \partial V/\partial x(x - X)$ with X being the center of the orbit. The constant term can be neglected, and higher order terms were dropped off. Under these reasonable considerations, it is obtained the same problem as before but now, the drift velocity is given by

$$v_y = -\frac{1}{eB}\frac{\partial V}{\partial x},$$

This means that each wavefunction, labelled by momentum k, sits at a different x position, $x = -kx_0$ and has a different drift velocity. In particular, the modes at each edge are both chiral, that is, they can only travel in one direction but in opposite sense at each edge. This is because the derivative has a different sign on each edge.

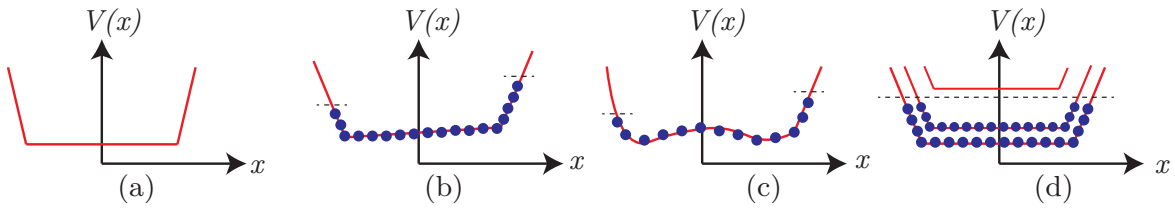

Figure 1.2: Potentials profile to model the edge. (a) Empty level. (b) Filled state up to the Fermi level indicated with dashed line when a chemical potential is applied. (c) Filled state up to the Fermi level when a chemical potential is applied but with a random profile for the bulk. (d) Many states filled up to the Fermi level.

We now introduce a chemical potential. The bulk becomes an insulator when all the states in the band are filled. However, the edge of the material is a conductor. This can be realized by introducing a chemical potential bias, $\Delta\mu$,around the Fermi level on both sides of the sample, for instance, the right hand edge is lifted with respect to the one on the left hand edge, as illustrated in Fig. 1.2(b), indicated with a dashed line, where all the levels are tilted due to the electric field.

The current is, again, the sum over all the filled states, but at this level of approximation this corresponds to the integration over x

$$I_y = -e\int \frac{dk}{2\pi} v_y(k) = \frac{e}{2\pi x_0}\int dx \frac{1}{eB}\frac{\partial V}{\partial x} = \frac{e}{h}\Delta\mu. \tag{1.9}$$

The Hall voltage is $V_H = \Delta\mu/e$, giving the Hall conductivity,

$$\sigma_{x,y} = \frac{I_y}{V_H} = \frac{e^2}{h}, \tag{1.10}$$

which is indeed the expected conductivity for a single Landau level.

The previous calculation holds regardless of the shape of the potential. If it is smooth enough, the conductivity is quantized. The result of Eq. (1.10) holds also even in the presence of a random profile, as depicted in Fig. 1.2(c). The previous argument is easily generalized for n filled levels, as illustrated in Fig. 1.2(d), as long as the Fermi level lies between two of them, giving rise to n chiral modes on each edge.

To end this subsection, we will discuss the disorder in the sample. Samples are naturally dirty, i.e., they have impurities. Such an effect may be modelled by a random potential. General results of perturbation theory [20] show that any generic perturbation, which does not preserve a symmetry breaks any degeneracy. Let's see what happens to a chiral system. Firstly, consider that the potential is smaller than the splitting of the Landau level i.e., $V \ll \hbar\omega_C$. In consequence, the density of states is broadened. Another effect due to disorder is that the states become localized. Here, an extended state is spread throughout the whole system, for instance in the whole edge of the sample. In contrast, a localized state is restricted to lie in some region of space. If, in addition, the potential varies only in scales much greater than the magnetic length $|\nabla V| \ll \hbar\omega_C/l_B$, with $l_B = \sqrt{\frac{\hbar}{eB}}$, the cyclotron orbit of an electron is confined in a region of essentially constant potential. In other words, the center of the orbit will drift along an equipotential. This means that, in a random potential with several minima and maxima, some electrons will orbit around them as if they were trapped, they cannot move throughout the sample. It is very rare to have an equipotential going from one side of the sample to another. Hence, electrons far from the edges are localized regardless if they are in a minimum or maximum of energy. Only the states close to the center of the band will be extended, therefore the density of states changes from a $\delta-$ profile, green line of Fig. 1.3 to the one depicted in blue lines of the same figure.

This has an impact on the conductivity because only the extended states can transport charge from one side of the sample to the other and the localized get stacked in the bulk orbiting in the equipotential lines. Suppose that all the extended states in a given Landau level are filled. If the magnetic field is decreased keeping the density constant, then each Landau level can accommodate fewer electrons. But rather than going to the next Landau level, the localized states become populated. Since these states can not contribute to the current, the conductivity does not change, leading to the plateaux with constant conductivities over a wide range of magnetic fields, already presented in Fig. 1.1(b). The existence of these localized states explain the broad plateaus

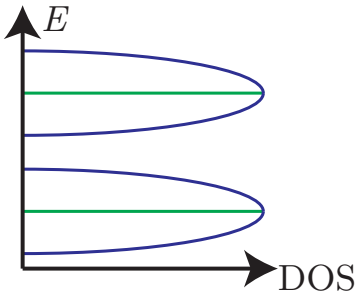

Figure 1.3: Schematic representation of the density of states (DOS) as function of energy. In green line with out disorder, the DOS is a $\delta-$ alike function whereas in blue line with disorder the levels broaden.

of the resistivity at integer filling fractions. Remarkably, this does not invalidate the argument that leads to the result of Eq. 1.10 where it was assumed that all the states contribute equally to the current. Many of those states are localised by impurities and do not transport charge. Hence, the extended states increase the current they carry to compensate for the lack of current transported by the localized states. This ensures that the resistivity remains quantized as Eq. 1.10 despite the presence of disorder. In the following subsection it will be reviewed another argument to show the quantization in the QHE.

1.1.3 Laughlin gedanken experiment: Corbino geometry

The original explanation is due to Laughlin and it was reported in Refs. [21, 22]. Also, the elaboration on the edge states was given by Halperin and is explained in much more detail in Ref. [23]. Laughlin's argument intends to explain the quantization of the conductance at QH state as follows. Let's consider a sample with a circular shape and a magnetic flux perpendicular to it, as depicted in Fig. 1.4. Suppose that a magnetic field is applied and goes through the center of the sample and it varies from 0 to Φ_0. It is turned on very slowly, so that its switching time is much greater than the inverse of ω_C, enabling the system to relax. There is an electromotive force $E = \partial\Phi/\partial t = \Phi_0/T$ in the azimuthal direction. This, in turns, generates a radial current because of the Hall effect. At this point it is customary to rewrite the Hamiltonian in cylindrical coordinates being ϕ the aziumthal coordinate and r the radius. If the particle is at constant radius, then, the only dynamical coordinate is ϕ so that the Hamiltonian is

$$H = \frac{1}{2m}\left(p_\phi + eA_\phi\right)^2 = \frac{1}{2mr^2}\left(-i\hbar\frac{\partial}{\partial\phi} + \frac{e\Phi}{2\pi}\right)^2.$$

The corresponding eigenstates are

$$\Psi_n = \frac{1}{\sqrt{2\pi r}}e^{in\phi}.$$

Solving the Schrödinger time dependent equation, i.e., $H\Psi = E\Psi$, the eigenenergies are

$$E_n = \frac{1}{2mr^2}\left(\hbar n + \frac{e\Phi}{2m}\right) = \frac{\hbar^2}{2mr^2}\left(n + \frac{\Phi}{\Phi_0}\right), \tag{1.11}$$

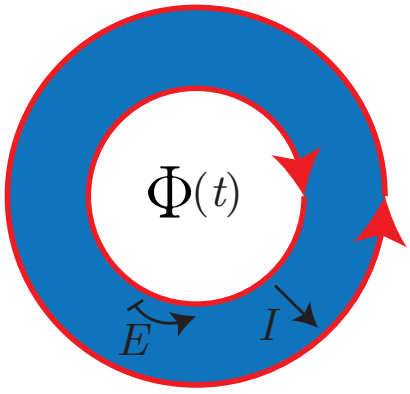

Figure 1.4: Corbino disk in QH state. The edge states are depicted with red arrows, When a magnetic flux $\Phi(t)$ is applied through the center of the sample an azimuthal electric field E is generated which in consequence leads to a radial current I.

with n being an integer. This means that the energy spectrum is shifted in an amount Φ/Φ_0. But when $\Phi/\Phi_0 \in \mathbb{Z}$ the particle goes again to an eigenstate but with the label $n+1$. This can be interpreted as follows. If all the Landau levels are filled, then, a single electron is transferred from the interior edge to the exterior edge as the flux is increased from $\Phi = 0$ to $\Phi = \Phi_0$. If n Landau levels are filled, then, n electrons are transferred from the interior to the exterior. The current is $I = \Delta Q/T = ne$, with ΔQ being the variation of charge and the Hall resistivity is again $\rho_H = E/I_r = h/(e^2 n)$. When the transition between different filling factors happens, a peak in the longitudinal resistance is observed as presented with blue line in Fig 1.1(b).

The robustness of the QHE relies also on other phenomena, this system undergoes on a phase transition to a so-called topological insulator (TI). A TI is a material that is an insulator at the bulk, has conducting states on its edge and its properties remains the same under perturbations or disorder. The QHE belongs to this family, as well as the quantum spin Hall, that will be explained in the next section. If the electrons are non-interacting and the spectrum can be decomposed in bands labeled by a momentum k, as the IQHE, then the system can be assigned a topological number, named the Chern number [11, 24]. And, as long as the potential added to the system does not break any symmetry or generates the closing of the gap, the Chern number remains the same. It can be shown that the Hall conductivity for the IQHE is proportional to the Chern number [11, 24] and it remains constant regardless of the impurities added to the system. More about TI and topological invariant can be found in Refs. [15, 25–28].

1.2 Quantum spin Hall effect

It was recently discovered that another kind of quantum Hall effect could be realized. Firstly, a proposal was done in graphene by Kane and Mele [29] and later by Bernevig and Zhang [30] in semiconductors. In 2D the phase was named the quantum spin Hall effect (QSHE) and, in

contrast to QHE, this effect does not need a magnetic field. Also, the edge states have a distinct property, which is that two states with opposite spin-polarization counter-propagate at a given edge [15, 25, 29, 31–36]. Due to this, they are called helical edge states. The edge states come in Kramers' doublets, and time reversal symmetry ensures the crossing of their energy levels at special points in the Brillouin zone. Because of this energy level crossing, the spectrum of a QSH insulator cannot be adiabatically deformed into that of a topologically trivial insulator without helical edge states. Therefore, in this precise sense, the QSH insulators represent a topologically distinct new state of matter. The topological properties of the QSH state are mathematically characterized by a Z_2 topological invariant [31]. States with an even number of Kramers' pairs of edge states at a given edge are topologically trivial, while those with an odd number are topologically non-trivial. In the following section, we will review this model and why it is different from an insulator or the IQHE explained previously.

1.2.1 The toy model of graphene

In this section we will review the model introduced by Kane and Mele [29, 31] inspired by the possibility of an intrinsic spin Hall effect [37]. The prelude to this proposal was the Hamiltonian proposed by Haldane [38] for the QHE in a lattice model. Their proposal was originally made for graphene but turned out to be unrealistic due to the weak spin-orbit-coupling of that material. Then, this model was revisited by Bernevig et. al. [32] who proposed that the inversion band observed in a HgTe-CdTe heterostructure alloy could host this new phase. This was experimentally verified by König et. al [33, 34]. Most of the ideas presented in this section are from [30–32, 34, 39]. Here is a humble summary that aims to present the model to better understand the forthcoming chapters.

To begin with, let's consider the tight-binding Hamiltonian with time-reversal-invariant spin-orbit interactions,

$$H = t\sum_{\langle i,j\rangle} c_i^\dagger c_j + i\lambda_{SO}\sum_{\langle\langle i,j\rangle\rangle} v_{i,j} c_i^\dagger s_z c_j + \lambda_R \sum_{\langle i,j\rangle} c_i^\dagger \left(\vec{s}\times\vec{d}_{i,j}\right)\Big|_z c_j + \lambda_v \sum_i \xi_i c_i^\dagger c_i. \tag{1.12}$$

The first term is a hopping between the nearest neighbors on the graphene (honeycomb) lattice, being $c_i = \left(c_{i,\uparrow}, c_{i,\downarrow}\right)$. The second term is the mirror-symmetric spin-orbit interaction, which involves spin-dependent second-neighbor hopping. Here $v_{i,j} = \left(\frac{2}{\sqrt{3}}\check{d}_1 \times \check{d}_2\right)\Big|_z = \pm 1$ where $\check{d}_j$ is a unit vector along the two bonds the electron traverses going from site j to i, s_z is the Pauli matrix in the spin space. The third term is a nearest-neighbor Rashba spin-orbit interaction. Note that this term explicitly violates mirror symmetry along $\check{z}$. It naturally arises due to a perpendicular electric field or the interaction with a substrate. The fourth term is a staggered sublattice potential ($\xi_i = \pm 1$) which is included to describe the transition between the QSH phase and the trivial insulator. Notice that this term violates the symmetry under twofold rotations in the plane. The diagonalization of H is straightforward by writing the wave function $\phi_\sigma(\vec{R} + \alpha\vec{d}) = u_{\alpha,\sigma}(\vec{k})e^{i\vec{k}\,\vec{R}}$, being σ its spin, $\vec{R}$ is a Bravais lattice vector built from primitive

vectors $\vec{a}_{1,2} = a/2\left(\sqrt{3}\check{y} \pm \check{x}\right)$, $\alpha = 0,1$ indicates the sublattice index being $\vec{d} = a\check{y}/\sqrt{3}$. Note that for each $\vec{k}$ the Bloch wavefunction is a four-component eigenvector $\left|u(\vec{k})\right\rangle$ of the Bloch Hamiltonian matrix $\mathscr{H}(\vec{k})$. In this way, the Hamiltonian can be rewritten in a more compact form as

$$\mathscr{H}(\vec{k}) = \sum_{a=1}^{5} d_a(\vec{k})\Gamma^a + \sum_{a<b=1}^{5} d_{a,b}(\vec{k})\Gamma^{ab}, \tag{1.13}$$

with

$$\Gamma^i = \left(\sigma^x \otimes \mathbb{1}_{2\times 2}, \sigma^z \otimes \mathbb{1}_{2\times 2}, \sigma^y \otimes s^x, \sigma^y \otimes s^y, \sigma^y \otimes s^z\right). \tag{1.14}$$

The Γ matrices are called the Dirac matrices. Here σ and s Pauli matrices operate in the sublattice and spin space respectively. They obey $\Gamma^{a,b} = \left[\Gamma^a, \Gamma^b\right]/(2i)$, where the brackets denote commutation. The $d-$ parameters in Eq. 1.13 codify the information about the parameters of the original Hamiltonian. There are only eight non null terms, which are

$$\begin{aligned}
d_1 &= t(1 + 2\cos x \cos y), & d_{12} &= -2t \cos x \sin y, \\
d_2 &= \lambda_v, & d_{15} &= \lambda_{SO}(2\sin 2x - 4\sin x \cos y), \\
d_3 &= \lambda_R(1 - \cos x \cos y), & d_{23} &= -\lambda_R \cos x \sin y, \\
d_4 &= -\sqrt{3}\lambda_R \sin x \sin y, & d_{24} &= \sqrt{3}\lambda_R \sin x \cos y,
\end{aligned}$$

with $x = k_x a/2$ and $y = \sqrt{3}k_y a/2$. The time-reversal-operator is given by $\Theta\left|u(\vec{k})\right\rangle \equiv i(\mathbb{1}_{2\times 2} \otimes s^y)\left|u(\vec{k})\right\rangle^*$. Note that the five Dirac matrices are even under time-reversal, $\Theta\Gamma^a\Theta^{-1} = \Gamma^a$, but the commutators are odd, $\Theta\Gamma^{ab}\Theta^{-1} = -\Gamma^{ab}$. Also note that $\mathscr{H}$ is periodical in the lattice, i.e., $\mathscr{H}(\vec{k} + \vec{G}) = \mathscr{H}(\vec{k})$ for reciprocal lattice vectors $\vec{G}$. This makes $\mathscr{H}$ defined on a torus. Finally, the time-reversal-invariance is reflected in the symmetry (antisymmetry) of $d_a(d_{ab})$ under $\vec{k} \to -\vec{k}$.

For $\lambda_R = 0$, there is an energy gap with magnitude $|6\sqrt{3}\lambda_{SO} - 2\lambda_v|$. For $\lambda_v > 3\sqrt{3}\lambda_{SO}$, the gap is dominated by λ_v, and the system is an insulator. In the opposite regime, when $3\sqrt{3}\lambda_{SO} > \lambda_v$, the system describes the QSH phase. Although the Rashba term violates S_z conservation (that is the projection of the spin in $\check{z}$), for $\lambda_R < 2\sqrt{3}\lambda_{SO}$ there is a finite region of the phase diagram in Fig. 1.5 that is adiabatically connected to the QSH phase at $\lambda_R = 0$.

Figure 1.5 was taken from Ref.[31], in order to show the phase transition between the QSH and insulator regimes. It is obtained by solving the lattice model in a zigzag strip geometry [29]. Note that both phases have a energy gap in the bulk and there is a band crossing in each edge at $ka = \pi$ even in the insulator phase (Fig.1.5 (b)). But only in the QSH regime (Fig.1.5 (a)) the edge states traverse the energy gap in pairs. In the transition, the gap closes, allowing the edge states to switch a partner. It is important to observe that, in the QSH phase each energy in the bulk has a single time-reversed pair of eigenstates on each edge, and since time-reversal-symmetry prevents the mixing of Krammer's doublets, they are robust against (small) perturbations, that is, the gapless states persist even if the spatial symmetry is further reduced. Even more, weak disorder will not lead to localization of the edge states because single particle elastic backscattering is forbidden [29, 32].

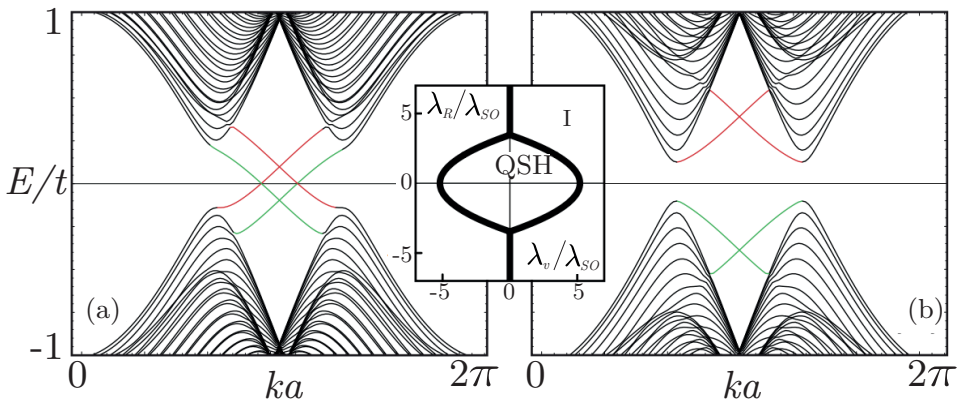

Figure 1.5: Band structure of the model presented by Kane and Mele with the Hamiltonian of Eq. (1.13). Different colors indicate different spin orientation . Panel (a) corresponds to the QSH phase where the lower bands are connected with the upper bands via the edge states ($\lambda_v = 0.1t$). Panel (b) corresponds to the insulating phase ($\lambda_v = 0.4t$). In both panels $\lambda_{SO} = 0.06t$ and $\lambda_R = 0.05t$. Note that in both situations, given an edge state there is a crossing at $ka = \pi$. Inset shows a phase diagram as function of λ_v and λ_R with $0 < \lambda_{SO} \ll t$.

To conclude this section, let's compare both IQHE and QSHE. IQHE requires the presence of a magnetic field which violates time-reversal-symmetry. However, if two copies of IQHE are put together, one for each spin orientation, then time-reversal-symmetry is restored. As it was shown, the time-reversal operator takes the complex conjugate of a wavefunction and it flips the spin. Therefore, a Hamiltonian in which the up and down spin are in opposite QH states is invariant under time-reversal. If an electric field is applied in this state, then the spin up electrons will go on one sense while the spin down electrons will go in the other one. Therefore, there is no net Hall current but there is a net flow of spin [35, 40]. When spin is conserved, this spin current defines a quantized spin Hall conductivity. A key ingredient to realize the QSH state was to consider the existence of a spin-orbit interaction, leading to a spin dependent second-neighbor hopping term. This is nothing more than two copies of the Haldane model [38].

The band calculation of this model, presented in Fig.1.5, shows that there is a bulk energy gap separating the conduction and the valence bands. But inside the gap there are bands localized at the edges. The spin up have a positive group velocity, while the downs spin have a negative group velocity. The spin up and down bands cross and the degeneracies should be lifted by arbitrarily weak perturbations. But it is not the case because these band-crossing are protected by time-reversal-symmetry. Time-reversal-symmetry manifests itself in half-integer-spin particles as the Kramers' theorem, which states that for every eigenstate of a time-reversal-invariant Hamiltonian is at least twofold degenerate. The two eigenstates that are crossing form a Kramers' pair and that degeneracy can not be lifted by any time-reversal-invariant perturbation even, if the conservation of spin is violated [41, 42].

Regarding to disorder, it is known that electronic systems are susceptible to Anderson localization. In one dimension, eigenstates are localized by arbitrarily weak disorder. So the expectation

would be that if the edges are dirty, i.e., with impurities, then it should become localized. The reason for this is that elastic backscattering due to disorder is a relevant perturbation. But in the QSH state, backscattering on the edge requires a spin flip because it would involve an up and down spin interchange, but it is odd operation against time-reversal-symmetry. In conclusion, the lowest order elastic backscattering process is forbidden. Even if the edges are totally dirty, the reflection amplitude of the backscattering process is odd, which means is zero, so the edges have a prefect transmission [32, 43, 44]. This means that the eigenstates of a helical edge cannot be localized, even for strong disorder. The helical edge is immune against Anderson localization. Similar situation happens in the IQHE with the chiral edge states.

In Ch. 4 we will introduce a mechanism to ensure backscattering in the edge states of a system under QSH. This mechanism is a nanomagnet that allows the backscattering by interchanging a spin momenta to the reflected electron leading to an optimal thermoelectrical machine. The ideas behind thermoelectricity will be developed in Ch. 2 together with the scattering matrix. But before that, let's introduce the last system to be considered, a superconductor. That is the topic of the last section of this chapter.

1.3 Superconductivity: general remarks

The most accepted theory for superconductivity is due to Bardeen, Cooper and Schriffer then called BCS theory [45]. It pursuits the explanation of electron-electron interaction mediated by phonons. Due to this interaction a novel ground state appears formed by a condensate of two electrons of opposite spin and momenta, which is commonly called a Cooper pair. Evidence of this ground state was observed, but neither explained nor understood in its moment, by measuring the thermal conductance and other transport properties of Hg performed by Kamerlingh-Onnes in 1911 [46]. It was observed that below the temperature of liquid He, 4.2K, the resistance of Hg dropped to zero. It was an astonishing discovery because, by that time it was expected a singular behaviour of the resistance at zero temperature, not at a finite value. In a normal metal the resistivity at low temperature has a constant contribution from impurity scattering, a T^2 contribution from electron-electron scattering and a higher power of temperature dependence (T^3 or even T^5) from phonon scattering. Thus, the vanishing value had to be a new ground state.

After Kamerlingh-Onnes' discovery, several other related phenomena appeared, like the expulsion of a magnetic field inside a material below a critical temperature, i.e., a perfect diamagnetic, in what now is called the Meissner effect in 1933 [47] or the superfluidity of bosonic liquid He-4 discovered by Kapitza and Misener in 1938 [48]. It was not until 1947 that an attempt to give a microscopic explanation was given first by Bogoliubov [49] and then in 1957 a more solid theory was formulated by Bardeen, Cooper and Schrieffer. In this section we will briefly review some points of this theory. A more detailed explanation of the theory of superconductivity can be found in Refs. [50–54].

1.3.1 Cooper instability

Let's consider an interacting two-electron system described by the following Schrödinger equation

$$\left[-\frac{\hbar^2}{2m}\nabla^2_{\vec{r}_1} - \frac{\hbar^2}{2m}\nabla^2_{\vec{r}_2} + V(\vec{r}_1 - \vec{r}_2)\right]\Psi(\vec{r}_1,\vec{r}_2) = E\Psi(\vec{r}_1,\vec{r}_2), \tag{1.15}$$

where $\vec{r}_1,\vec{r}_2$ refers to the position of each electron. As usual, it can be introduced a coordinate change to the displacement $\vec{r} = \vec{r}_1 - \vec{r}_2$ and the center of mass $\vec{R} = \frac{\vec{r}_1+\vec{r}_2}{2}$ leading to

$$\left[-\frac{\hbar^2}{2M}\nabla^2_{\vec{R}} - \frac{\hbar^2}{2\mu}\nabla^2_{\vec{r}} + V(\vec{r})\right]\Psi(\vec{r},\vec{R}) = E\Psi(\vec{r},\vec{R}), \tag{1.16}$$

being $M = 2m$ the total mass of the system and $\mu = m/2$ the reduced mass. Since there is a translational symmetry on $\vec{R}$,i.e., V only depends on $\vec{r}$ and not on $\vec{R}$, the solution can be decomposed as

$$\Psi(\vec{r},\vec{R}) = \phi(r)e^{i\vec{k}.\vec{R}},$$

leading to

$$\left[-\frac{\hbar^2}{2\mu}\nabla^2_{\vec{r}} + V(\vec{r})\right]\phi(\vec{r}) = \varepsilon\phi(\vec{r}), \tag{1.17}$$

with $\varepsilon = E - \frac{\hbar^2k^2}{2M}$. Note that the lowest eigenenergy takes place for $\vec{k} = 0$, that is, the center of mass is at rest. Let's consider this situation, $E = \varepsilon$. Depending on the spin-coupling, ϕ may be an even or odd function of $\vec{r}$, when the electrons form a singlet or triplet, respectively, in order to assure the anti-symmetry of the total wave function. A step further can be done by taking the Fourier transform on Eq. (1.17) with $\phi(\vec{q}) = \int d^3r e^{-i\vec{q}\vec{r}}\phi(\vec{r})$,

$$-\frac{\hbar^2}{2\mu}q^2\phi(\vec{q}) - \int d^3r V(\vec{r})\phi(r)e^{-i\vec{q}.\vec{r}} = E\phi(\vec{q}). \tag{1.18}$$

Note that the Fourier transformation on $\phi(\vec{r})$ can be thought as made of two plane waves with opposite momentum, $\vec{q}$ and $-\vec{q}$. Multiplying Eq. (1.18) by an orthogonal element $\int \frac{d^3p}{(2\pi)^3}e^{i\vec{p}.\vec{r}}$ get a relation for the potential V

$$\begin{aligned}\int \frac{d^3p}{(2\pi)^3}V(\vec{p})\int d^3r\phi(\vec{r})e^{-i(\vec{q}-\vec{p})\vec{r}} &= \left(E - \frac{\hbar^2q^2}{m}\right)\phi(\vec{q}),\\ \int \frac{d^3p'}{(2\pi)^3}V(\vec{q}-\vec{p'})\phi(\vec{p'}) &= \left(E - 2\varepsilon_{\vec{q}}\right)\phi(\vec{q}),\end{aligned} \tag{1.19}$$

where in the last line the change of variables $\vec{p'} = \vec{q} - \vec{p}$ was introduced and, as well as, the definition of the free-electron energy, $\varepsilon_{\vec{q}} = \frac{\hbar^2q^2}{2m}$. Note that for a bound state the electrons have energy $E < \varepsilon_{\vec{q}}$, that is, the total energy is smaller than the sum of two independent electrons. Finally let's define a modified wave function

$$\Delta(\vec{q}) = \left(E - 2\varepsilon_{\vec{q}}\right)\phi(\vec{q}), \tag{1.20}$$

so that Eq.(1.19) becomes

$$\Delta(\vec{q}) = -\int \frac{d^3p}{(2\pi)^3} \frac{V(\vec{q}-\vec{p})}{2\varepsilon_{\vec{q}} - E} \Delta(p). \tag{1.21}$$

To go forward let's assume the electrons are in a singlet state so that the solutions of Eq. (1.21) are $\Delta(\vec{q}) \simeq \Delta_0$ (at least at first order). Also,we assume that all the levels below the Fermi sea are already occupied. Finally, we assume that the phonon-mediated electron-electron interaction, V, is an attractive potential, $V(\vec{q}-\vec{p}) = -V_0$ and that there exists a cut-off energy above which V goes to zero,

$$V(\vec{q}-\vec{p}) = \begin{cases} -V_0 \text{ if } \varepsilon_{\vec{q},\vec{p}} \leq k_B\Theta_D, \\ 0 \text{ otherwise,} \end{cases} \tag{1.22}$$

with k_B the Boltzmann constant and Θ_D the Debye temperature. With all this assumptions, Eq. (1.21) becomes

$$\Delta_0 = V_0\rho(\varepsilon_F)\Delta_0 \int_{E_F}^{E_F+k_B\Theta_D} \frac{d\varepsilon}{2\varepsilon - E}$$

$$\frac{2}{V_0\rho(\varepsilon_F)} = \ln\left(\frac{2E_F - E + 2k_B\Theta_D}{2E_F - E}\right). \tag{1.23}$$

As all the states below the Fermi level are occupied, the ones that will be affected by the interaction are those having energies $E_F < \varepsilon < E_F + k_B\Theta_D$.

In the limit of small $V_0\rho(E_F) < 1$, E is close to $2E_F$, and it can be approximated as $2E_F - E + 2k_B\Theta_D \simeq 2\Theta_D$. Then, the solution is

$$E = 2E_F - 2k_B\Theta_D e^{-\frac{2}{V_0\rho(\varepsilon_F)}}. \tag{1.24}$$

Note that this energy is negative, hence it corresponds to a bound state. A bound state suggests a gap in the spectrum, which is consistent with the exponentially falling heat capacity observed experimentally. This state is called a Cooper pair, which is formed by two electrons with different momenta and different spin orientations (in the situation of a singlet). In the following section we will study the many-body problem leading to the BCS state as the ground state of the superconducting phase.

1.3.2 BCS theory of superconductivity

The question that naturally arises in relation to the previous section is what would happen when the Cooper pair proliferate. Consider the following Hamiltonian

$$H = \sum_{k,\sigma} \xi_k c^\dagger_{k,\sigma} c_{k,\sigma} + \sum_{k,k'} V_{k,k'} c^\dagger_{k,\uparrow} c^\dagger_{-k,\downarrow} c_{-k',\downarrow} c_{k',\uparrow}, \tag{1.25}$$

where $c^\dagger_{k,\sigma}(c_{k,\sigma})$ creates (destroys) an electron with momentum k and spin σ, and the energy is defined from the chemical potential level, i.e., $\xi_k = \varepsilon_k - \mu$. Note that the creation and destruction of Cooper pairs is written explicitly in the second term of the Hamiltonian 1.25.

To decouple the interaction term, we use the mean field approximation

(1.26)
$$\left\langle c^{\dagger}_{k,\uparrow}c^{\dagger}_{-k,\downarrow}c_{-k',\downarrow}c_{k',\uparrow}\right\rangle \simeq \left\langle c^{\dagger}_{k,\uparrow}c^{\dagger}_{-k,\downarrow}\right\rangle c_{-k',\downarrow}c_{k',\uparrow} + c^{\dagger}_{k,\uparrow}c^{\dagger}_{-k,\downarrow}\left\langle c_{-k',\downarrow}c_{k',\uparrow}\right\rangle - \left\langle c^{\dagger}_{k,\uparrow}c^{\dagger}_{-k,\downarrow}\right\rangle\left\langle c_{-k',\downarrow}c_{k',\uparrow}\right\rangle.$$

The mean value $\left\langle c^{\dagger}_{k,\uparrow}c^{\dagger}_{-k,\downarrow}\right\rangle$ is non zero since it corresponds to one Cooper pair in superconducting state. Also, it is useful to define the function

(1.27)
$$\Delta_k = \sum_{k'} V_{k,k'}\left\langle c_{-k',\downarrow}c_{k',\uparrow}\right\rangle,$$

so that the Hamiltonian of Eq. (1.25) becomes

(1.28)
$$H = \sum_{k\sigma}\xi_k c^{\dagger}_{k,\sigma}c_{k,\sigma} + \sum_k\left(\Delta_k c^{\dagger}_{k,\uparrow}c^{\dagger}_{-k,\downarrow} + \Delta^*_k c_{-k,\downarrow}c_{k,\uparrow}\right) + \sum_k \Delta_k\left\langle c^{\dagger}_{k,\uparrow}c^{\dagger}_{-k,\downarrow}\right\rangle.$$

This Hamiltonian is diagonalized by the Bogoliubov transformation

(1.29a)
$$c_{k,\uparrow} = u^*_k\gamma_{k,\uparrow} + v_k\gamma^{\dagger}_{-k,\downarrow}$$

(1.29b)
$$c^{\dagger}_{-k,\downarrow} = u_k\gamma^{\dagger}_{-k,\downarrow} - v_k\gamma_{k,\uparrow}.$$

In order to satisfy the commutation rules, the new operators $\gamma_{k,\sigma}$ have to satisfy the following relations

$$\left\{\gamma_{k,\sigma},\gamma^{\dagger}_{k',\sigma'}\right\} = \delta_{k,k'}\delta_{\sigma,\sigma'};\ \ \left\{\gamma_{k,\sigma},\gamma_{k',\sigma'}\right\} = \left\{\gamma^{\dagger}_{k,\sigma},\gamma^{\dagger}_{k',\sigma'}\right\} = 0,$$

implying

$$|u_k|^2 + |v_k|^2 = 1.$$

The coefficients of Eqs. (1.29) diagonalizing H are

(1.30a)
$$|u_k|^2 = \frac{1}{2}\left(1 + \frac{\xi_k}{\sqrt{\xi_k^2 + |\Delta_k|^2}}\right)$$

(1.30b)
$$|v_k|^2 = \frac{1}{2}\left(1 - \frac{\xi_k}{\sqrt{\xi_k^2 + |\Delta_k|^2}}\right)$$

The diagonalized BCS Hamiltonian reads:

(1.31a)
$$H = \sum_k E_k\left(\gamma^{\dagger}_{k,\uparrow}\gamma_{k,\uparrow} + \gamma^{\dagger}_{-k,\downarrow}\gamma_{-k,\downarrow}\right) +$$

(1.31b)
$$+ \sum_k\left[\xi_k - E_k - \Delta_k\left\langle c^{\dagger}_{k,\uparrow}c^{\dagger}_{-k,\downarrow}\right\rangle\right],$$

with

$$E_k = \sqrt{\xi_k^2 + \Delta_k^2}.$$

It is usual that $|\Delta_{-k}| = |\Delta_k|$ so that Eq. (1.31a) becomes $\sum_{k,\sigma}E_k\gamma^{\dagger}_{k,\sigma}\gamma_{k,\sigma}$. On the other hand the second term, Eq. (1.31b) is the ground state energy of the condensate. The term Δ_k is called

the energy gap. In fact, for the energy equal to the Fermi level, $\xi_k = 0$, the energy spectrum of the superconductor has a gap of amplitude $|\Delta_k|$. Therefore, a minimum energy equal to $2|\Delta_k|$ is needed to break a Cooper pair and to excite its quasi-particles, which are described by the operator $\gamma^\dagger_{k,\sigma}$. These operators are usually called Bogoliubons. Note that from Eqs. (1.29), the Bogoliubons are described by a mixture of particles and holes

$$\gamma_{k,\uparrow} = u_k c_{k,\uparrow} - v_k c^\dagger_{-k,\downarrow} \tag{1.32a}$$

$$\gamma^\dagger_{-k,\downarrow} = u^*_k c^\dagger_{-k,\downarrow} + v^*_k c_{k,\uparrow}. \tag{1.32b}$$

Finally, to end this section we observe from Eqs.(1.30) we have that when $\Delta_k \to 0$ $u_k \to 1$ when $\xi_k > 0$ and $u_k \to 0$ when $\xi_k < 0$ with the opposite behavior for v_k, Hence, in the normal state, creating a Bogoliubov's excitation corresponds to creating an electron above the Fermi sea and destroying it (or creating a hole) of opposite momentum and spin below the Fermi sea. Instead, in a superconducting regime the Bogoliubon becomes a superposition of both electron and hole state.

1.3.3 The gap equation

We now discuss the dependence of the gap with the temperature. This will play a key role mainly in Ch. 5. Also, knowing Δ_k determines completely the problem. In order to do so, let's come back to the definition of Δ_k in Eq. (1.27) and replace the Bogoliubov transformation defined in Eqs. (1.29) in order to have an implicit equation for Δ_k that is solved self-consistently,

$$\Delta_k = \sum_{k'} V_{k,k'} \left[u^2_{k'} \langle \gamma_{-k',\downarrow} \gamma_{k',\uparrow} \rangle + v^*_{k'} u_{k'} \left\langle \gamma^\dagger_{k',\uparrow} \gamma_{k',\uparrow} \right\rangle - v^*_{k'} u_{k'} \left\langle \gamma_{-k',\downarrow} \gamma^\dagger_{-k',\downarrow} \right\rangle + (v^*_{k'})^2 \left\langle \gamma^\dagger_{k',\uparrow} \gamma^\dagger_{-k',\downarrow} \right\rangle \right]. \tag{1.33}$$

For fermionic Bogoliubov quasiparticles in thermal equilibrium holds the following properties

$$\langle \gamma_{-k',\downarrow} \gamma_{k'\uparrow} \rangle = \left\langle \gamma^\dagger_{k',\uparrow} \gamma^\dagger_{-k'\downarrow} \right\rangle = 0, \tag{1.34a}$$

$$\left\langle \gamma^\dagger_{k',\uparrow} \gamma_{k'\uparrow} \right\rangle = 1 - \left\langle \gamma_{-k',\downarrow} \gamma^\dagger_{-k'\downarrow} \right\rangle = f(E_{k'}), \tag{1.34b}$$

with $f(E_k)$ the Fermi-Dirac distribution,

$$f(E) = \frac{1}{1 + \exp\left(\frac{E}{k_B T}\right)},$$

with T being the temperature. Thus, the equation for the gap becomes,

$$\Delta_k = -\sum_k V_{k,k'} u_{k'} v^*_{k'} [1 - 2f(E_{k'})] = -\sum_{k'} V_{k,k'} \frac{\Delta_{k'}}{2E_{k'}} \tanh\left(\frac{E_k}{k_B T}\right), \tag{1.35}$$

where it is not considered the trivial solution $\Delta_k = 0$. As said before, $V_{k,k'}$ is considered constant as long as $|\xi_k|, |\xi_{k'}| < k_B \Theta_D$ and zero otherwise. As the potential does not depend on k, k' it is worth to look for solutions to Δ_k also independent on k and real. Due to this symmetry, this kind

of gap is called an s-wave gap since its angular dependence is that of the Y_{00} spherical harmonic [50, 54]. Introducing the density of states in Eq. (1.35), and using the fact that for $k_B\Theta_D \ll \mu$, the density of states can be approximated to its value on the Fermi surface as follows,

$$1 = V_0\rho(E_f)\int_0^{k_B\Theta_D} \frac{1}{\sqrt{\varepsilon^2+\Delta^2}} \tanh\left(\frac{\sqrt{\varepsilon^2+\Delta^2}}{k_BT}\right). \tag{1.36}$$

At $T = 0$, the hyperbolic tangent goes to 1 and Eq. (1.36) becomes

$$1 = V_0\rho(E_F)\int_0^{k_B\Theta_D} \frac{1}{\sqrt{\varepsilon^2+\Delta_0^2}}, \tag{1.37}$$

where $\Delta_0 = \Delta(T = 0)$. Integration is straightforward and gives

$$\frac{1}{V_0\rho(E_F)} = \operatorname{arcsinh}\left(\frac{k_B\Theta_D}{\Delta_0}\right). \tag{1.38}$$

Generally, one is in the situation where $\Delta_0 \ll k_B\Theta_D$ so that arcsinh can be expanded in series for large argument, leading to

$$\frac{1}{V_0\rho(E_F)} = \ln\left(\frac{2k_B\Theta_D}{\Delta_0}\right),$$

or equivalently

$$\Delta_0 = 2k_B\Theta_D e^{-\frac{1}{V_0\rho(E_F)}}. \tag{1.39}$$

Notice that this is the same result obtained in Sec. 1.3.1, that is, an arbitrarily small attractive potential rises a finite gap at zero temperature.

Also the critical temperature, T_C can be found by noticing that $\Delta(T > T_c) = 0$, so that the integration on Eq. (1.36) becomes, after performing a change of variables,

$$\frac{1}{V_0\rho(E_F)} = \int_0^{\frac{\Theta_D}{2T_C}} \frac{\tanh x}{x} dx.$$

Integrating parts and using the fact that $\Theta_D \gg T_C$, we get

$$T_C = \Theta_D \frac{2e^{\gamma_E}}{\pi} e^{-\frac{1}{V_0\rho(E_F)}}, \tag{1.40}$$

with $\gamma_E = 0.577...$ being the Euler constant. Note that, again, there is a dependence on $e^{-\frac{1}{V_0\rho(E_F)}}$. By identifying Δ_0 it can be derived a universal relation between the superconducting gap and the critical temperature

$$\frac{\Delta_0}{k_BT_C} = \frac{\pi}{e^{\gamma_E}} \simeq 1.7638... \tag{1.41}$$

For low temperatures such that $T \ll T_C$ the integral of Eq. 1.36 gives [50, 54]

$$\Delta \simeq \Delta_0 + (2\pi k_BT)^{1/2} e^{-\Delta_0/k_BT}. \tag{1.42}$$

For temperatures such that $T_C - T \ll T_C$ it can be deduced another relation

$$\Delta(T) \simeq 1.74\Delta_0\sqrt{1-\frac{T}{T_C}}. \tag{1.43}$$

There is also an interpolating formula that reproduces within 98% of accuracy the self consistent formula of Eq. (1.36) for temperatures close to zero and close to T_C,

$$\Delta(T) = \Delta_0 \tanh\left(1.74\sqrt{\frac{T_C}{T}-1}\right). \tag{1.44}$$

1.3.4 Bogoliubov-de-Gennes formalism for s-wave superconductors

There exists another formalism that emphasizes the symmetries discussed in Eqs. 1.32 (a) and 1.32 (b) in a more compact way. That is the Bogoliubov-de-Gennes. Let's start by the free particle Hamiltonian

$$H = \sum_{k,\sigma} c^\dagger_{k,\sigma}\varepsilon(k)c_{k,\sigma} = \frac{1}{2}\sum_{k,\sigma}\left[c^\dagger_{k,\sigma}\varepsilon(k)c_{k,\sigma} - c_{-k,\sigma}\varepsilon(-k)c^\dagger_{-k,\sigma}\right] + \frac{1}{2}\sum_k \varepsilon(k), \tag{1.45}$$

where as usual, $c^\dagger_{k,\sigma}(c_{k,\sigma})$ creates (destroys) en electron with momentum k and spin σ and ε being the energy of that electron. The spinor $\Psi = \left(c_{k,\uparrow}, c_{k,\downarrow}, c^\dagger_{-k,\uparrow}, c^\dagger_{-k,\downarrow}\right)^T$ is introduced and the Hamiltonian is rewritten as

$$H = \sum_k \Psi^\dagger_k H_{\mathrm{BdG}}\Psi + E, \tag{1.46}$$

where

$$H_{\mathrm{BdG}}(k) = \frac{1}{2}\begin{pmatrix}\varepsilon(k)\mathbb{1}_{2\times 2} & 0\\ 0 & -\varepsilon(-k)\mathbb{1}_{2\times 2}.\end{pmatrix}$$

and $E = \frac{1}{2}\sum_k \varepsilon(k)$ is a constant term which can be dropped. The Hamiltonian $H_{\mathrm{BdG}}(k)$ is invariant under the transformation $C = \tau^x \otimes \mathbb{1}_{2\times 2}$ that is, $H_{\mathrm{BdG}}(k) = -CH^T_{\mathrm{BdG}}(-k)C^{-1}$, being τ^x the Pauli matrix acting on the particle-hole space. The complete Hamiltonian obeys $H = -CH^TC^{-1} = -CH^*C^{-1}$. This invariance is known as particle-hole symmetry. Note that this description adds degrees of freedom, instead of having two (one for band and two for spin) we end up having four. To see the effectiveness of this formalism let's introduce now a pairing potential that, simply couples the upper and lower blocks of H_{BdG} and we will focus only on a s-wave superconductor. Under these assumptions the pairing term can be written as

$$H_\Delta = \Delta c^\dagger_{k\uparrow}c^\dagger_{-k\downarrow} + \Delta^* c_{-k\downarrow}c_{k\uparrow} = \frac{1}{2}\left[\Delta\left(c^\dagger_{-k\downarrow}c^\dagger_{k\uparrow}\right) + \Delta^*\left(c_{k\downarrow}c_{k\uparrow} - c_{k\uparrow}c_{-k\downarrow}\right)\right], \tag{1.47}$$

with $\Delta \in \mathbb{C}$ being the superconducting order parameter. We can observe that rewritten in this way, this term evidences that two electrons or holes combine to a Cooper pair or a Cooper pair breaks

into its constituents. In this way the sum of both $H_{\mathrm{BdG}} + H_{\Delta}$ reads as

$$H_{\mathrm{BdG}} + H_{\Delta} = \frac{1}{2}\begin{pmatrix} \varepsilon(k) & 0 & 0 & \Delta \\ 0 & \varepsilon(k) & -\Delta & 0 \\ 0 & -\Delta^* & -\varepsilon(-k) & 0 \\ \Delta^* & 0 & 0 & -\varepsilon(-k) \end{pmatrix}. \tag{1.48}$$

At the same time, Eq. 1.48 can be decomposed in blocks as

$$H_{\mathrm{BdG}} + H_{\Delta} = \varepsilon(k)\tau^z \otimes \mathbb{1}_{2\times 2} - \left(\mathrm{Re}(\Delta)\tau^y + \mathrm{Im}(\Delta)\tau^x\right) \otimes \sigma^y, \tag{1.49}$$

where τ^i is the Pauli matrix operates in the particle-hole degrees of freedom while σ^i do it in the spin space. Note that the matrices are mutually anticommuting so that the spectrum can be easily computed by $(H_{\mathrm{BdG}} + H_{\Delta})^2 = (\varepsilon(k) + |\Delta|)^2 \mathbb{1}_{4\times 4}$. Thus, the energy spectrum is made up of two doubly degenerate bands with energies

$$E_{\pm} = \pm\sqrt{\varepsilon(k)^2 + |\Delta|^2}$$

and it presents a gap whenever $\Delta \neq 0$. Let's recall that the transformation that diagonalizes the Hamiltonian, the Bogoliubon of Eqs. (1.29),thus, the quasi-particles that are excited in a superconductor are a mixture of quasi-particles and quasi-holes.

1.4 Organization of this thesis

The basic properties of the systems under consideration were already presented in this chapter. In chapter 2 we will introduce the general framework to analyze the thermoelectric properties of those systems. In Sec. 2.1 we will present some general remarks on the scattering matrix formalism with an example for a Normal-Superconductor (NS) junction (Sec. 2.1.1), while Sec. 2.2 is devoted to introduced the other framework, Onsager theory of linear response for two reservoirs with a temperature and chemical potential bias. Concepts such as the transmission function, efficiency, figure of merit are also introduced there.

The theoretical treatment of chapter 2 will be applied to study the different systems. In chapter 3 we will present measurements of a quantum Hall system under the Corbino geometry. This geometry is ideal to study the thermal current independently of the electrical current. We will model the transport in linear response regime.

In chapter 4 the transmission function of a two-dimensional topological insulator is calculated alongside its transport response. We will show that when the edge states are coupled to a magnetic impurity, optimal efficiency and great figure of merit can be achieved

In chapter 5 the system previously analyzed in chapter 4 is studied with superconducting terminals. The main framework used here is the scattering matrix formalism. We will analyze the thermal conductance and show its dependence on the properties of the system such as the existence of a topological regime. Finally, in chapter 6 an overview of this thesis is presented.

CHAPTER 2

SOME THEORETICAL CONSIDERATIONS

This chapter is devoted to give the theoretical framework that will be used alongside this thesis, without presenting a complete overview of the subject. To begin with, in Sec. 2.1 the main ideas behind the formalism of scattering matrix are introduced. In particular, its evaluation for a single and composed scatterer, the symmetries and some other useful properties. An example is presented in Sec. 2.1.1 for the case of a Normal-Superconductor (NS) junction. In Sec. 2.2 the contact between the scattering matrix formalism, the transport elements and the Landauer-Büttiker formula are discussed. The key element is the transmission function, which is introduced in the context of linear response theory in Sec. 2.2.1. Some properties characterizing the thermoelectric performance, such as the efficiency and figure of merit are presented in Sec. 2.2.2.

2.1 Scattering Matrix formalism; general remarks

The purpose of this section is to develop the main ideas of the scattering matrix formalism that will be used along this thesis and will let us to calculate the transport coefficients. For sake of clarity, we will consider spinless electrons. To start with, suppose the following 1-D Hamiltonian

$$H = H_0 + V,$$

with H_0 being a Hamiltonian easy to solve and V is a potential that allows to distinguish at least two regions, for example

$$V = \begin{cases} V(x) \text{ for } 0 < x < l, \\ 0 \text{ otherwise}, \end{cases} \tag{2.1}$$

being l the length of the system of interest. Eventually l can be set to zero, for instance in an insulator interface or infinity such as the situation of the idealized junction between two

materials. This separation allows us to distinguish a solution for each domain

$$\Psi_L = \Psi_L^+(x) + \Psi_L^-(x)\ ;\ x \leq 0, \tag{2.2a}$$

$$\Phi(x)\ ;\ 0 < x \leq l, \tag{2.2b}$$

$$\Psi_R = \Psi_R^+(x) + \Psi_R^-(x)\ ;\ x > l, \tag{2.2c}$$

where $\Psi_{L,R}$ is the solution of H_0 localized at left or right of the interface, $\pm$ indicates its propagation (for instance Ψ_L^- means that is located at the left of the interface and moving to right) and Φ is the solution inside the scatterer. This situation is depicted in Fig. 2.1. The central system, depicted with a green circle, is the scattering region and is characterized by the $V(x)$ potential profile. Incident waves, Ψ_L^+ and Ψ_R^- may be reflected or transmitted. This information is codified in the outgoing states Ψ_L^- and Ψ_R^+.

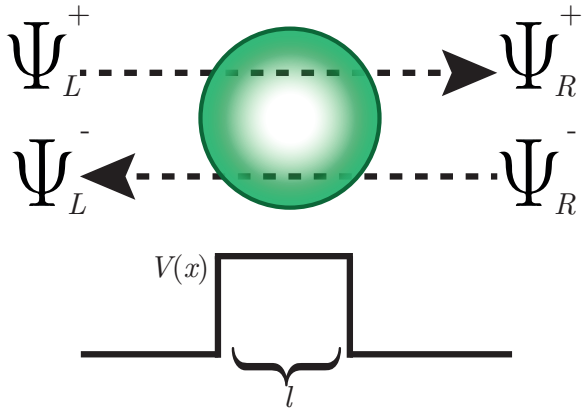

Figure 2.1: Incident waves (Ψ_L^+ and Ψ_R^-) are scattered by the system (green circle) characterized by the potential V (profile depicted in solid lines at bottom of the figure). Reflected and transmitted wave functions through the system are described by Ψ_L^- and Ψ_R^+ .

The general solution of the Schrödinger equation $H\Psi = E\Psi$ must be a continuous function of the position and of its first derivative [1],

$$\Psi_L(x = 0^-) = \Phi(x = 0^+)\ ;\ \left.\frac{\partial \Psi_L}{\partial x}\right|_{x=0^-} = \left.\frac{\partial \Phi}{\partial x}\right|_{x=0^+}, \tag{2.3a}$$

$$\Psi_R(x = l^+) = \Phi(x = l^-)\ ;\ \left.\frac{\partial \Psi_R}{\partial x}\right|_{x=l^+} = \left.\frac{\partial \Phi}{\partial x}\right|_{x=l^-}. \tag{2.3b}$$

Recall that due to the fact that $V(x)$ can be a very complicated function, the solution of the Hamiltonian inside the scattering region may not be analytical. Outside there, the solution can be expressed as a linear combination of solutions of the free part of the Hamiltonian, generally $H_0 \propto \frac{\partial^2}{\partial x^2}$ or $H_0 \propto \frac{\partial}{\partial x}$, where the eigenfunctions are plane waves. In most of the cases it is enough

[1] This is not true when the potential $V(x)$ is a Dirac-δ function, where a discontinuity must be set, i.e. $\left.\frac{\partial \Psi_L}{\partial x}\right|_{x=0^-} - \left.\frac{\partial \Phi}{\partial x}\right|_{x=0^+} = \Lambda$, with Λ the potential at the interface. See for instance Ref. [55] and references therein.

to know the solutions outside. In general, a linear relation between the incoming and outgoing waves can be written as

$$\begin{pmatrix} \Psi_L^-(x=0) \\ \\ \Psi_R^+(x=l) \end{pmatrix} = \mathbf{S} \begin{pmatrix} \Psi_L^+(x=0) \\ \\ \Psi_R^-(x=l) \end{pmatrix}, \tag{2.4}$$

where $\mathbf{S}$ is the so called scattering matrix. Note that the off-diagonal elements represent the amplitude of an incoming wave from left be transmitted to the right, S_{21}, and incoming from right be transmitted at left, S_{12}. The diagonal elements represent the amplitude of being reflected back, S_{11} for a left incoming wave, and S_{22} for a right incoming wave. Because of this, the scattering matrix is also usually written as

$$\mathbf{S} = \begin{pmatrix} r & t' \\ t & r' \end{pmatrix}. \tag{2.5}$$

where the element modulus square is called the probability amplitude of being reflected if it is r or r' and the amplitude of being transmitted if it is t or t'.

Another possible way to relate the waves is via the transfer matrix $\mathbf{T}$,

$$\begin{pmatrix} \Psi_R^+(x=l) \\ \\ \Psi_R^-(x=l) \end{pmatrix} = \mathbf{T} \begin{pmatrix} \Psi_L^+(x=0) \\ \\ \Psi_L^-(x=0) \end{pmatrix}, \tag{2.6}$$

The difference between both matrices is that while the scattering matrix relates the outgoing waves with the incoming ones, the transfer matrix relates the left hand side with the right hand side of the scatterer region. Note that the two formalisms are equivalent; in fact both matrices are related via

$$\mathbf{S} = \frac{1}{T_{22}} \begin{pmatrix} -T_{21} & 1 \\ \det\mathbf{T} & T_{12} \end{pmatrix}; \tag{2.7a}$$

$$\mathbf{T} = \frac{1}{S_{12}} \begin{pmatrix} -\det\mathbf{S} & S_{22} \\ -S_{11} & 1 \end{pmatrix} = \begin{pmatrix} t' - \frac{rr'}{t} & \frac{r}{t} \\ -\frac{r'}{t} & \frac{1}{t} \end{pmatrix}. \tag{2.7b}$$

This means, for instance, that the amplitude t from Eq.(2.5) in the language of transfer matrix is the inverse of T_{22} and similar arguments apply to the other amplitudes.

The elements of $\mathbf{S}$ are not all independent. There are some properties that must be satisfied. If we are in time-independent problem, then there is conservation of the current, that is the incoming particle flux equals the outgoing particle flux, then $\mathbf{S}$ has to be unitary. This property leads to some interesting relations, for example

$$\left(\mathbf{S}\cdot\mathbf{S}^\dagger\right)_{11} = |r|^2 + \left|t'\right|^2 = 1. \tag{2.8}$$

Note that both probabilities sum up to one, so that a particle is transmitted with probability $|t'|^2$ and reflected with probability $|r|^2 = 1 - |t'|^2$. Different relations can be found if it is looked at the other elements of the product $\mathbf{S} \cdot \mathbf{S}^\dagger$ [56, 57].

Another property is due to time-reversal-symmetry. As we are considering spinless particles, if $\Psi(x)$ is a solution of the Scrödinger equation, then $\Psi^*(x)$ is also a solution. This implies that the scattering matrix is symmetric. This can be easily probed; the incoming waves now are Ψ_L^{-*} and Ψ_R^{+*} while the outgoing waves are Ψ_L^{+*} and Ψ_R^{-*}. The scattering matrix relates any incoming and outgoing waves, so that we have

$$\begin{pmatrix} \Psi_L^{+*} \\ \\ \Psi_R^{-*} \end{pmatrix} = \mathbf{S} \begin{pmatrix} \Psi_L^{-*} \\ \\ \Psi_R^{+*} \end{pmatrix}. \tag{2.9}$$

On the other hand, if it is conjugated Eq. (2.4) and it is replaced in Eq.(2.9), it is found

$$\begin{pmatrix} \Psi_L^{+*} \\ \\ \Psi_R^{-*} \end{pmatrix} = \mathbf{S} \cdot \mathbf{S}^* \begin{pmatrix} \Psi_L^{+*} \\ \\ \Psi_R^{-*} \end{pmatrix}. \tag{2.10}$$

As this relation must be true for any incoming wave, it can be concluded that

$$\mathbf{S} \cdot \mathbf{S}^* = \mathbf{S}^* \cdot \mathbf{S} = \mathbb{1} \tag{2.11}$$

where $\mathbb{1}$ is the identity matrix. Combining this result with the unitarity we get $\mathbf{S}^* = \mathbf{S}^\dagger$. More general relations and symmetries of the scattering matrix are explained and discussed in Refs. [58–60].

To end this section, we will present next how the effective scattering matrix is calculated when there are two scattering regions under the hypothesis of coherent transport. For a more detailed explanation the reader is deferred to Refs. [61, 62].

Figure 2.2 presents two scattering regions, 1 and 2, depicted with green and purple circles respectively. There is an incoming wave at left of 1. Part of this incoming wave is transmitted and other part is reflected. The part that is transmitted by the first scatterer may be either reflected or transmitted by the second scatterer. If it is reflected, then it is an incoming wave for 1 and, again, it can be either transmitted or reflected and so on. The same reasoning applies to an incoming wave at the right of 2.

Let $\mathbf{S}^{(1)}$ and $\mathbf{S}^{(2)}$ be the scattering matrices of the scatterers 1 and 2, respectively, and let us denote their elements with the respective super-index. The combination of the two scattering matrices is denoted by the operator $\otimes$ and its combination by $\mathbf{S}$,

$$\mathbf{S} = \mathbf{S}^{(1)} \otimes \mathbf{S}^{(2)} = \begin{pmatrix} r & t' \\ t & r' \end{pmatrix}.$$

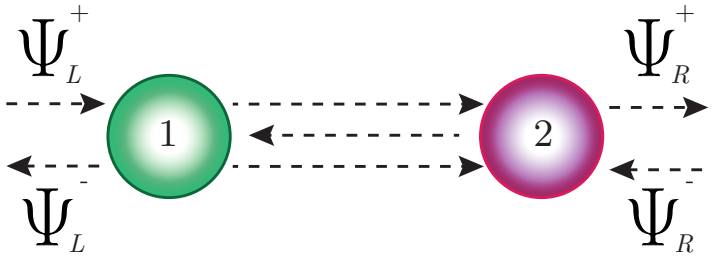

Figure 2.2: Two scattering regions 1 and 2 depicted with green and purple. Infinite reflections occur in the region between them. In the figure, only three are depicted.

If there is an incident wave at left of 1 only, the transmission and the reflection after passing through the first scatterer is calculated by

$$\mathbf{S}^{(1)}\Psi = \begin{pmatrix} r^{(1)} & t'^{(1)} \\ t^{(1)} & r'^{(1)} \end{pmatrix} \begin{pmatrix} \Psi_L^+ \\ 0 \end{pmatrix} = \begin{pmatrix} r^{(1)}\Psi_L^+ \\ t^{(1)}\Psi_L^+ \end{pmatrix}. \tag{2.12}$$

Note that for the second scatterer, $t^{(1)}\Psi_L^+$ is the incoming wave at left while $r^{(1)}\Psi_L^+$ is out of the system. For simplicity, it will be considered next $\Psi_R^- = 0$, then the scattering with system 2 is

$$\mathbf{S}^{(2)} \begin{pmatrix} t^{(1)}\Psi_L^+ \\ 0 \end{pmatrix} = \begin{pmatrix} r^{(2)} & t'^{(2)} \\ t^{(2)} & r'^{(2)} \end{pmatrix} \begin{pmatrix} t^{(1)}\Psi_L^+ \\ 0 \end{pmatrix} = \begin{pmatrix} r^{(2)}t^{(1)}\Psi_L^+ \\ t'^{(2)}t^{(1)}\Psi_L^+ \end{pmatrix}. \tag{2.13}$$

This last equation is telling us that, in order to have an outgoing wave at right, first it must have been transmitted twice, once per each scatterer. The two reflections (one per each scatterer) lead to the following results

$$\mathbf{S}^{(1)} \begin{pmatrix} 0 \\ r^{(2)}t^{(1)}\Psi_L^+ \end{pmatrix} = \begin{pmatrix} t'^{(1)}r^{(2)}t^{(1)}\Psi_L^+ \\ r'^{(1)}r^{(2)}t^{(1)}\Psi_L^+ \end{pmatrix} \tag{2.14a}$$

$$\mathbf{S}^{(2)} \begin{pmatrix} r'^{(1)}r^{(2)}t^{(1)}\Psi_L^+ \\ 0 \end{pmatrix} = \begin{pmatrix} t^{(2)}r'^{(1)}r^{(2)}t^{(1)}\Psi_L^+ \\ r'^{(2)}r'^{(1)}r^{(2)}t^{(1)}\Psi_L^+ \end{pmatrix} \tag{2.14b}$$

Note that after two reflections the effective transmission is

$$t = t^{(2)}t^{(1)} + t^{(2)}(r'^{(1)}r^{(2)})t^{(1)}. \tag{2.15}$$

This means that, when there is an incoming wave at the left of the system, the effective transmission is obtained after being transmitted by both systems plus being transmitted by the first, then being reflected by the second, by the first again and finally being transmitted by the second. If there were more reflections, note each reflection would add a term proportional to a power of $r'^{(1)}r^{(2)}$. Hence, it can be inferred that the complete series must be

$$t = \sum_{n=0}^{\infty} t^{(2)}(r'^{(1)}r^{(2)})^n t^{(1)}, \tag{2.16}$$

where each term counts how many times the wave was reflected by the second and first scatterer. Luckily, this series converges because $|r'^{(1)}r^{(2)}| < 1$, so the effective transmission for two scattering regions is

$$t = t^{(2)}(1 - r'^{(1)}r^{(2)})^{-1}t^{(1)}. \tag{2.17}$$

Something similar happens for the reflection coefficient. The first terms of the series for the left outgoing wave are

$$r = r^{(1)} + t'^{(1)}r^{(2)}t^{(1)} + t'^{(1)}r^{(2)}r^{(1)}r^{(2)}t^{(1)}, \tag{2.18}$$

where the last term was obtained after considering two more reflections. Again, this series converges to

$$r = r^{(1)} + t'^{(1)}r^{(2)}(1 - r^{(1)}r^{(2)})^{-1}t^{(1)}. \tag{2.19}$$

The other two elements of the full scattering matrix, r' and t', are calculated from an incoming wave at right. It can also be noticed that the result is achieved by the substitution $1 \leftrightarrow 2$, tilde for no tilde and viceversa. For instance the first terms of both r' and t' are

$$r' = r'^{(2)} + t^{(2)}r'^{(1)}t'^{(2)} + t^{(2)}r'^{(1)}r'^{(2)}r'^{(1)}t'^{(2)}, \tag{2.20a}$$

$$t' = t'^{(1)}t'^{(2)} + t'^{(1)}r^{(2)}r'^{(1)}t'^{(2)}, \tag{2.20b}$$

and the series converges to

$$r' = r'^{(2)} + t^{(2)}(1 - r'^{(1)}r^{(2)})^{-1}\ r'^{(1)}t'^{(2)}, \tag{2.21a}$$

$$t' = t'^{(1)}(1 - r^{(2)}r'^{(1)})^{-1}\ t'^{(2)}. \tag{2.21b}$$

The Eqs. (2.17), (2.19) and (2.21) determine the elements of the scattering system composed by the two scatterers.

2.1.1 Example: Normal-Superconductor junction

To illustrate the previous ideas, the problem of a Normal-Superconductor (NS) junction is considered. The resolution of this example will be useful to understand concepts and ideas presented mainly in Ch. 5. Figure 2.3 presents the profile of a potential Δ that allows to distinguish a normal region, where $\Delta = 0$ and a superconducting region where $\Delta = \Delta_0$. The interface is set at $x = 0$. Generally this potential is written as

$$\Delta(x) = \Delta_0\Theta(x)e^{i\phi},$$

with ϕ being the superconducting phase, only relevant when there are at least two superconductors. For our purposes now, it can be set to zero without lose of generality. Also, it will be

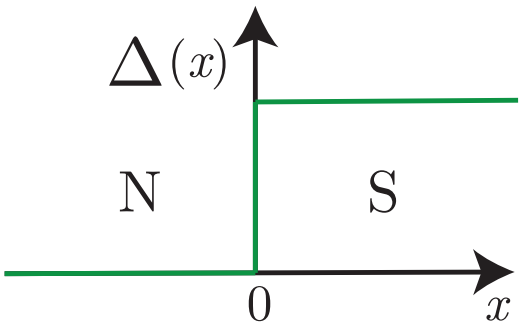

Figure 2.3: Model of a Normal-Superconductor (NS) interface with a gap potential $\Delta(x) \propto \Theta(x)$.

considered that both parts of the NS junction are semi-infinite. The system is modeled by the Bogoliubov-de-Gennes (BdG) equation [55, 63, 64],

$$\begin{pmatrix} \mathscr{H}_e & \Delta \\ \Delta^* & -\mathscr{H}_e^* \end{pmatrix} \begin{pmatrix} u \\ v \end{pmatrix} = E \begin{pmatrix} u \\ v \end{pmatrix}, \tag{2.22}$$

where u and v are the coherence factors and satisfy $u^2 + v^2 = 1$. For simplicity, will be considered particles that only move in the $\check{x}$ direction, perpendicular to the interface. It can be also considered

$$\mathscr{H}_e = -i\hbar v_F \frac{\partial}{\partial x}.$$

Each side of the junction admits a plane wave solution with wave vector $\vec{k}_N^{\pm} = \pm\frac{\varepsilon}{\hbar v_F}\check{x}$ for the normal side and $\vec{k}_S^{\pm} = \frac{\sqrt{\varepsilon^2-\Delta^2}}{\hbar v_F}\check{x}$ for the superconducting side. Here $\pm$ refers to (quasi) particles and (quasi) holes excitation. Applying the uniform solution to the left side of the junction it is found

$$\begin{pmatrix} u \\ v \end{pmatrix}_L = e^{ik_N^+ x} \begin{pmatrix} 1 \\ 0 \end{pmatrix} + a e^{ik_N^- x} \begin{pmatrix} 0 \\ 1 \end{pmatrix} + b e^{-ik_N^+ x} \begin{pmatrix} 1 \\ 0 \end{pmatrix}, \tag{2.23}$$

where the amplitude of the incident wave was set to one, a is the amplitude of a right moving hole and b is the amplitude of a left moving particle. On the superconducting side of the interface, the amplitudes are

$$\begin{pmatrix} u \\ v \end{pmatrix}_R = c e^{ik_S^+} \begin{pmatrix} U \\ V \end{pmatrix} + d e^{-ik_S^-} \begin{pmatrix} V \\ U \end{pmatrix}, \tag{2.24}$$

where the coherence factors U and V for a uniform superconductor are

$$U = \frac{1}{\sqrt{2}} \left(1 + \frac{\sqrt{\varepsilon^2 - \Delta^2}}{\varepsilon} \right) = \sqrt{\frac{\Delta}{2\varepsilon}}\, e^{\frac{1}{2}\arccos\frac{\varepsilon}{\Delta}}, \tag{2.25a}$$

$$V = \frac{1}{\sqrt{2}} \left(1 - \frac{\sqrt{\varepsilon^2 - \Delta^2}}{\varepsilon} \right) = \sqrt{\frac{\Delta}{2\varepsilon}}\, e^{-\frac{1}{2}\arccos\frac{\varepsilon}{\Delta}}. \tag{2.25b}$$

while c and d are the amplitude of a right-mover quasi-particle and left-mover quasi-hole respectively. Applying the boundary condition from Eq. (2.3) to Eqs.(2.23) and (2.24) it is found

$$1 + b = cU + dV; \tag{2.26a}$$

$$a = cV + dU; \tag{2.26b}$$

$$(1-b)k_N^+ = ck_S^+U - dk_S^-V; \tag{2.26c}$$

$$ak_N^+ = ck_S^+V - dk_S^-U, \tag{2.26d}$$

where the first two equations correspond to the continuity of the wave function and the last two ones correspond to the continuity of its derivative. Note that 2.26 is a linear set of four equations where the unknowns are the amplitudes a, b, c and d. The unique solution to this set of equations is

$$a = \frac{V}{U}; \tag{2.27a}$$

$$b = 0; \tag{2.27b}$$

$$c = \frac{1}{U}; \tag{2.27c}$$

$$d = 0, \tag{2.27d}$$

with U and V given by Eqs. 2.25. This result remains valid if the incident wave is a hole and regardless whether the energy ε is greater or smaller than the superconducting gap Δ_0. But in the particular case that $\varepsilon < |\Delta_0|$, then $|a|^2 = 1$ highlighting the fact that an incoming electron forms a Cooper pair in the superconductor side. The hole is annihilated and expelled back to the normal side as a reflected object. This process is called the Andreev reflection [63]. For a nice explanation on Andreev reflections the reader is deferred to Ref. [65–67] and references therein. For excitations on the superconducting side, for both quasi-electrons and quasi-holes it is found

$$a = -\frac{V}{U}; \tag{2.28a}$$

$$b = 0; \tag{2.28b}$$

$$c = \frac{\sqrt{\varepsilon^2 - \Delta^2}}{\varepsilon}\frac{1}{U}; \tag{2.28c}$$

$$d = 0. \tag{2.28d}$$

Recall that from Sec. 1.3.4, if $\varepsilon < 0$, the BdG equation satisfy a property known as particle-hole-symmetry [55, 58, 63, 64]. This is, if $\Psi_e = (u(x), v(x))^T$ is a solution for $\varepsilon > 0$, then also a solution is $\Psi_h = (v^*(x), -u^*(x))^T$ for $\varepsilon < 0$. Loosely speaking if it is changed the energy, due to the complex conjugation, it has to be changed the momentum and the particles moves backwards.

With this solved, we have now all the elements to compute our scattering matrix as in 2.5. Notice that for a superconductor it was needed to take into account left and right movers and the two types of particles. Therefore, our scattering matrix is now a 4×4 matrix. A frequently used

basis for the scattering matrix involving particles and holes is $\Psi = (\Psi_e; \Psi_h)^T$; so the $\mathbf{S}$ matrix becomes

$$\mathbf{S} = \begin{pmatrix} 0 & \frac{V}{U} & -\frac{\sqrt{U^2-V^2}}{U}\Theta(|\varepsilon|-\Delta_0) & 0 \\ -\frac{V}{U} & 0 & 0 & \frac{\sqrt{U^2-V^2}}{U}\Theta(|\varepsilon|-\Delta_0) \\ \frac{\sqrt{U^2-V^2}}{U}\Theta(|\varepsilon|-\Delta_0) & 0 & 0 & -\frac{V}{U}\Theta(|\varepsilon|-\Delta_0) \\ 0 & \frac{\sqrt{U^2-V^2}}{U}\Theta(|\varepsilon|-\Delta_0) & -\frac{V}{U}\Theta(|\varepsilon|-\Delta_0) & 0 \end{pmatrix}. \tag{2.29}$$

This matrix is obtained after identifying the amplitudes a, b, c and d with elements of the scattering matrix and normalizing it so that $|\det\mathbf{S}| = 1$. Note also the Θ function accompanying most of the elements. This is due to a physical reason that quasi-particles cannot be transmitted to the other side if they do not have energy greater than the gap. Two remarks can be made in this point. Firstly, the scattering matrix still respects the structure of Eq. (2.5), but now each block is a 2×2 matrix. For instance the block r has elements that represent the probability of an incoming electron (hole) being reflected as electron (hole) for the diagonal elements or being reflected as hole (electron) for the non diagonal elements. But the transmission block allows electrons (holes) to be transmitted as a hole (electron). Secondly, the Eqs.(2.17),(2.19) and (2.21) can be generalized to a matrix structure but it has to be taken into account the proper order of matrix multiplication. These two properties will be used in Ch. 5.

2.2 Landauer-Büttiker formula and Onsager theory in linear response regime

Once the scattering matrix is calculated, all the transport coefficients describing the charge, energy and heat currents can be calculated. To develop the theory a two-terminal device as depicted in Fig. 2.4 we will consider that each reservoir has its temperature and chemical potential defined, T_L, μ_L for the left reservoir and T_R, μ_R for the right reservoir.

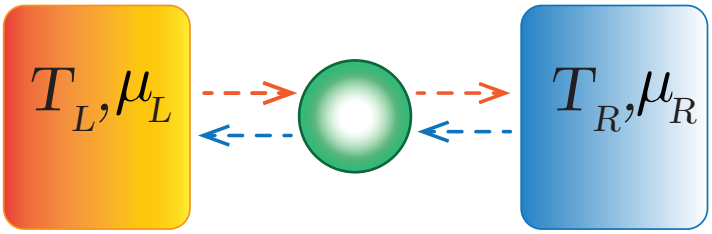

Figure 2.4: Two-terminal device with a central part. Each reservoir is at thermodynamic equilibrium. Left terminal is at temperature T_L and chemical potential μ_L while right reservoir is at temperature T_R and chemical potential μ_R.

Also, the device has a central region where the particles will be scattered from one terminal to the other, depicted with the green circle in the figure. To study the thermal coefficients, it is

often useful to define the **P**-matrix [68, 69] as

$$P_{i,j}^{\alpha,\beta} = |S_{i,j}^{\alpha,\beta}|^2 \tag{2.30}$$

with $\alpha,\beta = e,h$. Each element of the **P**-matrix represents the amplitude probability for a particle of type β to being reflected or transmitted as an $\alpha-$ type from channel j to i (for instance from left to right if there are two channels). The **P**-matrix is useful when there are at least two kinds of particles. Its structure is

$$\mathbf{P} = \begin{pmatrix} S^{++} & S^{+-} \\ S^{-+} & S^{--} \end{pmatrix} \tag{2.31a}$$

$$S^{\alpha,\beta} = \begin{pmatrix} r^{\alpha,\beta} & t'^{\alpha,\beta} \\ t^{\alpha,\beta} & r'^{\alpha,\beta} \end{pmatrix}. \tag{2.31b}$$

Note that due to the unitarity of the **S** matrix, the **P**-matrix satisfies

$$\sum_{\beta,j} P_{i,j}^{\alpha,\beta} = N_i^{\alpha}, \tag{2.32a}$$

$$\sum_{\alpha,i} P_{i,j}^{\alpha,\beta} = N_j^{\beta}, \tag{2.32b}$$

where N_i^{α} is the number of open channels for an $\alpha-$ type of particle form terminal i satisfying $N_i^{+}(\varepsilon) = N_i^{-}(-\varepsilon)$. The **P**-matrix also inherits the particle-hole symmetry from the scattering matrix. It is reflected mathematically as

$$P_{i,j}^{\alpha,\beta}(\varepsilon) = P_{j,i}^{-\alpha,-\beta}(-\varepsilon). \tag{2.33}$$

Also, time-reversal-symmetry yields to

$$P_{i,j}^{\alpha,\beta}(\varepsilon) = P_{j,i}^{\beta,\alpha}(\varepsilon). \tag{2.34}$$

Finally, the charge current density is defined as [68, 69]

$$\frac{2}{h}\sum_{j}\sum_{\alpha,\beta} e\alpha\left(f_i^{\alpha} - f_j^{\beta}\right)P_{i,j}^{\alpha,\beta}, \tag{2.35}$$

and, in this way, the charge current in the terminal i is

$$J_i^C = \frac{2e}{h}\sum_{j,\alpha,\beta}\int d\varepsilon\alpha\left(f_i^{\alpha} - f_j^{\beta}\right)P_{i,j}^{\alpha,\beta}. \tag{2.36}$$

Several remarks are in order here. When dealing with superconductors, such as the example of Sec. 2.1.1 or as it will be in Ch. 5, it is convenient to write all the negative energy states of an electron ε_e in terms of holes with positive energy $\varepsilon_h = -\varepsilon_e$. In this way the Fermi-Dirac distribution of each reservoir is written as

$$f_i^{\alpha}(\varepsilon) = \frac{1}{1+\exp\left(\frac{\varepsilon-\alpha\mu_i}{T_i}\right)}, \tag{2.37}$$

with $\alpha = \pm$ for electrons (holes) for $\varepsilon > 0$, where it was used the fact $f(-x) = 1 - f(x)$ and the substitution $\varepsilon \to -\varepsilon$. Then, the integration in Eq. (2.36) is performed over $0 < \varepsilon < \infty$ [68, 70, 71]. Also, we will focus on superconductors with equal chemical potentials which can be different from the ones of the normal terminal. This leads to a problem without time-dependent effects. When there is no need to deal with two types of particles, for instance when there is no superconducting terminals as is the situation considered in Chs. 3 and 4, Eq. (2.36) reduces to

$$J^C = \frac{2e}{h} \sum_j \int_{-\infty}^{+\infty} d\varepsilon \left(f(\varepsilon)_i - f(\varepsilon)_j \right) \mathscr{T}(\varepsilon), \tag{2.38}$$

with $\mathscr{T}(\varepsilon) = S_{21}^{++} = |t|^2$, being the transmission function. In the same way, the energy current is defined as

$$J_i^U = \frac{2}{h} \sum_{j,\alpha,\beta} \int d\varepsilon (\varepsilon \alpha) \left(f_i^\alpha - f_j^\beta \right) P_{i,j}^{\alpha,\beta}. \tag{2.39}$$

On the other hand, the heat current is defined as $J^Q = J^U - \mu J^C$. In a more compact way, both charge and heat currents can be written as

$$J_i^\xi = \frac{2}{h} \sum_{j,\alpha,\beta} \alpha^{\delta_{\xi,C}} \int d\varepsilon \left(f_i^\alpha - f_j^\beta \right) \left(\varepsilon - \mu_i \right)^{\delta_{\xi,Q}} \; P_{i,j}^{\alpha,\beta}, \tag{2.40}$$

where $\delta_{a,b}$ is the Kronecker delta function, and $\xi = C, Q$ for charge and heat current respectively. As the problem is time-independent, there are neither sinks and sources of particles nor external work is done. Then, charge and energy are conserved quantities, that is

$$\sum_i J_i^C = \sum_i J_i^U = 0. \tag{2.41}$$

But the heat is not. The sum over all the reservoirs is

$$\sum_i J_i^Q = -\sum_i \mu_i J_i^C. \tag{2.42}$$

This is the electrical power generated by the scatterer and it manifests the first law of thermodynamics for a steady-state flow. If the power is positive, it means that the scatterer absorbs heat from the electronic reservoirs turning it into electrical power. On the other hand, if the power is negative, then the scatterer absorbs electrical power from the electronic reservoirs and emits heat to them.

As a final remark it is often more useful to consider the heat current than energy current along with the charge one. Let us notice that, despite the latter is a conserved quantity, it depends on the choice of the zero of energy turning it gauge dependent and then into a non-physical relevant quantity. This is not the case with the heat current that does not depend on the choice of the zero energy and then is a thermodynamical relevant quantity.

2.2.1 Onsager theory of linear response

It was already seen that the elements of the scattering matrix can be used to calculate the transport coefficients via the **P**-matrix. We now discuss some useful properties that will be needed in the development of the forthcoming chapters.

Let us consider again a two-terminal device with a central part as shown in 2.4, but operating under small differences in the temperature and in the chemical potential, that is $T_L = T + \Delta T$; $T_R = T$, with $\Delta T > 0$ and $\mu_L = \mu$; $\mu_R = \mu + \Delta\mu$, with $\Delta\mu > 0$. We also consider, for sake of simplicity, the system does not mix electrons and holes, so we can consider the flux of one kind of particles. This means that Eq. (2.38) will be used to calculate the charge current. For more general statements with a superconducting terminal, the reader is deferred to Refs. [58, 69–73]. In linear response, the charge and heat currents read

$$J^C = \mathscr{L}_{11} X_C + \mathscr{L}_{12} X_Q, \tag{2.43a}$$

$$J^Q = \mathscr{L}_{21} X_C + \mathscr{L}_{22} X_Q. \tag{2.43b}$$

The coefficients $\mathscr{L}_{i,j}$ define the so-called Onsager matrix **L** and they can be written as

$$\mathscr{L}_{i,j} = -T e^{4-i-j} \int_{-\infty}^{+\infty} \frac{d\varepsilon}{h} \frac{\partial f}{\partial \varepsilon} \left(\varepsilon - \mu\right)^{i+j-2} \mathscr{T}(\varepsilon) \tag{2.44}$$

with $\mathscr{T}$ being the transmission function. The $X_{C,Q}$ are the generalized thermodynamic forces that appear from linear order expansion in the difference of Fermi-Dirac functions. They are

$$X_C = \frac{\Delta\mu}{T}, \tag{2.45a}$$

$$X_Q = \frac{\Delta T}{T^2}. \tag{2.45b}$$

The coefficients of the Onsager matrix **L** are not independent. By the second law of thermodynamics, the entropy flux rate must be positive. In terms of the linear-response fluxes [59], it reads

$$\dot{\mathscr{S}} = X_C J^C + X_Q J^Q = X_C^2 \mathscr{L}_{11} + X_Q^2 \mathscr{L}_{22} + (\mathscr{L}_{12} + \mathscr{L}_{21}) X_C X_Q. \tag{2.46}$$

Note that the entropy flux rate is a quadratic function on both generalized forces, X_C and X_Q. This implies that $\mathscr{L}_{ii} > 0$ and also $\det\mathbf{L} > 0$.

There is also another constraint imposed by time-reversal-symmetry. In the presence of a magnetic field $\vec{B}$ the elements must satisfy

$$\mathscr{L}_{\alpha,\beta}(\vec{B}) = \mathscr{L}_{\beta,\alpha}(-\vec{B}), \tag{2.47}$$

so that the laws of physics remain unchanged if time is flipped. In this way, the diagonal elements of the Onsager coefficients must be even functions of the magnetic field, while the non diagonal

can have any dependence. Finally, to end this subsection, we present the relations between the Onsager and the transport coefficients

$$G = \left.\frac{J^C}{\Delta V}\right|_{\Delta T=0} = \frac{\mathscr{L}_{11}}{T}; \tag{2.48a}$$

$$\kappa = \left.\frac{J^Q}{\Delta T}\right|_{J^C=0} = \frac{1}{T^2}\left(\mathscr{L}_{22} - \frac{\mathscr{L}_{21}\mathscr{L}_{12}}{\mathscr{L}_{11}}\right); \tag{2.48b}$$

$$S = -\left.\frac{\Delta V}{\Delta T}\right|_{J^C=0} = \frac{1}{T}\frac{\mathscr{L}_{12}}{\mathscr{L}_{11}}; \tag{2.48c}$$

$$\Pi = \left.\frac{J^Q}{J^C}\right|_{\Delta T=0} = \frac{\mathscr{L}_{21}}{\mathscr{L}_{11}}, \tag{2.48d}$$

where G is the electrical conductance, κ is the thermal conductance, S is the Seebeck coefficient, where the voltage bias that it develops, is called the voltage thermopower, V_{TP}, and Π is the Peltier coefficient. With these definitions, the currents of Eq. (2.43) can be expressed as

$$J^C = G\Delta V + GS\Delta T; \tag{2.49a}$$

$$J^Q = G\Pi\Delta V + (\kappa + GS\Pi)\Delta T. \tag{2.49b}$$

2.2.2 Efficiency and Figure of merit: general remarks

The efficiency of any system is calculated as the ratio of what is gained over what is invested in a given operation. For a heat engine we have

$$\eta = \frac{P}{J^Q} = \frac{-\Delta\mu/eJ^C}{J^Q} = -TX_C\frac{\mathscr{L}_{11}X_C + \mathscr{L}_{12}X_Q}{\mathscr{L}_{21}X_C + \mathscr{L}_{12}X_Q}, \tag{2.50}$$

where $P = -\Delta\mu/eJ^C > 0$ is the gained power investing an amount of heat at a rate J^Q. Maximizing this expression for X_C, for a given X_Q we get

$$X_C = -\frac{\mathscr{L}_{22}}{\mathscr{L}_{21}}\left(1 - \sqrt{\frac{\det\mathbf{L}}{\mathscr{L}_{22}\mathscr{L}_{11}}}\right), \tag{2.51a}$$

$$\eta^{\mathrm{he}}_{\mathrm{max}} = \frac{\sqrt{ZT+1}-1}{\sqrt{ZT+1}+1}, \tag{2.51b}$$

$$ZT = \frac{\mathscr{L}_{21}\mathscr{L}_{12}}{\det\mathbf{L}}, \tag{2.51c}$$

where ZT is the figure of merit and η_C is the Carnot efficiency $\eta_C = \Delta T/T$. Note that the maximum efficiency is an increasing function of ZT and it is bounded by η_C [74].

For a refrigerator the efficiency is

$$\eta^{\mathrm{ref}} = \frac{J^Q}{P}, \tag{2.52}$$

where now J^Q and P are both negative, indicating that it is invested power in the system in order to remove the heat current from the cold reservoir. With the same procedure as before, one

concludes that the maximum achievable efficiency is

$$\eta_{\max}^{\text{ref}} = \frac{1}{\eta_C}\frac{\sqrt{ZT+1}-1}{\sqrt{ZT+1}+1}, \tag{2.53}$$

with the same figure of merit as before.

Another quantity that can be maximized is the power generated to a given X_Q in the heat-engine operation. Recall that the generated power is calculated as

$$P = -\frac{\Delta\mu}{e}J^C = -TX_C\left(\mathscr{L}_{11}X_C + \mathscr{L}_{12}X_Q\right), \tag{2.54}$$

and it is maximum for a fixed X_Q when $X_C = -\frac{\mathscr{L}_{12}}{\mathscr{L}_{11}}X_Q$, leading to a maximum power

$$P^{\max} = \frac{\eta_C}{4}\frac{\mathscr{L}_{12}^2}{\mathscr{L}_{11}}X_Q = \frac{1}{4}S^2G(\Delta T)^2. \tag{2.55}$$

Finally, for systems with time-reversal-symmetry, the efficiency at maximum power reads as

$$\eta\left(P^{\max}\right) = \frac{\eta_C}{2}\frac{ZT}{ZT+2}. \tag{2.56}$$

Note that the expression of Eq. (2.56) is valid whether the system is working as a heat engine ($\eta_C = \Delta T/T$) or a refrigerator ($\eta_C = T/\Delta T$). Note also that the maximum efficiency at maximum power is bounded by $\eta_C/2$ when $ZT \to \infty$.

All the needed theory to understand the present thesis was already introduced in this chapter. In the following chapters we will apply this formalism to analyze nanostructures based on the systems introduced in chapter 1.

CHAPTER 3

STUDIYNG QHE IN THE CORBINO GEOMETRY

After presenting the systems to be considered, this chapter will be devoted to model and analyze measurements in a quantum Hall regime of a Corbino disk, similar to the one introduced in Sec. 1.1. More precisely, the focus will be on thermoelectric measurements. The idea behind this kind of experiments is simple, one edge or terminal has a thermal bias and the charge flow that is generated is measured. An illustration is presented in Fig. 3.1 for both bar, panel (a), and Corbino disk, panel (b), configurations.

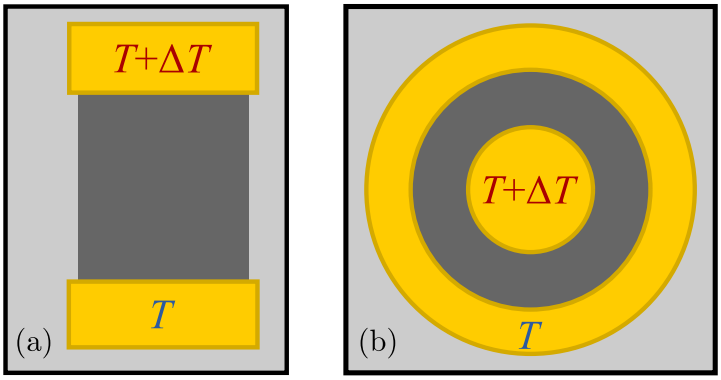

Figure 3.1: The two sample designs to investigate thermoelectric effects, Hall-bar (a) and Corbino (b). The dark gray areas are the 2DES. The hot and the cold contacts for measuring the thermovoltage are at two ends of the rectangular shaped Hall-bar. For the Corbino, the hot contact is in the center of the 2DES which is surrounded by the cold one.

Measurements of the thermopower developed in this regime would allow one to access the entropy of the system and then, lead to a better understanding of the non-Abelian quasiparticles of some fractional filling factors [75–78]. Nevertheless, although thermoelectricity has been studied in Hall-bar, both theoretically and experimentally, theories based on electron diffusion

could not reconcile with the experimental observations [79–82]. The effect of phonon drag was suggested as an explanation [79, 81, 82], but recently inherent problems due to the topology of the Hall-bar geometry affecting both phonon-drag and electron diffusion, have been pointed out [77].

In the Corbino geometry, the longitudinal thermopower can be measured directly. Due to the circular design, the thermal bias is applied radially, hence, the thermal and electrical transport is induced along the radial direction and then, the transport takes place through the bulk [83].

In this chapter we will study the thermopower devoloped in the quantum Hall regime of a sample with Corbino geometry treating it as a two-terminal device where a thermal gradient is applied, standing in the same framework developed in chapter 2. To get the thermal bias in the Corbino sample, a heater was added in the center, so that the thermal gradient could be set in both the substrate and the two-dimensional electron system (2DES). Results at temperatures from about 300 mK to 2 K are presented and compared with theoretical results, where both the electrical conductance and the thermovoltage are modeled based upon the same transmission function as it was introduced in Sec. 2.2. A very good agreement over a wide range of magnetic-fields and temperatures is found. This demonstrates that the substantial disagreement which was typical for Hall bars can be removed by using the Corbino topology. In contrast to Hall-bar studies, it is not necessary to consider phonon-drag in the theory in order to explain a good agreement with the experimental data.

This chapter is organized as follows, in Sec. 3.1 experimental details concerning the set-up and the measurements will be presented. Then, in Sec. 3.2 the measurements of the electrical conductance and voltage thermopower at different range of magnetic-field, temperature and power delivered are presented. In Sec. 3.3 two models to fit the data in two different ranges of magnetic-field are considered. The modeling predicts superbly both electrical conductance and voltage thermopower. It also predicts well the thermal gradient developed, discussed in Sec.3.4. The thermoelectric performance in terms of the figure of merit is presented in Sec. 3.4.1. Finally, conclusions are presented in Sec. 3.5.

3.1 Samples details and experimental set-up

The experimental setup used for the measurements is presented in Fig.3.2. A thin-film heater made of AuPd is inserted in the center of the Corbino samples. An AC current at frequency f of few Hz is applied in the heater, producing a temperature oscillation of $2f$. In this way, a radial thermal gradient between the center and the external edge of the sample, assumed to be at the temperature T close to the one of the bath is induced. The used device is presented in Fig. 3.2 (a). It consists of five concentric ohmic contact rings with diameters ranging from 0.4 mm to 3.2 mm. They were made by making an alloy with Au-Ge-Ni into the 2DES structure forming four independent Corbino rings. The heater is shown at left of 3.2(a). Under the heater

and outside of the rings the 2DES is removed. A sketch of the cross-section is presented in panel (c). It is assumed that the local temperature over the 2DES follows the one of the underlying GaAs substrate. This was already verified by Chickering et al. [84, 85] down to much lower temperatures than the ones used here. Any possible anisotropies in the heat conductivity of the substrate is neglected, due to the ballistic nature of the phonons because these become only relevant if the dimension of the heater and the contacts are much smaller than the substrate thickness [86].

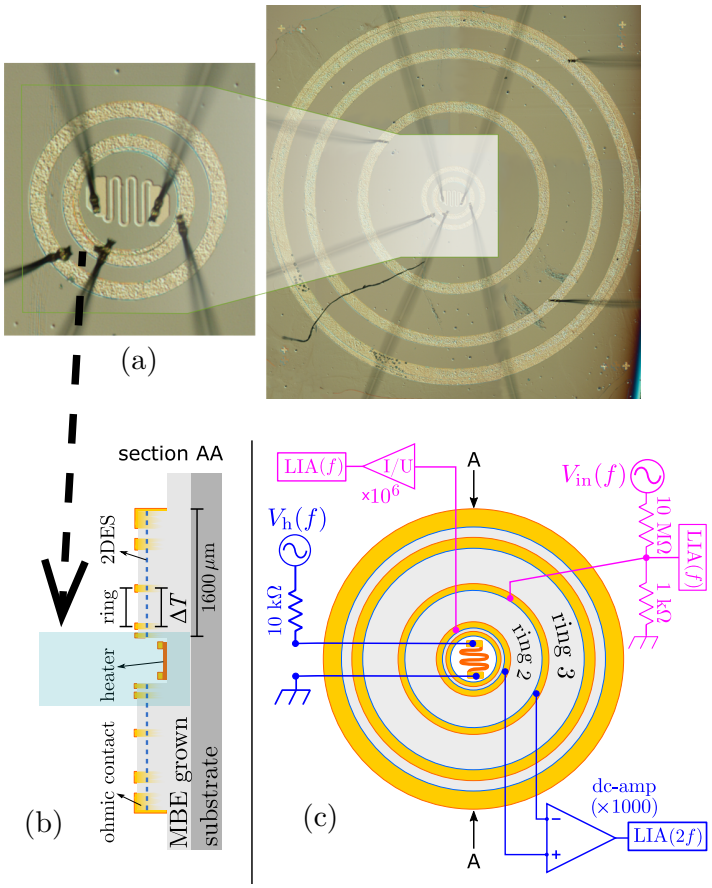

Figure 3.2: (a) Right, a sample with five concentric rings. Left, zoom of the heater design. (b) Cross-section of the sample, notice that the heater element is over the substrate outside the 2DES. The heater area is highlighted in light blue. (c) Measurement configurations for the conductance and the thermovoltage are shown in magenta and blue, respectively. LIA denotes lock-in amplifier. Each measurement and therefore each circuit were done separately. Only two of the four Corbino rings are labeled in the figure.

The samples were grown by molecular beam-epitaxy on GaAs wafers having a single 2DES located in a 30 nm-wide quantum-well with Si-doped layers on both sides. Data of two samples from two wafers, A and B are presented here. Separate test pieces from these wafers in Van-der-Pauw geometry had mobilities of $21 \times 10^6\,\mathrm{cm^2\,V^{-1}\,s^{-1}}$ and $18 \times 10^6\,\mathrm{cm^2\,V^{-1}\,s^{-1}}$ at electron densities of $n_e = 3.06 \times 10^{11}\,\mathrm{cm^{-2}}$ and $n_e = 2.0 \times 10^{11}\,\mathrm{cm^{-2}}$ for sample A and B respectively, measured at 1.3 K in the dark.

The Corbino samples were glued in a standard commercial ceramic-holder with gold-plated pins base and a 3 mm diameter hole drilled in the middle to reduce thermal contact to the samples. The measurements were performed in vacuum in a ^{3}He cryostat equipped with a 14T magnet being able to achieve a base temperature of 250 mK.

Figure 3.2(c) presents the configurations used for the measurements of the conductance, magenta circuit, and of the thermovoltage, blue circuit. The conductance G was measured by applying an AC voltage through a voltage divider and measuring the current with an amplifier (IUAmp). The thermovoltage V_{TP} was measured in separate runs by passing an AC current of frequency f to the central heater having a resistance of about 60 Ω. The thermopower induced in the sample was measured by using a $\times$1000 differential DC voltage amplifier (DCamp). The input impedance of this amplifier must be very high because the internal resistance of the Corbino device diverges in the quantum-Hall states. The impedance of the used amplifier was about 1 TΩ [87]. Very little frequency dependence of the thermovoltage was found in the range of 3 Hz to 100 Hz. Because of convenience, most of the measurements were done at 13.8 Hz. To avoid effects of time-dependent magnetic fluxes, the waiting time for each data point was set to a few seconds to guarantee the stabilization of the magnetic-fields at a constant value.

3.2 Measurements and data fitting

Figure 3.3 presents the conductance of the Corbino disk (solid orange line) and its voltage thermopower (solid light blue line) for a base temperature (temperature of the thermal bath) of T =269 mK and an applied heater power of P =277 nW for sample A. The top panel is for a range of 0.3 T to 1 T. It presents the characteristic Shubnikov-de-Haas (SdH) oscillations at low magnetic-field [88–92]. Note that the spin-splitting becomes visible at $B \simeq 0.9$ T and then the conductance reaches zero at $\nu = 16$. The lower panel presents measurements for a range of 1.4 T to 5 T. For this range of magnetic-field, the maxima of the conductance coincides with the Landau levels. This separation was made for the different models used in each region (dashed lines in the Fig.), that will be explained in the next section.

In both situations appears a sign change in the V_{TP} with a periodicity that coincides with the one of the local maxima of G. This sign change was already reported in previous measurements with the Corbino geometry [93], but it was not the case for the bar geometry despite it had been predicted theoretically [78].

Measurements of V_{TP} in sample B are presented in Fig. 3.4. Here the response for each ring (2,3 and 4) was measured at a bath temperature of 600 mK and a heater power of 213 nW. Again, the oscillatory behavior is present corresponding to the conductance local maxima and minima.

The large signals of V_{TP} that appear, are in the gap between two consecutive Landau levels. They are reproducible and they persist even when the magnetic-field is fixed and kept constant or when the direction of the sweep of the magnetic-field is reversed. They vanish only when a DC

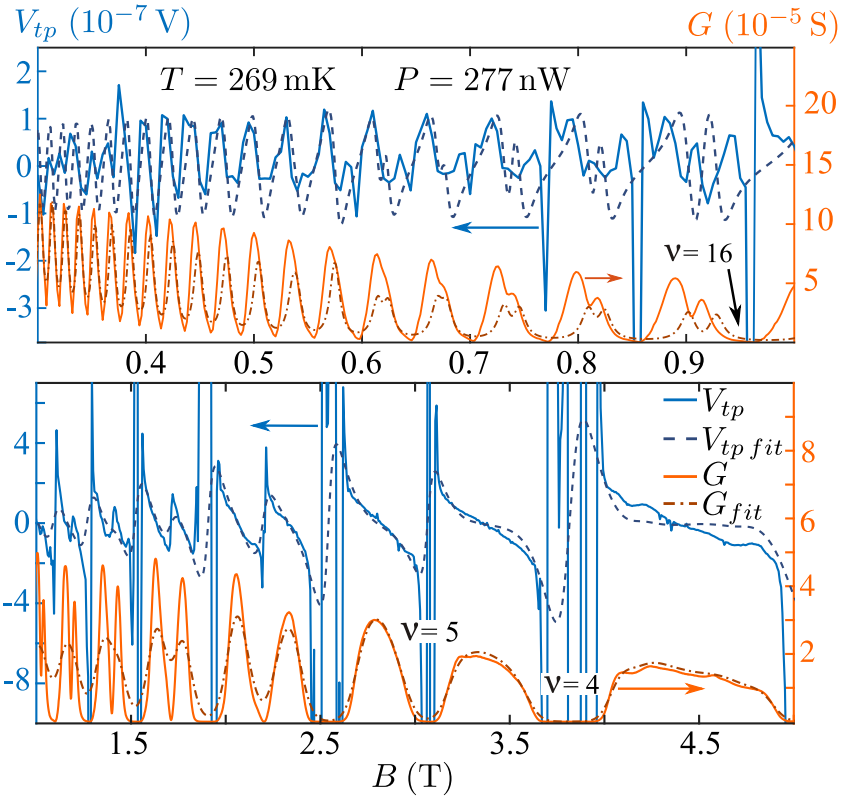

Figure 3.3: Conductance G and thermovoltage V_{TP} as a function of the magnetic-field B for the ring 2 in Fig. 3.2 at temperature T =269 mK with power P =277 nW supplied by the heater for sample A (mobility of $21 \times 10^6\,\mathrm{cm^2\,V^{-1}\,s^{-1}}$ and $n_e = 3.06 \times 10^{11}\,\mathrm{cm^{-2}}$). Experimental data is plotted in solid lines and their respective fits are in dashed lines. Each panel was calculated with its respective transmission function.

current is applied on top of a square AC current, leading to a constant heating and a vanishing temperature oscillation. We can therefore conclude that the large value of the signal is thermally induced and it is not produced by an electromagnetic crosstalk.

3.3 Modeling the transmission function

In this section we will analyze the thermal voltage for only partially filled Landau levels, not for the gap. It is convenient to separate in low and high magnetic-field regions. The reason for this separation will be explained below.

3.3.1 Low magnetic-field region

In the low magnetic-field region the main hypothesis is that the electrons are affected by disorder and not by many-body interactions. Therefore, the transmission function $\mathcal{T}$ can be modeled as

$$\mathcal{T}(\varepsilon) = \Lambda \sum_{n,\sigma} \frac{(n+1)\,\omega_c^2}{8\pi h} A_{n,\sigma}(\varepsilon) A_{n+1,\sigma}(\varepsilon), \tag{3.1}$$

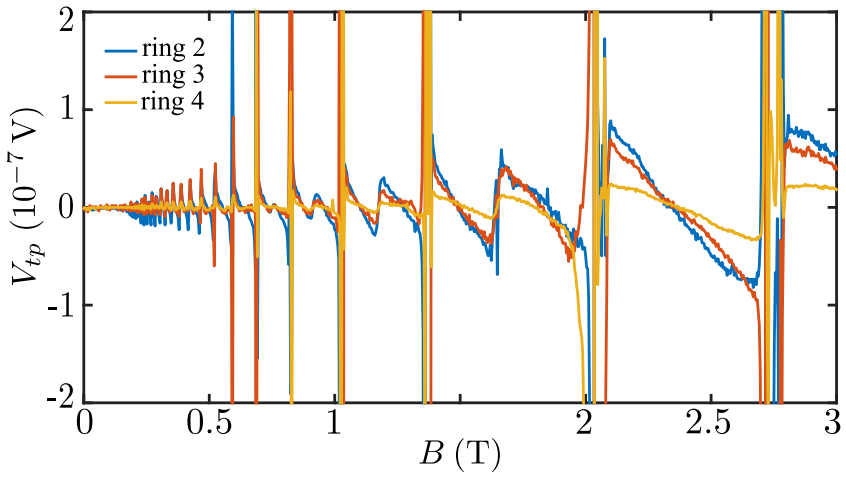

Figure 3.4: Voltage thermopower V_{TP} for sample B (mobility of $18\times10^{6}\,\mathrm{cm^2V^{-1}s^{-1}}$ and n_e = $2.0\times10^{11}\,\mathrm{cm^{-2}}$) as a function of the magnetic-field B. Each line represents a measurement for each ring. Measurements were made at a bath temperature of 600 mK and a heater power of 213 nW. Note that since ring 2 and 3 present a larger thermal gradient than ring 4 they present a larger response.

being Λ a geometric factor relating the conductance to the conductivity, $A_{n,\sigma}(\varepsilon) = \mathrm{Im}\left[G_{n,\sigma}(\varepsilon)\right]$, with $G_{n,\sigma}(\varepsilon) = \left[\varepsilon - \varepsilon_{n,\sigma} - \Sigma(\varepsilon)\right]^{-1}$, being the Green function calculated within the self-consistent Born approximation. $\varepsilon_{n,\sigma} = \hbar\omega_c(n+1/2) \pm \mu_B B/2$ is the energy of the Landau level, including the Zeeman splitting, with $\pm$ corresponding, respectively, to spin up and down. Here, μ_B is the Born magneton, $\omega_c = eB/m^*$ is the cyclotron frequency, and $m^* = 0.067m_e$ is the effective mass of the electrons in the structure and m_e is the electron mass. The effect of disorder due to impurities introduces a widening Γ in the Landau levels, which is accounted for the self-energy $\Sigma(\varepsilon) = (\varepsilon-\varepsilon_L)/2 - i\Gamma\sqrt{1-(\varepsilon-\varepsilon_L)^2/(4\Gamma^2)}$. Here ε_L is the energy of the Landau level which is closest to ε. Note that there are two parameters to be fit, Λ and Γ. The model presented in Eq. (3.1) was already introduced by Johnson et. al. in Ref. [94] and also used by Barlas et. al. in Ref. [77].

With the transmission function, it can be calculated all the Onsager elements as stated in Eq. (2.44) as

$$\mathscr{L}_{ij} = -e^{4-i-j}\frac{T}{h}\int_0^\infty d\varepsilon \frac{\partial f}{\partial \varepsilon}\left(\varepsilon-\mu\right)^{i+j-2}\mathscr{T}(\varepsilon,B), \tag{3.2}$$

where B is the magnetic-field in the direction perpendicular to the plane of the sample. We found out experimentally that the model presented in Eq. (3.1) fits superbly the data of both G and V_{TP} presented in the top panel of Fig. 3.3, that is, predicts correctly the observed electrical conductance and reproduces the same oscillations and periodicity in the SdH as in the measurements. Particularly, the lower the magnetic field is, the better the fit is. However, this model is quite simple and, as the magnetic-field is increased (compare for instance the fit for $B = 0.4$T and $B = 0.9$T), it fails to reproduce the observed data in both G and V_{TP}. This is in part due to the fact that the hypothesis of the absence of many-body interaction does not hold. We will briefly discuss this and present a different model in the following section.

3.3.2 High magnetic-field region

As the magnetic-field is increased, the hypothesis of the previous section are no longer valid. This can be seen for instance at $B \simeq 0.9\text{T}$ where the model based on Eq.(3.1) does not predict well the observed behavior neither in G nor V_{TP}. We can trace back this problem to the fact that the self-consistent Born approximation used in the previous section only takes into account the effects of disorder. Despite it is a good approach to threat metals with low disorder and with weak interactions, with high magnetic fields a 2DES becomes strongly interacting and consequently the picture of electrons affected only by disorder approximation does not hold anymore [15, 16]. For example, the interactions are crucial in the FQHE that was already observed in samples with similar electron density but at lower temperatures [95–97]. A microscopic model for this situation would turn out to be very complicated and would be out of the scope of the present work. Nevertheless, it is reasonable to assume that there exists a transmission function that takes interactions into account [98, 99] from which we can calculate the transport coefficients with Eq. (3.2).

Therefore for high magnetic-fields, the strategies is to *infer* the transmission function from the experimental data instead of calculating it from a microscopic model. To this end, we used the fact that in linear response regime in the limit of zero temperature, $\mathscr{T}$ tends to the electrical conductance. That is because,

$$\lim_{T\to 0} -\frac{\partial f}{\partial \varepsilon} \to \delta(\varepsilon - \mu),$$

therefore, for low temperatures, such that $k_B T \ll \Gamma, \hbar\omega_c$, the transmission function becomes

$$\mathscr{T}(\mu_\nu) \sim \frac{G(\mu_\nu)}{e}, \tag{3.3a}$$

$$\mu_\nu = \frac{\hbar e B}{2m^*}, \quad B_{\nu+1} < B < B_\nu, \tag{3.3b}$$

where $B_\nu = n_e h/(e\nu)$ is the magnetic-field corresponding to the filling fraction ν, while μ_ν is the Fermi energy for the range of B within two consecutive integer filling factors.

In summary, the procedure is to get the transmission from the lowest temperature measurement of the electrical conductance and then use Eq. (3.2) to calculate the transport coefficients at any other (higher) temperature. Recall that our aim is to model the transport coefficients for *partially filled Landau levels*. The response in the gap is out of scope for the moment, which means we are not aiming now to explain the large signals in the V_{TP} that occur in the gap. Nevertheless, with this procedure, we could fit the data very accurately in the regions of partially filled Landau levels, as can be seen in the lower panel of Fig. 3.3 with the magnetic field ranging from 1 T to 5 T.

3.4 Determining the thermal gradient

The voltage thermopower is written in terms of the Onsager coefficients as

$$V_{\mathrm{TP}}(B) = -S(B)\frac{\Delta T}{T}, \tag{3.4}$$

being the Seebeck coefficient $S = \mathscr{L}_{12}/\mathscr{L}_{11}$. In this way, given $\mathscr{T}$ from the fitting of G and therefore every Onsager coefficient, we can estimate the thermal gradient of each measurement adjusting the ratio $\Delta T/T$. For instance in Fig. 3.3, for the low magnetic-field region, the temperature bias we estimate is $\Delta T = 1\,\mathrm{mK}$ whereas, for the high magnetic-field region is 1.08 mK. Figure 3.5 presents an example of the region of high magnetic-field, $B = 2.21\,\mathrm{T}$ to 2.46 T for the upper panel and 2.625 T to 3 T.

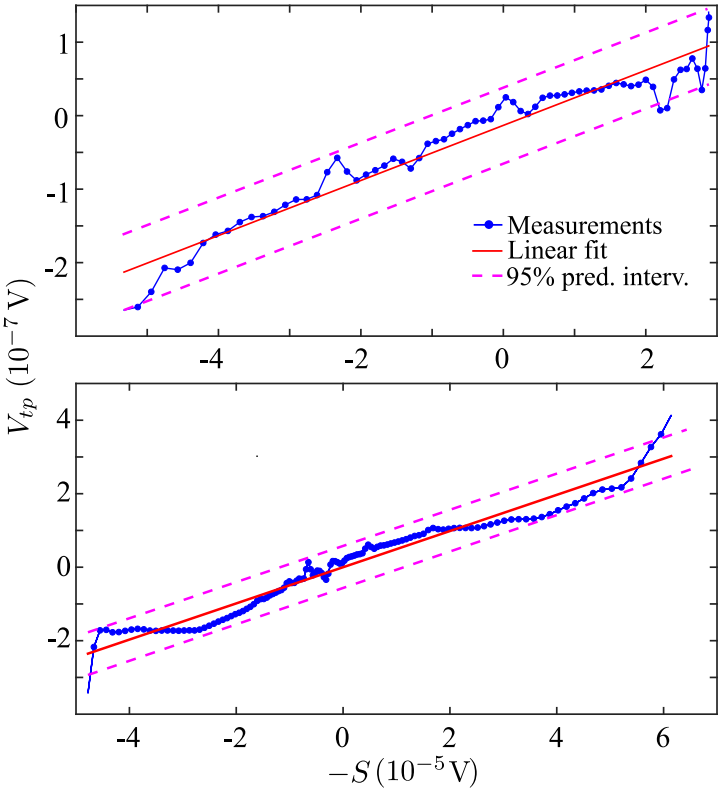

Figure 3.5: Measured V_{TP} as function of the calculated $-S$ within the range of $B = 2.21\,\mathrm{T}$ to 2.46 T (upper panel) and 2.625 T to 3 T (lower panel).

With an accuracy corresponding to a 95% we get $\Delta T = 1.01(6)\,\mathrm{mK}$ for the upper panel and ΔT 1.33(6) mK lower panel. While for sample B measured at a bath temperature of 600 mK as presented in Fig. 3.4 the fit gives a result for $\Delta T = 60(3)\,\mu\mathrm{K}$ for ring 2, for ring 3 $\Delta T = 110(10)\,\mu\mathrm{K}$ and for ring 4 $\Delta T = 74(50)\,\mu\mathrm{K}$. This result is significantly lower to sample A. The reason is that the thermal conductivity of the substrate increases with T^3 and at 600 mK the temperature gradient will be nearly 10 times smaller and, correspondingly, a much smaller temperature difference is expected at higher temperatures.

Overall, in particular for high magnetic-fields, the agreement between experiment and theory is excellent within the range of B corresponding to partially filled Landau levels, for which the electrical conductance is not null. With this good agreement between experimental and theoretical estimates of the temperature difference ΔT found analyzing the data of Fig. 3.3, it is possible to analyze the relation between the electrical power supplied at the heater and ΔT. As the experiment is done at very low temperatures, so that there is only electronic response in the system, so that we can assume that the system thermalizes fast enough to achieve the same temperature of the bath, and the bias applied are small enough to consider the linear response regime, it is natural to assume a linear relation between the electrical power, P, and ΔT or in other words

$$\frac{\Delta T(P)}{P} = \text{constant}. \tag{3.5}$$

Hence, knowing the thermal gradient only once and knowing the power supplied, it can be calculated ΔT at any power considered. For instance, using the power supplied for $\Delta T = 1.08\,\text{mK}$, this can be used in Eq. (3.5) to calculate the thermal gradient for any supplied power P as

$$\Delta T(P) = \frac{P}{277\,\text{nW}} 1.08\,\text{mK} \tag{3.6}$$

This analysis is presented in Fig. 3.6. The same Seebeck coefficient was used in all the measurements, and the bath temperature was kept fixed at 260 mK. Again, it can be seen good agreement between experimental data (solid lines) and theoretical prediction (dashed lines).

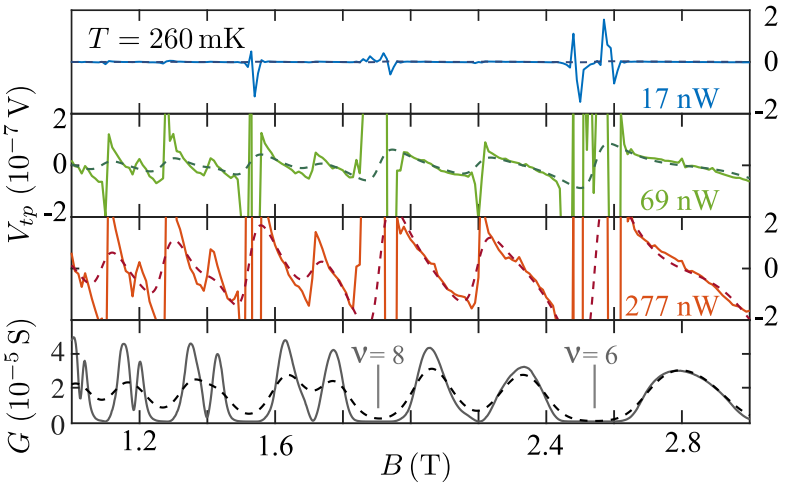

Figure 3.6: Thermovoltage V_{tp} for a fixed temperature and different powers P' applied at the heater, assuming $\Delta T(P') = P'/P\ 1.08\,\text{mK}$. P and other details are the same as in Fig. 3.3.

In Fig. 3.7 is presented the V_{TP} for the high magnetic-field region. Each panel corresponds to a different bath temperature in ranges from 269 mK to 1.5 K. In the first five panels, the power used was of 277 nW, while in the last two, it was 433 nW. As in the previous figures, solid lines is the experimental data and dashed lines correspond to the theoretical estimate. The

agreement between the theoretical predictions and the experimental data for magnetic-fields corresponding to partially filled Landau levels within a wide range of temperature is overall very good, improving as the temperature decreases.

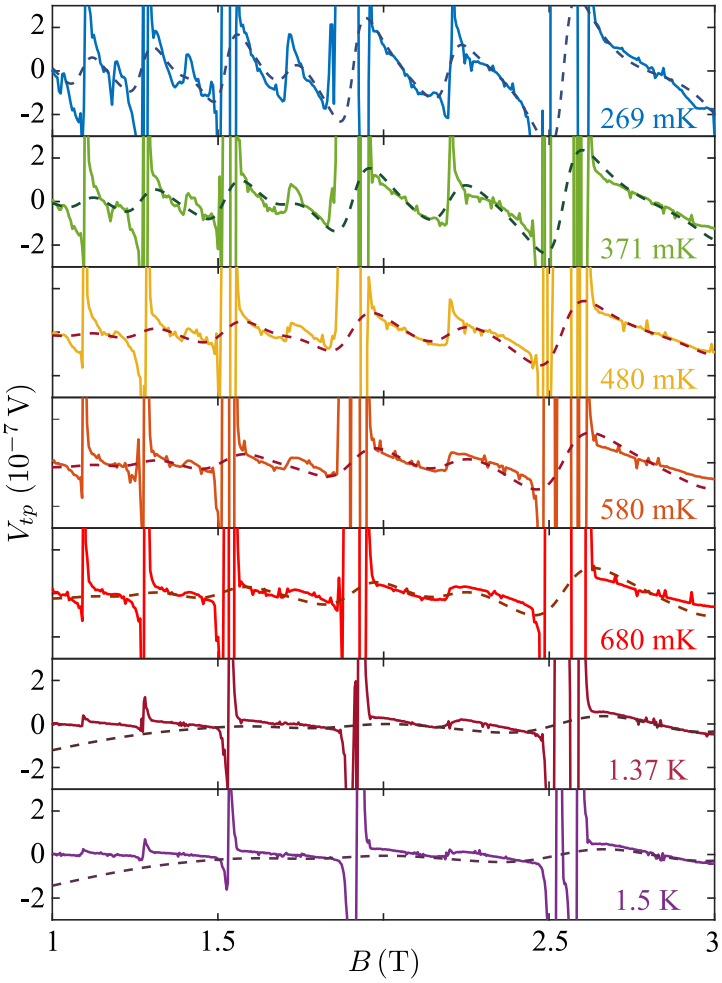

Figure 3.7: Thermovoltage $V_{\rm tp}$, as function of the magnetic-field. Each panel corresponds to a different temperature. In the case of 269 mK to 680 mK a power of 277 nW was used, while for 1.37 K to 1.5 K the heater power was 433 nW. Other details are the same as in previous Figs. The scale for $V_{\rm tp}$ is the same in all panels.

3.4.1 Thermoelectric performance

As stated in Sec. 2.2.2, the performance of a system taking into account only the electron contribution to transport can be parametrized by the figure of merit $ZT = \mathscr{L}_{12}^2/\det\mathbf{L}$ for both situations, heat engine and refrigerator. The calculation is straightforward once $\mathscr{T}$ is known. Figure 3.8, top panel, presents ZT as a function of the magnetic-field where each line corresponds to a different temperature. The lower panel of the Fig. presents the transmission function of the systems as function of ε in units of $\hbar e/2m^*$.

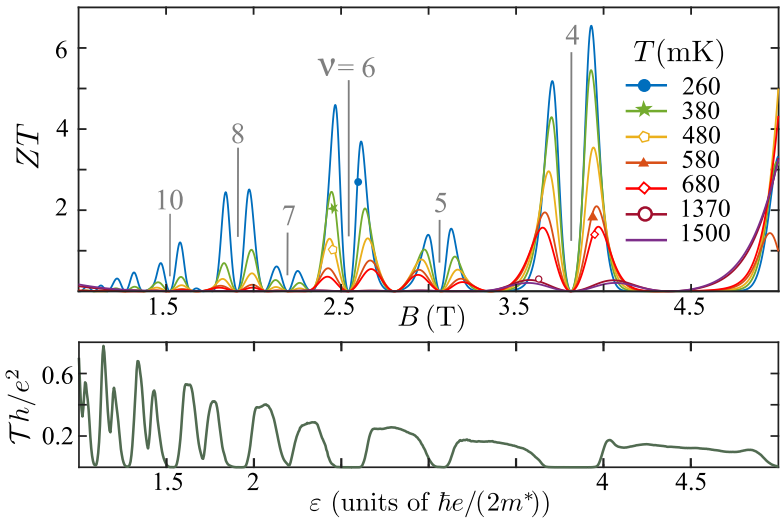

Figure 3.8: Figure of merit ZT as function of B (top panel) and transmission function (bottom panel) in function of ε in units of $\hbar e/2m^*$. Each line in ZT corresponds to a different temperature.

It can be seen that the thermoelectric performance in the Corbino device under the QH regime is surprisingly high, comparable with the highest values reported up to the date based upon ballistic transport. The highest reported values, semiconductors in general, are in the range $1 \leq ZT \leq 2.7$ [68, 100], while some optimistic theoretical calculations predict $ZT \leq 4$ [101] for systems based on edge channel ballistic transport.

The transmission function presented in Fig. 3.8, only takes into account the electronic contribution and it was enough to fit the experimental data presented in Fig. 3.3. The sequence of sharp features at the Landau levels, corresponding to the high magnetic-field regime, works out as an energy filter, leading to large values of ZT, which reaches values close to 6 for $\nu = 4$ ($B \simeq 3.75$). Thus, diffusive transport across the bulk of a Corbino device has a potentially higher performance than the envisioned edge channel devices. Note also that ZT decreases with the temperature, so this may lead us to think that for lower temperatures higher values could be reached, but in order to calculate that it would be needed lower temperatures measurements so the electrical conductance would become a better estimator of the transmission function.

3.5 Conclusions of this chapter

In this chapter, the experimental thermoelectric response of a Corbino ring was studied. The theoretical interpretation was based on the hypothesis of linear response and diffusive transport. The analysis carried out here relied on the assumption that the main contribution to the transport is due to the electrons. Phononic thermal transport in the substrate would tend to decrease the performance but this contribution would die out at low temperatures with a temperature dependence of T^3, while the figure of merit would probably increase. Therefore, it could be envisioned that a Corbino device could be used as a themoelectric cooler in the low temperature

regime, for instance few mK, for specific purposes by replacing the heater with an object to be cooled for instance. A specific analysis of the cooling properties was reported in Ref. [102].

For partially filled Landau levels it was found an excellent agreement between the data and the theoretical description neglecting any kind of interaction with phonons. What is more astonishing, with this framework, results in range from T =300 mK to 2 K could be predicted. Despite electron-phonon interaction may exist, the transfer of momentum between them does not lead to a measurable voltage. In fact, it was already noted that contribution of the phonon-drag mechanism to the thermoelectric coefficient $\mathscr{L}_{12}$ should be zero in the heat-flow direction [81] which is, mainly, a consequence of the Lorentz force. It appears that only in Corbino devices the vanishing contribution of phonon-drag is reflected in the thermovoltage measurement.

Notwithstanding the theoretical difficulties, a simple model as the one presented here was able to reproduce the data with an excellent accuracy taking as a basis only the measured conductance. This is consistent with the experimental temperature bias estimates and the one derived from independent thermal conductivity data. The calculated figure of merit achieves large values, suggesting that the Corbino system is very promising as a low-temperature cooling device or a heat engine.

Of course, future work is needed in order to clarify the origin of the large voltage signals at the conductance minima, that is when the quantized state where G vanishes. Also, different mechanisms might be relevant in these regimes, like temperature-driven magnetic flux [83] or temperature-dependent contact potentials, which may not equilibrate in the conductance minima. Another important direction, as stated before, would be the extension of the experiment to lower temperatures which could lead to determine the entropy in fractional quantum Hall regime and non-abelian states.

CHAPTER 4

ACHIEVING OPTIMAL POWER AND FIGURE OF MERIT

The present chapter is devoted to study the transport properties of another two-dimensional topological insulator: the quantum spin Hall regime. This kind of system was already introduced in Sec. 1.2. As stated there, the most striking difference between the quantum Hall and quantum spin Hall regimes is that the latter does not need any magnetic field to be observed and in consequence, it preserves time-reversal invariance. For this reason, the quantum spin Hall regime has in each edge an even number of helical channels, the so-called Kramer's pairs [29, 31–36]. These are made of two partners with opposite spin orientation and circulating along the edge of the sample in opposite senses.

The thermoelectric properties of a two-dimensional topological insulator in the quantum spin Hall regime with an edge coupled to a magnetic domain will be studied. In order to better understand these phenomena, in Sec. 4.1 some easier examples will be presented and analyzed as reference. These are a quantum point contact (QPC) which has the transmission function given by a step function, and a quantum dot (QD) which is modeled by a resonance. The system under study will be presented in Sec. 4.2, along with the results. We will show that a system in the quantum spin Hall state with a magnetic domain, can achieve optimal power and high efficiency. Finally, conclusions are presented in Sec.4.3.

4.1 Sand Box examples; QD and QPC

To start with, in this section we review some transport properties of a quantum point contact (QPC), that has a Heaviside-Θ transmission function, as well as, a well-function, that is the sum of two QPC's and, finally, a QPC with a resonance. It will be shown that, despite the simpleness of the models, they help to understand the more complex system that will be presented in the following section.

A QPC is a narrow constriction that only lets the flow of electrons if the energy is larger than a critical value ε_0. As stated before, this can be modeled by a Heaviside- Θ transmission function,

$$\mathcal{T}_{\mathrm{QPC}}(\varepsilon) = \Theta(\varepsilon - \varepsilon_0). \tag{4.1}$$

By use of the Eqs. (2.51c) and (2.55) we can calculate the maximum power and figure of merit for this system. In Fig. 4.1 the results of the thermoelectric properties are presented. The top panel shows the maximum achievable power in units of $P_0 = (k_B \Delta T)^2/\hbar$, with k_B the Boltzmann constant and h the Planck constant and the figure of merit ZT is shown in the bottom panel. Each line corresponds to different temperatures in units of $T_0 = \varepsilon_0/k_B$.

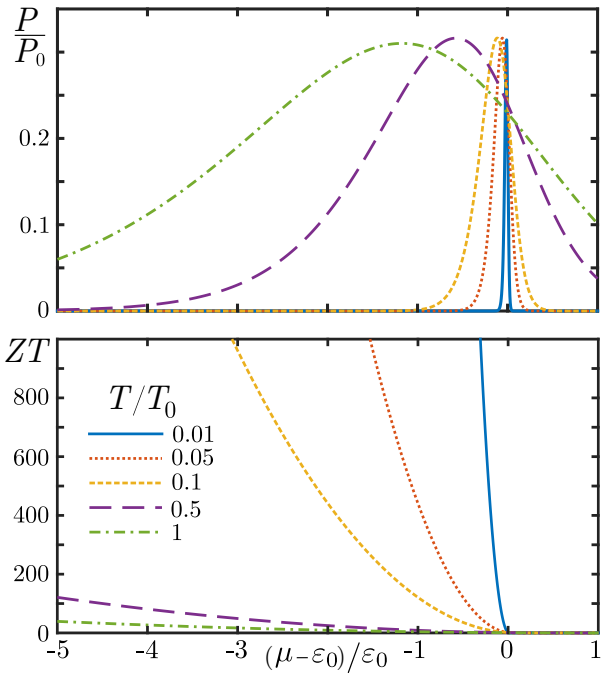

Figure 4.1: Maximum power, $P^{\max}$ in units of $P_0 = (k_B \Delta T)^2/h$ (top panel) and figure of merit ZT (bottom panel) of a transmission function corresponding to Eq.(4.1). Each line corresponds to a different temperature in units of $T_0 = \varepsilon_0/k_B$.

Note that there is no bound for the maxima value of ZT and is a decreasing function of the temperature. But it drops rapidly to zero in the region $\mu > \varepsilon$ where $\mathcal{T} = 1$. This is not the case for $P^{\max}$ that is bounded to $0.32P_0$. Also, note that this maxima is achievable at all temperatures presented here. It was already proven in Refs [103, 104] that this is the upper bound for any transmission function. In other words, there is no system with a single transport channel in which a power greater than $0.32P_0$ can be generated.

4.1.1 Well transmission function and a resonance

The second sand-box example is the sum of two QPC configured in such a way that the resulting transmission function has a well-shape function,

$$\mathscr{T}(\varepsilon) = \Theta(\varepsilon - \varepsilon_0) + \Theta(\varepsilon + \varepsilon_0). \tag{4.2}$$

For simplicity, we construct a symmetrical well that is centered around $\varepsilon = 0$. The power and figure of merit for this transmission function are presented in Fig. 4.2. The top panel indicates the maximum achievable power in units of P_0 and the bottom panel indicates the figure of merit. Each line corresponds for a different temperature in units of $T_0 = \varepsilon_0/k_B$.

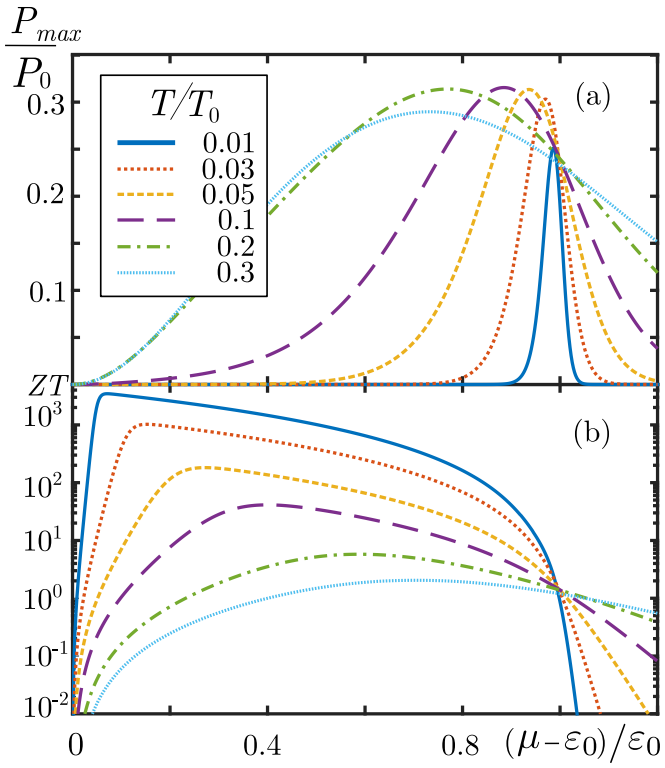

Figure 4.2: Maximum power, $P^{\max}$ in units of $P_0 = (k_B\Delta T)^2/h$ (top panel) and figure of merit ZT (bottom panel) of a transmission function corresponding to Eq.(4.2). Each line corresponds to a different temperature in units of $T_0 = \varepsilon_0/k_B$.

As in the previous situation, ZT is a decreasing function of temperatures, achieving very high values for low temperatures (note that it is presented in a logarithmic scale). But in contrast to the previous example, $P^{\max}$ is bounded in temperature, that is, there is a temperature given by the width of the well, that for higher temperatures, $P^{\max}$ decreases. In this case we identify this critical temperature $T_C \simeq 0.2T_0$.

The last sand-box example considered here is the addition of a resonance inside the well,

modeled by a Lorenztian function described by

$$\mathcal{T}(\varepsilon) = \Theta(\varepsilon - \varepsilon_0) + \Theta(\varepsilon + \varepsilon_0) + \frac{\gamma^2}{\gamma^2 + \varepsilon^2}. \tag{4.3}$$

In practice, a single resonance may be achieved in a quantum dot (QD) that acts as an energy filter letting the flow of electrons with $\varepsilon = 0$ in a window of energy given by γ.

The power and figure of merit for this system is presented in Fig. 4.3, top and bottom panels, respectively, for $\gamma = 0.001\varepsilon_0$ (left panels) and $\gamma = 0.1\varepsilon_0$ (right panels). Each line corresponds to a different temperature, using the same scale in the four panels.

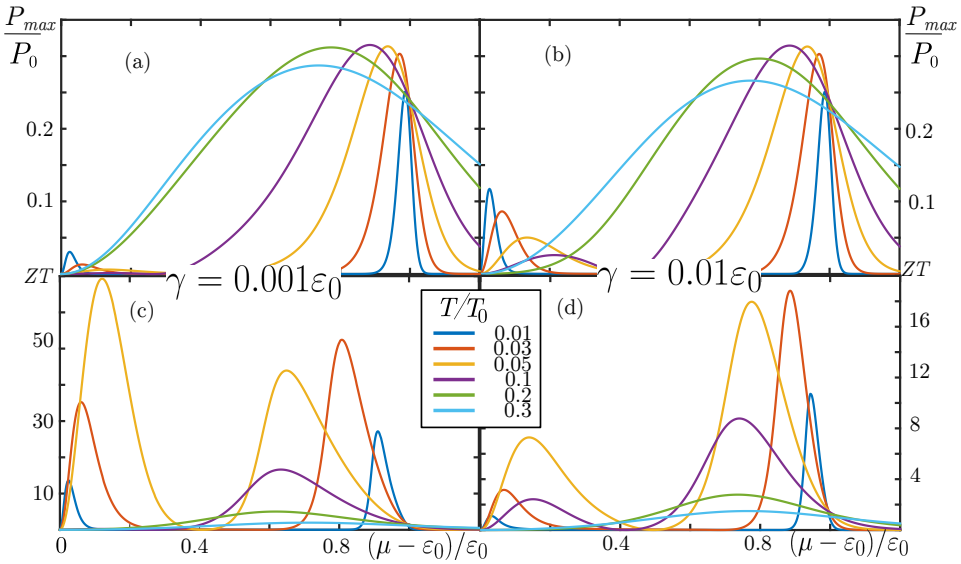

Figure 4.3: Maximum power, $P^{\max}$ in units of $P_0 = (k\Delta T)^2/h$ (top panels) and figure of merit ZT (bottom panels) of a transmission function corresponding to Eq.(4.3). Left panels correspond to $\gamma = 0.001\varepsilon_0$. Right panels correspond to $\gamma = 0.01\varepsilon_0$ Each line corresponds to a different temperature in units of $T_0 = \varepsilon_0/k$.

Note that the dominant behavior for all temperatures is similar to the one presented in Figs.4.1 and 4.2, that is, the well function is the dominant one. For low temperatures, lets say $T < \gamma k_B$, there are also features in the response due to the resonance. This maximum is situated at $\mu \sim k_B T$. In ZT there are some similarities and differences with respect to the previous examples generated by the resonance. At low temperatures, for instance $T \leq 0.05T_0$, the resonance leads to a maxima at values of chemical potential that satisfies $|\mu - \varepsilon_0| \propto k_B T$. In the low-temperature range, there are two maxima. One is situated close to $\mu - \varepsilon_0 \sim 0$ and is originated because the resonance. The other one, is situated close to $\mu - \varepsilon_0 \sim \varepsilon_0$ and is originated because of the great slope of the step function (blue line in bottom panels of Fig.4.3). As the temperature is increased, these maxima become closer to each other (yellow line in bottom panels of Fig.4.3). For higher temperatures, the window of energy given by $-\partial f/\partial\varepsilon$ envelops both, the resonance and the great slope, and as result there is only one peak in some point in the middle of the other two (purple line in bottom panels of Fig.4.3). Then, if the temperature is increased even higher, ZT decreases rapidly (green line in bottom panels of Fig.4.3).

4.2 Achieving the optimal performance

Thermal transport and thermoelectricity in the edge states of a system under the QH regime have been widely studied in a plethora of interesting works [98, 105–118], taking advantage of the chirality, the use multiterminal configurations or quantum interference can lead to manufacture heat engines or refrigerators where the efficiency is enhanced [119–121]. But all these proposals rely on QPC and QD tunnel-coupled to the edge states, which are generated by recourse to constrictions. The system analyzed in the present chapter, presented in Fig. 4.4, is a 2DTI strip in QSH regime attached to two terminals (yellowish blocks in the Fig.) which are at temperature T_1 and T_2 and at chemical potential μ_1 and μ_2. The Kramer's pair of edge state (pink and blue lines) is coupled to the one or two magnetic domains (green blocks in the Fig.). As we will discuss, these two configurations have properties alike a QD and QPC. Therefore, they can be implemented to achieve a high efficiency and figure of merit. Even more appealing is the fact that this system is in the actual state of the art of fabrication [33, 35, 36].

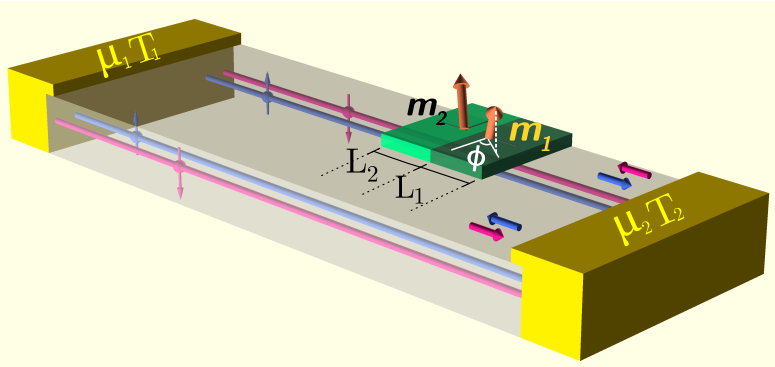

Figure 4.4: Sketch of the setup scheme. 2D TI contacted to ohmic contacts at which a bias voltage $eV = \mu_1 - \mu_2$ and temperature difference $\Delta T = T_2 - T_1$ are applied. Two nanomagnets with magnetic moments m_1 and m_2 and lengths L_1 and L_2 are contacted to a helical Kramer's pair of edge states.

4.2.1 Model and discussion

The structure sketched in Fig. 4.4 is modeled by the following Hamiltonian

$$H = \int dx \Psi^\dagger(x) \left[\left(-i\hbar v_F \frac{\partial}{\partial x} \right) \hat{\sigma}_z + J\vec{m} \cdot \hat{\vec{\sigma}} \right] \Psi(x); \tag{4.4}$$

where $\Psi(x) = \left(\psi_{R,\uparrow}(x), \psi_{L,\downarrow}(x)\right)^T$,$\hbar$ is the reduced Planck constant, v_F is the Fermi velocity, $\hat{\vec{\sigma}} = (\hat{\sigma}_x, \hat{\sigma}_y, \hat{\sigma}_z)$ are the Pauli matrices in the spin-space and J is the magnetic exchange interaction. The magnetic island is assumed to be single- or multiple-domain and it is described by the following piece-wise spacial distribution of the magnetic moment within segments of lengths $L_j = x_j - x_{j-1}$,

$$\vec{m}(x) = \sum_j \Theta(x_j - x)\Theta(x - x_{j-1})\vec{m}_j, \tag{4.5}$$

where $\vec{m}_j = \left(m_{j\perp}\cos\phi_j, m_{j\perp}\sin\phi_j, m_{j\parallel}\right)$ is the magnetic moment per unit length with components $m_{j,\perp}$ (perpendicular) and $m_{j,\parallel}$ with respect to the direction of the spin-orbit interaction of the TI.

In order to calculate the transmission function, we will proceed as in Ref. [122], starting from the evolution operator in space for the whole scattering region, which can be read as $\hat{\mathbf{U}}(x_N, x_0) = \prod_{j=1}^{N} \hat{\mathbf{U}}(x_j, x_{j-1})$ with

$$\hat{\mathbf{U}}(x_j, x_{j-1}) = \exp\left(i\frac{\varepsilon_{j\parallel}}{\hbar v_F}L_j\right)\exp\left(-i\vec{\lambda}_j.\hat{\vec{\sigma}}\right) = \exp\left(i\frac{\varepsilon_{j\parallel}}{\hbar v_F}L_j\right) = \left[\hat{\sigma}_0\cos\lambda_j - i\vec{n}_j\hat{\vec{\sigma}}\sin\lambda_j\right], \tag{4.6}$$

being $\vec{\lambda}_j = \left(i\varepsilon_{j\perp}\sin\phi, -i\varepsilon_{j\perp}\cos\phi, \varepsilon\right)L_j/\hbar v_F$ with $\varepsilon_{\perp,\parallel} = Jm_{\perp,\parallel}$ and $\vec{n}_j = \vec{\lambda}_j/\lambda_j$. The inverse of the evolution operator is the transfer matrix, which was already introduced in Sec. 2.1. Therefore, the transmission function is $\mathscr{T}(\varepsilon) = \left|\mathrm{Det}\left[\hat{\mathbf{U}}(x_N, x_0)\right]/\hat{\mathscr{U}}(x_N, x_0)_{1,1}\right|^2$.

4.2.1.1 Single-magnetic domain

For a single homogeneous domain, i.e., $N = 1$ of length L, the evolution operator of Eq. (4.6) becomes

$$\hat{\mathbf{U}}(\varepsilon) = \begin{pmatrix} \cos\lambda - i\frac{\varepsilon/\varepsilon_\perp \sin\lambda}{\sqrt{\left(\frac{\varepsilon}{\varepsilon_\perp}\right)^2 - 1}} & -i\frac{\varepsilon/\varepsilon_\perp \sin\lambda}{\sqrt{\left(\frac{\varepsilon}{\varepsilon_\perp}\right)^2 - 1}}e^{i\theta} \\ i\frac{\varepsilon/\varepsilon_\perp \sin\lambda}{\sqrt{\left(\frac{\varepsilon}{\varepsilon_\perp}\right)^2 - 1}}e^{-i\theta} & \cos\lambda + i\frac{\varepsilon/\varepsilon_\perp \sin\lambda}{\sqrt{\left(\frac{\varepsilon}{\varepsilon_\perp}\right)^2 - 1}} \end{pmatrix}, \tag{4.7}$$

and the transmission function reads

$$\mathscr{T}(\varepsilon) = \frac{|\varepsilon_\perp^2 - \varepsilon^2|}{|\varepsilon_\perp^2 - \varepsilon^2|\cos^2\lambda + \varepsilon^2\sin^2\lambda}, \tag{4.8}$$

being

$$\lambda = l\sqrt{\left(\frac{\varepsilon}{\varepsilon_\perp}\right)^2 - 1},$$

with $l = L/L_0$ and $L_0 = \hbar v_F$. Notice that the transmission function does not depend on the orientation of the magnetic island, but only on the projection $m_\perp$ perpendicular to the direction of the spin-orbit interaction of the material. Also, note that it is a symmetric function of ε around $\varepsilon = 0$. The behavior of $\mathscr{T}(\varepsilon)$ is depicted in Fig. 4.5 for different magnetic lengths ratios l. For instance, $l = 0.9$ in red line, $l = 1.5$ in purple line, $l = 3.9$ in blue line and $l = 18$ in green line.

There are some remarks to be done. First, for short islands there is a sizable tunneling amplitude through the magnetic island, while as the length of the magnet increases, the transmission function tends to a step function close to $\varepsilon \sim \varepsilon_\perp$. When $\varepsilon = \varepsilon_\perp$, the transmission function behaves as $\mathscr{T} = (1 + l^2)^{-1}$ and its slope at that point behaves as $\mathscr{T}' = 2l^4[1 + l^2]/3[1 + l^2]^3$, which saturates at the value 2/3. Also, note that for energies $\varepsilon > \varepsilon_\perp$ the transmission function presents oscillations; the larger the island is, the more oscillations appear. The maxima, at energies ε_n saturate to 1 and the minima are given by $\mathscr{T}^{\min}(\varepsilon_m) = 1 - (\varepsilon_\perp/\varepsilon_m)^2$, for energies satisfying

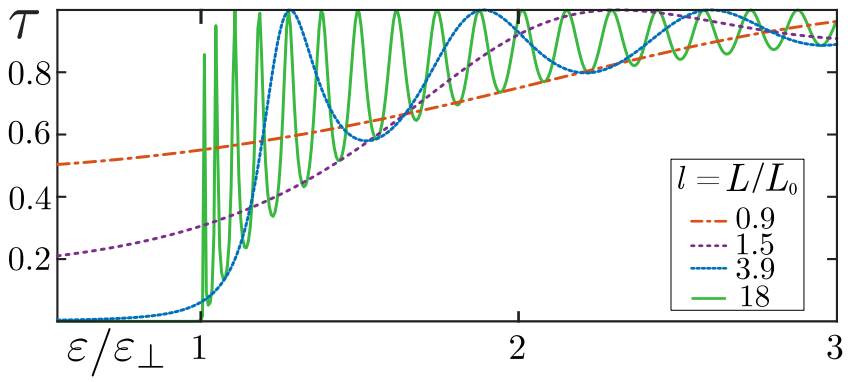

Figure 4.5: Transmission function $\mathscr{T}(\varepsilon)$ for a single homogeneous magnetic domain. Different colors represent different magnetic lengths; $l = 0.9$(red), $l = 1.5$(purple),$l = 3.9$(blue), $l = 18$(green).

$\left(\varepsilon_{n(m)}\right)^2 = (\varepsilon_\perp)^2 + \left(\pi\alpha_{n(m)}\hbar v_F/L\right)^2$, with $\alpha_{n(m)}$ being an integer number for the maxima and a half-integer number for the minima.

As anticipated at the beginning of this section, the transport response corresponding to this transmission function is similar to one described by a Heaviside-Θ function, alike a QPC if the temperature is high enough. Instead, in the low-temperature regime, the response is dominated by the peaks and resembles the response of a QD. The impact of these features is presented in Fig. 4.6, where it is shown the maximum achievable power (top panels) in units of $P_0 = (k_B\Delta T)^2/h$ and the figure of merit, ZT (bottom panels). Left panels are for $L = 10$ and right panels are for $L = 20$. Each color represents a different temperature T in units of $T_0 = \varepsilon_\perp/k$.

For the shortest length shown in panels (a) and (b), $l = 10$, $\mathscr{T}(\varepsilon_\perp) < 0.01$ and $d\mathscr{T}/d\varepsilon|_{\varepsilon_\perp} \sim 0.65$, i.e., close to the maximal slope (2/3), implying a pronounced step in the transmission function at the closing of the energy gap. The plots shown in panels (c) and (d) correspond to a longer island of length $L = 20$, for which the step function is slightly more pronounced. For very low temperatures, within a scale k_BT smaller than the width of the peaks of $\mathscr{T}(\varepsilon)$, both $P_{\max}$ and ZT vanish for $\mu = \varepsilon_n$ (see arrows in panels (a) and (b)). At sufficiently high temperature, such that several maxima of $\mathscr{T}(\varepsilon)$ are included in an energy window of width k_BT defined by the derivative of the Fermi-Dirac function, the behavior is dominated by the average between the envelopes for the minima and the maxima of $\mathscr{T}(\varepsilon)$. The resulting function is approximately a smoothed step-function, regardless of the length of the island. For this reason, $P_{\max}$ shows a wide maximum centered at $\sim |\varepsilon_\perp - \mu| \sim k_BT$ [120, 123]. The maximum is as high as $\sim 0.244P_0$, i.e., $\sim 75\%$ of the bound $0.32P_0$. The operation of this system as a cooling device operating beyond linear response was later reported in Ref.[117]. An excellent performance was found as well in that case.

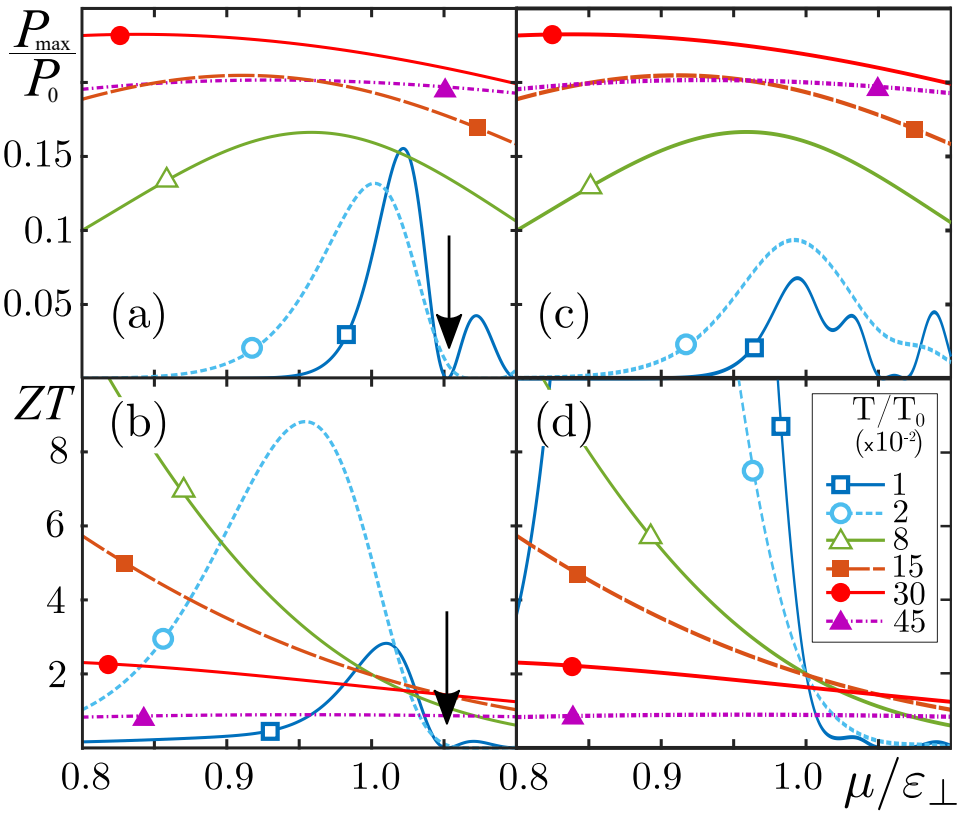

Figure 4.6: Maximum power (upper panels) and figure of merit ZT (lower panels), for a single magnetic domain of $L = 10$ (a)-(b) and $L = 20$ (c)-(d). Each line corresponds to different temperatures. The maximum values in (a) and (b) are $P_{\max}(T/T_0 = 0.3) = 0.240P_0$ (a), $ZT(T = 0.08) = 60$ (b), $P_{\max}(T/T_0 = 0.3) = 0.244P_0$ (c), and $ZT(T/T_0 = 0.02) = 274$ (d), with $T_0 = \varepsilon_\perp/k$. Power is expressed in units of $P_0 = (k\Delta T)^2/h$.

4.2.1.2 Two magnetic domains: appearance of a resonance in the gap

In this last subsection, the results concerning to the situation with two magnetic domains with $L_1 = L_2 = l$, $\phi_1 = 0$, $\phi_2 = \phi$, and $\varepsilon_{\perp,1} = \varepsilon_{\perp,2} = \varepsilon_\perp$ will be presented. The resulting transmission function reads,

$$\mathcal{T}(\varepsilon) = \left\{ \left[\cos^2\lambda + \frac{\sin^2\lambda}{r^2}\left(\cos\phi - \frac{\varepsilon^2}{\varepsilon_\perp^2}\right)\right]^2 + \left[-\frac{\varepsilon}{\varepsilon_\perp}\frac{\sin 2\lambda}{r} + \sin\phi\frac{\sin^2\lambda}{r^2}\right]^2 \right\}^{-1}. \tag{4.9}$$

The behavior of the transmission function for two domains is illustrated in Fig. 4.7, for a set of orientations of the magnetization. The upper and lower panels show the transmission function for $l = 10$ and $l = 4$, for each domain, respectively.

The new feature in the present case, in comparison to the case of a single magnetic moment, is the existence of resonances within the gap, $|\varepsilon| < \varepsilon_\perp$, for $\phi \neq 0$. Note, that the width of the resonance decreases for increasing l. The position of the resonant state depends on the phase difference ϕ. For $\phi = \pi$, Eq. (4.4) coincides in that case with the model introduced by Jackiw and Rebbi (JR) [124–126], which has a topological zero mode localized at the domain wall.

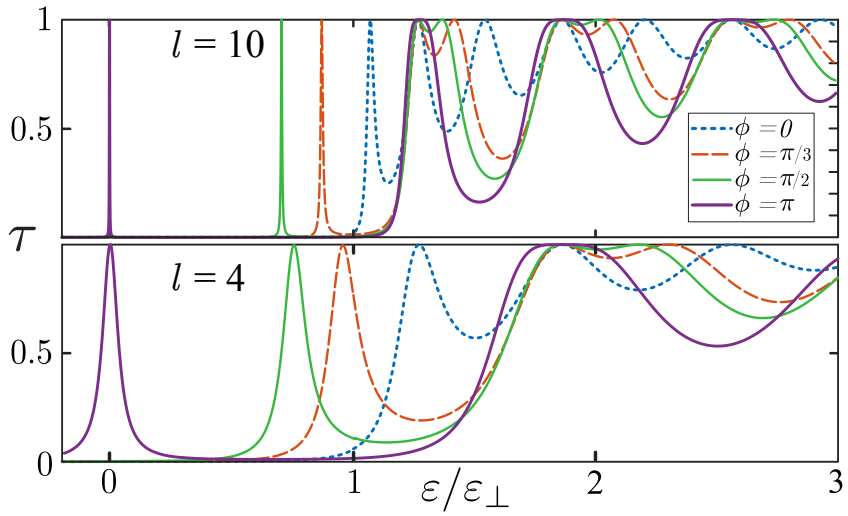

Figure 4.7: Transmission function $\mathcal{T}(\varepsilon)$ defined in Eq. (4.9) for two magnetic domains of equal size ($l = 4, 10$) with the perpendicular component of the magnetic moments oriented with a relative tilt ϕ.

Notice that for $\varepsilon = 0$, Eq. 4.9 reads

$$\begin{aligned}\left[\mathcal{T}(0,l,\phi)\right]^{-1} &= \left[\cos^2(li) + \left(\frac{\sin(li)}{i}\right)^2 \cos\phi\right]^2 + \left(\sin\phi\left(\frac{\sin li}{i}\right)^2\right)^2 \\ &= \left(\cosh^2 l + \sinh^2 l\cos\phi\right)^2 + \sin^2\phi\sinh^2 l \\ &= \left(1 + \left(1+\cos\phi\right)\sinh^2 l\right)^2 + \sin^2\phi\sinh^2 l, \end{aligned} \tag{4.10}$$

where $\mathcal{T}(0,l,\phi) \sim 0$ for $l > 1$ except for $\phi = (2n+1)\pi$, with n integer, in which case $\mathcal{T}(0,l,(2n+1)\pi) = 1$. Therefore, it can be concluded that for $\phi = (2n+1)\pi$, there is resonant state in the center of the gap, with energy $\varepsilon = 0$. The width of this resonant state depends on the length as e^{-l}, which means that, the width of the resonance decreases with l. For this configuration there is also a simple expression for the minima of the oscillations above the gap. It reads

$$\mathcal{T}^{min}(\varepsilon_m) = \left[\left(\varepsilon_m^2 - \varepsilon_\perp^2\right)/\left(\varepsilon_m^2 + \varepsilon_\perp^2\right)\right]^2, \tag{4.11}$$

where $(\varepsilon_m)^2 = (\varepsilon_\perp)^2 + (\pi\alpha_m\hbar v_F/L)^2$, with α_m being a half-integer number. It can be used the following criterion to determine the critical length l_c for which the width of the resonant state is smaller than the energy gap, $\mathcal{T}(\varepsilon/\varepsilon_\perp = 0.5) \leq 0.5$, leading to

$$\mathcal{T}\left(\frac{\varepsilon}{\varepsilon_\perp} = 0.5, l_c\right) = \frac{9/8}{\frac{15}{8} - \cosh\left(\sqrt{3}l_c\right) + \frac{1}{4}\cosh\left(2\sqrt{3}l_c\right)}, \tag{4.12}$$

resulting in $l_c \simeq 0.9$. Hence, a resonance is identified in the configuration $\phi = \pi$ for $l > l_c$.

The previous analysis was based on the assumption that the two domains have the same length. To conclude the analysis of the transmission function, results will be presented for the case where the lengths of the domains are not the same, or they have different orientations. A

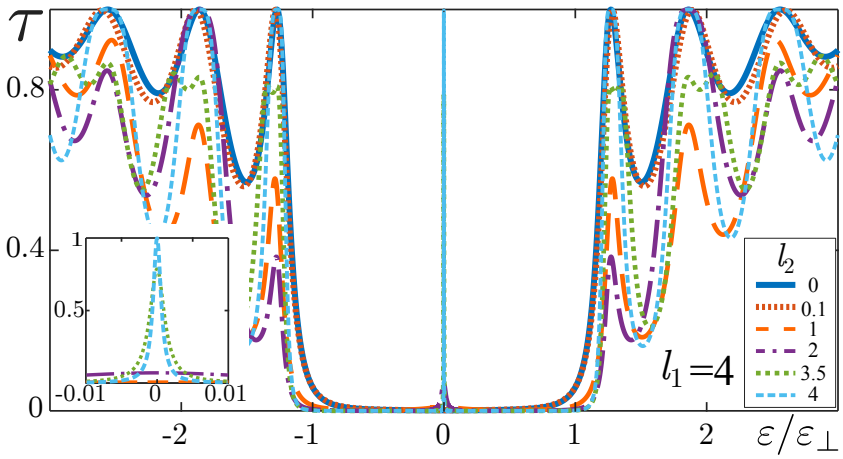

Figure 4.8: Transmission function for a two-domain configuration with $\phi = \pi$. The first island has a fixed length,$l_1 = 4$ while the length of the second island is changed represented in different colors. The inset shows a detail of the bound state at zero energy

situation where the first domain has $l_1 > 1$ and the second domain has $l_2 \leq l_1$ will be considered. The generalization of Eq. (4.9) reads

$$\left[\mathcal{T}(\lambda_1,\lambda_2,\phi,x)\right]^{-1} = \left[\cos\lambda_1\cos\lambda_2 + \frac{\sin\lambda_1\sin\lambda_2}{r^2}\left(\cos\phi - x^2\right)\right]^2 + \\ + \left[\sin\phi\frac{\sin\lambda_1\sin\lambda_2}{r^2} - \sin(\lambda_1+\lambda_2)\frac{x}{r}\right]^2. \tag{4.13}$$

For $\phi = \pi$, the height of the resonant level is given by

$$\mathcal{T}(\lambda_1,\lambda_2,\phi=\pi,x=0) = \frac{1}{\cosh(l_1 - l_2)}. \tag{4.14}$$

For the particular situation where $l_1 = l_2$ the previous result $\mathcal{T} = 1$, is recovered and when $l_2 \ll l_1$ the transmission function becomes vanishing small . From Eq. (4.14) we can calculate that if $|l_1 - l_2| \leq 0.5$, then $\mathcal{T}$ hosts a resonance with $\tau(0) > 0.9$. The behavior of $\tau(\varepsilon)$ for $l_1 \neq l_2$ is illustrated in Fig. 4.8 for $l_1 = 4$ and $l_2 < l_1$. Note that for $l_1 - l_2 > 2$, the resonance is no longer distinguished within the gap. However, for small difference in the lengths of the two magnetic domains, not only there is a resonant peak, but also the behavior of $\tau(\varepsilon)$ above the gap is practically unaffected.

Another property of the transmission function is the robustness against different orientations in the magnetic moment. In order to study this effect, each magnetic domain was divided in n pieces of equal length and each phase has a random component. Hence, the orientation of the magnetic moment within each of these pieces is $\phi_j = \phi^0 + \delta\phi_j$, $j = 1,\ldots,n$, where $\delta\phi_j$ is a random component of the phase within the $j-$th sub-domain, while $\phi^0 = 0,\pi$ for the first and second domain, respectively. According to the previous analysis, the partitions must satisfy $l/n << 1$, in order to be considered as a perturbation over the main magnetic configuration of the domain. In fact, for $l/n \sim 1$, each of these partitions would separately open a gap and would behave as an additional magnetic domain.

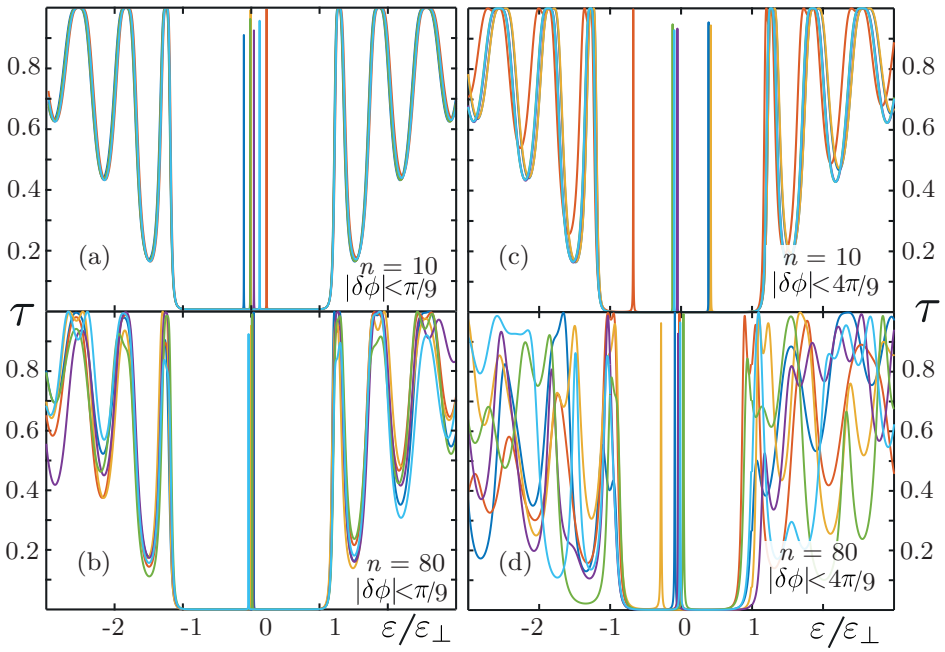

Figure 4.9: Transmission function for two domains of equal length $l = 4$. Panels (a) and (b) have an orientation of the magnetic moments $\phi^0 = 0, \pi$ and random piece-wise random fluctuations $\delta\phi_j = \pm\pi/9$, $j = 1, \ldots, n$, within $n = 10$ partitions of equal length (a) and $n = 80$ (b). Panels (c) and (d) correspond to random fluctuations $\delta\phi_j = \pm 4\pi/9$, $j = 1, \ldots, n$, within $n = 10$ partitions of equal length (c) and $n = 80$. Different colors correspond to different realizations of disorder.

Examples are shown in Figs. 4.9 for weak ($\delta\phi \leq \pi/9$) and strong ($\delta\phi \leq 4\pi/9$) amplitude in the random component of the magnetic moment, respectively. In each case, we compare the behavior of different numbers of partitions n. In the case of weak disorder, shown in panels (a) and (b), the behavior of the transmission function above the gap is almost unaffected by the inhomogeneous orientation of the magnetic moment, while the position of the resonant peak is slightly shifted away from $\varepsilon = 0$. Albeit, the width of the latter remains unaffected. The shift becomes smaller as the number of partitions increases, as seen in the comparison between the top and the bottom panels. The case of strong fluctuations is analyzed in panels (c) and (d). The behavior of the resonance is similar to the case of weak disorder. For increasing fluctuations of the magnetic moment, the shift of the resonance away from $\varepsilon = 0$ is larger. For small number of partitions n (top panel) the pattern of maxima and minima above the gap becomes also affected. However, the overall structure of $\mathcal{T}$, including the existence of a resonant peak, the clear opening of the gap and a series of peaks with an envelope defined by a Heaviside function are preserved. For larger number of partitions (bottom panel), all the features, including the resonant peak, as well as the pattern of maxima and minima above the gap are mildly affected.

This analysis leads us to conclude that the performance of the setup is very robust under weak fluctuations in the orientation of the magnetic moment, as well as under fluctuations in the length of the two domains. This stability is a consequence that the system realizes a Goldstone-Wilczec

soliton, discussed in Refs. [127–129].

Having analyzed the features of the transmission function, its thermoelectrics response will be discussed, focusing only on the special case of $\phi = \pi$ presented in Fig. 4.10.

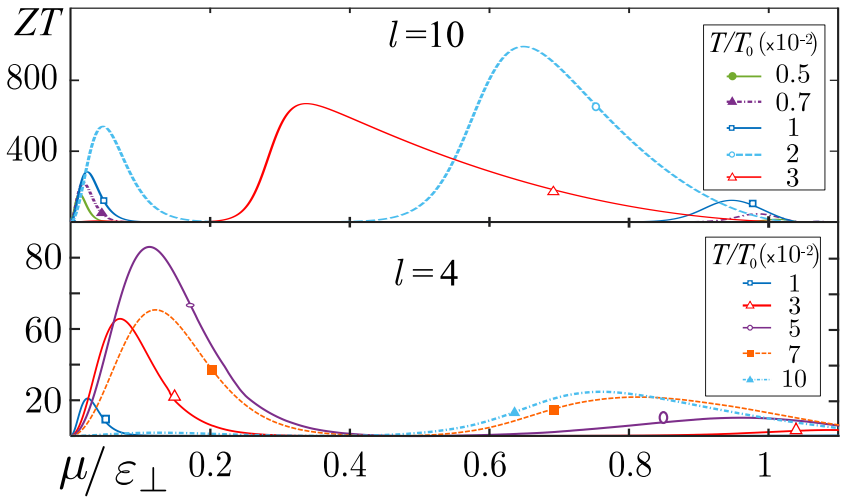

Figure 4.10: Figure of merit ZT for two magnetic domains of length $l = 4, 10$ each, with the perpendicular component of the magnetic moments tilted in $\phi = \pi$. Other details are similar to previous figures.

For $\mu \sim k_B T$ the thermoelectric response is dominated by the resonance within the gap. This leads to high values of ZT for $k_B T \lessapprox 10\gamma$, being γ the width of the resonance, which depends on the domain length. For higher temperatures, the transport behavior is dominated by the Heaviside-step function and well-shaped envelopes of the transmission function. Hence, the thermoelectric response is similar to the one discussed for a single domain.

A comparison between two configurations, recall one and two magnetic domains, is presented in Fig. 4.11 where the top panel presents the maximum achievable power $\overline{P}_{\max} = \mathrm{Max}_\mu[P_{\max}]$ for a given temperature and the bottom panel the maximum figure of merit, $\overline{ZT} = \mathrm{Max}_\mu[ZT]$, achievable for a given temperature. Yellow and purple lines are for one magnetic domain of length $l = 10$ and $l = 20$ respectively while red and blue lines are for two magnetic domain with each domain having a length $l = 10$ and $l = 20$ respectively.

The boundary for the lowest-temperature regime is identified with the range of T below the one corresponding to the minimum of $[P_{\max}]$. This regime is akin to the response due to a Lorenzian-type transmission function and is non-universal, since it depends on the details of the resonant peaks of $\mathcal{T}(\varepsilon)$, like its width and position if the situation where $\phi \neq \pi$. In the case of two domains with $\phi = \pi$, it is possible to distinguish a narrow feature, which is associated to a resonance within the gap, followed by a second feature, associated to the the first peak after the closing of the gap. For islands with a single domain, we can distinguish only one feature, which is associated to the first peak after the closing of the gap. For larger temperatures, we enter the regime dominated by the Heaviside-Θ alike function corresponding to averaging the envelopes of the minima and maxima of the transmission function for $\varepsilon > \varepsilon_\perp$. While the maxima corresponds

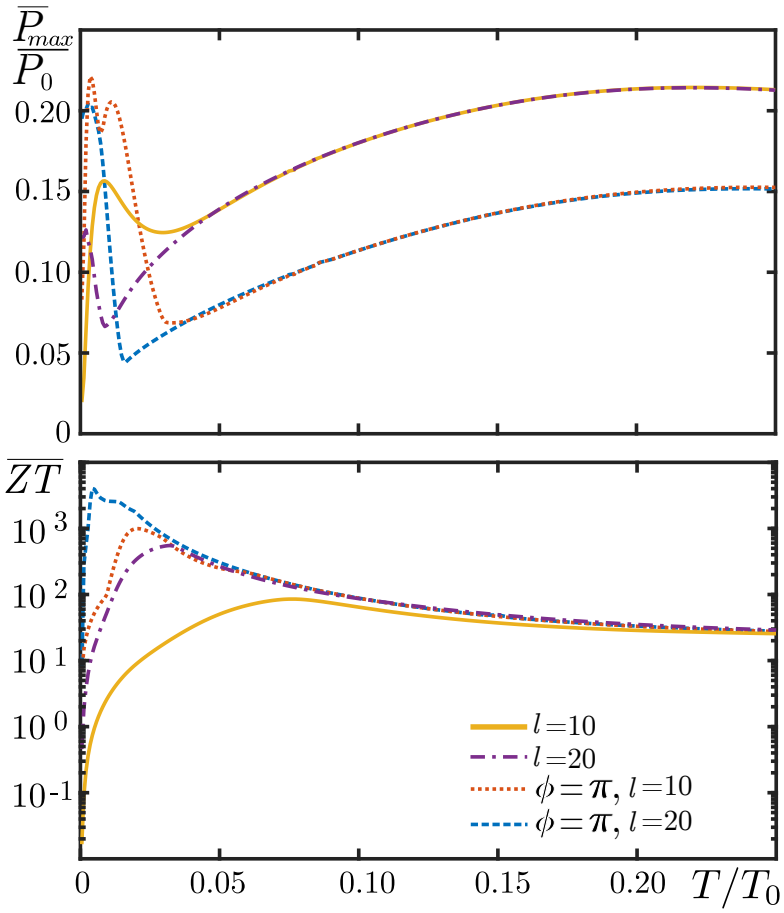

Figure 4.11: $\overline{ZT} = \mathrm{Max}_\mu[ZT]$ and $\overline{P}_{\mathrm{max}} = \mathrm{Max}_\mu[P_{\mathrm{max}}]$, corresponding to the maximum values of P_{max} and ZT over the whole range of μ, as functions of the temperature T. AF denotes islands with two domains anti-parallel aligned.

to $\mathscr{T} = 1$, the minima are deeper for two domains with $\phi = \pi$ than for a single domain. Hence, the values of $\mathrm{Max}_\mu[P_{\mathrm{max}}]$ within this regime are higher for a single domain than for two anti-parallel ones. For both orientations, the behavior is universal, namely, it does not depend on the length of the island. The figure 4.11 shows the onset of the third (high-temperature) regime, where the well-shape becomes dominant and $\mathrm{Max}_\mu[P_{\mathrm{max}}]$ turns to be a decreasing function of T.

4.3 Conclusions of this chapter

In this chapter, the transmission function characterizing the coherent transport of electrons in a structure consistent of a pair of a helical edge states in a two-dimensional topological insulator coupled by a magnetic island with a magnetic moment having a component perpendicular to the direction of the spin orbit of the topological insulator was analyzed. It was shown that this setup has the necessary conditions to achieve high thermoelectric performance. This is a consequence of the opening of a gap in the spectrum of the helical edge states with a step-like slope of the

transmission function at the opening of the propagating modes in the spectrum. Depending on the energy range and the configuration of the magnetic domains, the transmission function has features similar to a Heaviside-Θ function, as well as features similar to a Lorentzian function, close to the Dirac-δ function, which are known to be optimal for high power production and figure of merit, respectively. With two magnetic domains, the Jackiw-Rebbi resonant states in the gap make possible very large values of the figure of merit, $ZT > 100$. These are attained for the heat-engine and refrigeration modes. The calculations were focused on a single pair of edge states, but the currents simply scale in a factor two when the pair at the opposite edge is also considered. The range of temperature operation is set by the magnetic gap $\varepsilon_\perp$. For a single domain generating an effective magnetic field of 1.8 T to 4 T [130], we estimate $\varepsilon_\perp \sim 1\times10^{-4}$ eV to 2×10^{-4} eV, corresponding to a reference temperatures $T_0 \sim 1.2$ K to 2.4 K. According to the present study, such a device with a length of the magnetic island of $\sim 10L_0$, being $L_0 = \varepsilon_\perp/\hbar v_F$, operates as a heat engine at a high performance ($\sim 75\%$ of the optimal bound) regarding power generation with a figure of merit $ZT \gg 1$ for $T < 0.5T_0$. Taking estimates for the Fermi velocity of the helical edge states in quantum-wells of HgTe from Ref. [33], we have $\hbar v_F \sim 0.9\,\mathrm{eV\,nm^{-1}}$, leading to $L_0 \sim 10\,\mu$m to 20 μm. These parameters are at the state of the art of present experimental realizations.

CHAPTER 5

ADDING SUPERCONDUCTIVITY: AN HYBRID JUNCTION WITH QSH

In this chapter a hybrid junction consisting of a pair of semi-infinite superconducting leads will be studied, where in the middle there is a two-dimensional topological insulator in the quantum spin Hall state with a nanomagnet within it. In other words, the configuration is similar to the one presented in chapter 4 but with superconducting leads. The system is depicted in Fig. 5.1, where the superconducting leads are represented by red and blue blocks having only a temperature bias $\delta T > 0$. This kind of structures have received great attention in the last time [131–136]. One prominent example is the platform proposed by Fu and Kane [137], where they propose a Josephson-junction made out of a Kramer's pair in proximity to a s-wave superconductor and a magnet embedded in the junction. For a magnetic moment having a component perpendicular to the natural quantization axis of the 2D-topological insulator, Majorana bound states are formed. The concomitant signatures in the behavior of the Josephson current have been investigated in several works [137–150].

The role of the magnetic island coupled to the Kramers' pair of the two-dimensional topological insulator is to introduce a boundary with a backscattering process in the Dirac system constituted by the edge states. Some of the properties were already shown in chapter 4 (and also in references therein). Recall that in the previous chapter a configuration with several magnetic domains was also studied where it was shown a realization of the Jackiw-Rebbi(JR) model of a Dirac system with a space-dependent soliton mass [124–126]. Jackiw-Rebbi physics in presence of a superconductor was already studied in Refs. [151, 152] and in Refs. [153–155] fractional charges in two-dimensional topological insulator with many-body interactions were presented.

Here, the Andreev spectrum and the thermal conductance of the system for the same configurations as the previous chapter, one and two magnetic domains will be analyzed. It will be shown that the thermal conductance turns out to be very sensitive to the presence of Jackiw-Rebbi

resonance, unlike the Josephson current, and the present procedure can be used as smoking gun to reveal the topological nature of a system. Unlike the previous chapters, there is no thermoelectric response in this device, since the superconductor imposes particle-hole-symmetry and it is necessary to have it broken in order to get thermoelectricity.

This chapter is organized as follows; in Sec. 5.1 the model and the calculations to get the scattering matrix of the system using the framework developed in Sec. 2.1 are presented. The calculation of the Andreev bound states (ABS) for each configuration is presented in Sec. 5.2. In Sec. 5.3 the analysis of the transmission function calculated via the **P**-matrix alongside with the thermal conductance for each domain are presented. Finally, the conclusions of this chapter are presented in Sec. 5.4.

5.1 Model and general framework

The studied system is presented in Fig. 5.1. As stated before, it consists of a 2DTI attached by the bottom to two superconducting semi-infinite electrodes that are kept at a phase difference ϕ and at different temperatures, T for the blue block at right and $T+\delta T$ for the red block at left (with $\delta T > 0$). These superconductors, due to proximity effect, induce a pairing potential in the portion of the 2DTI beneath them. Also, above the TI there are two magnetic domains (sketched with the yellow blocks) with lengths L_1 and L_2 and are placed at distance l_S of the electrode (eventually this parameter will be set to zero). Each domain has a magnetization $\vec{m}_1$ and $\vec{m}_2$ respectively, in the plane of the sample and a relative orientation θ. Also, they may have different length and different magnetization. Both domains are put in contact with the same edge state (sketched with solid lines in the grey area) of the sample that is considered to be wide enough so that both edges are uncoupled and only one Kramer's pair can be considered .

The Hamiltonian describing the system, taking into account the proximity-induced pairing potential and the coupling to the magnetic island, expressed in the basis of Nambu spinors $\Psi(x) = \left(\psi_\uparrow(x), \psi_\downarrow(x), \psi_\downarrow^\dagger(x), -\psi_\uparrow^\dagger(x)\right)^T$, reads

$$H = \int_{-\infty}^{+\infty} dx \Psi^\dagger(x)[\mathscr{H}_0(x) + \mathscr{H}_M(x) + \mathscr{H}_S(x)]\Psi(x), \tag{5.1}$$

where each term is

$$\mathscr{H}_0(x) = \left(-i\hbar v_F \frac{\partial}{\partial x}\right)\sigma_z\tau_z - \mu\sigma_0\tau_z, \tag{5.2a}$$

$$\mathscr{H}_M(x) = J\vec{m}(x)\cdot\vec{\sigma}, \tag{5.2b}$$

$$\mathscr{H}_S = \vec{\Delta}(x)\cdot\vec{\tau}. \tag{5.2c}$$

The first term of Eq. (5.2a), describes the free Kramers pair, with $\check{z}$ as the natural quantization axis of the topological insulator. The terms of Eqs. (5.2b) and (5.2c) describe, respectively, the effect of the coupling to the magnetic island and the BCS superconducting pairing potential. The

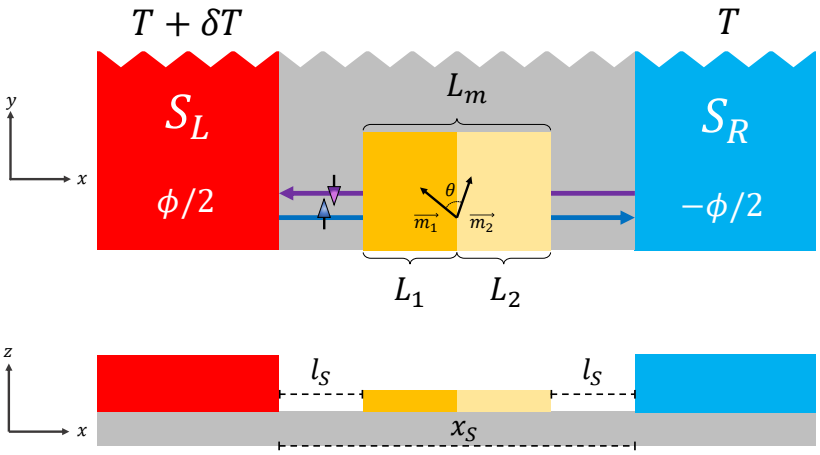

Figure 5.1: Top and lateral view of the device. Two semi infinite superconductors at temperatures T for the right and $T+\delta T$ for the left with $\delta T > 0$ and with a phase bias ϕ, proximized to a 2DTI in the quantum spin Hall regime. A magnetic island, of total length L_m composed with two magnetic domains of length L_1 and L_2 respectively, is placed at distance l_S from both superconductors, and contacted to the Kramer's pair of helical states localized at one of the edges. The magnetic moments of the two domains are oriented with a relative tilt θ.

matrices $\sigma_0, \vec{\sigma} = (\sigma_x, \sigma_y, \sigma_z)$ and $\tau_0, \vec{\tau} = (\tau_x, \tau_y, \tau_z)$ are the usual Pauli matrices that operate, on the spin and particle-hole degrees of freedom, respectively. Note that $H_0 + H_M$ is the Hamiltonian already presented in Sec. 4.2. The pairing potential induced by superconducting proximity is described by,

$$\vec{\Delta}(x) = \left[\vec{\Delta}(\phi/2)\Theta(-x) + \vec{\Delta}(-\phi/2)\Theta(x - x_S)\right], \tag{5.3}$$

with $\vec{\Delta}(\pm\phi/2) = \Delta_0\left(\cos\phi/2, \pm\sin\phi/2, 0\right)$ where ϕ is the phase bias and x_S is the distance between the two superconductors. The magnetization of the island is accounted for

$$\vec{m}(x) = \vec{m}_1[\Theta(x - l_S) - \Theta(x - x_1)] + \vec{m}_2[\Theta(x - x_1) - \Theta(x - x_2)], \tag{5.4}$$

where $\vec{m}_j = m_j\left(\cos\theta_j, \sin\theta_j, 0\right)$, for $j = 1, 2$ and $x_1 = L_1 + l_S$ and $x_2 = L_2 + x_1$. The total length of the magnetic island is $L_m = L_1 + L_2$.

For simplicity, we assume a fully anisotropic magnetic moment with a vanishing $\check{z}$ component of the magnetization, that is, the direction parallel to the natural quantization axis of the topological insulator. Recall that, as in the situation with a single magnetic domain presented in Ch. 4, the component of the magnetization perpendicular to $\check{z}$ is the only mechanism introducing a backscattering processes in the present problem, and it is due to this, that it generates non-trivial effects in the two-terminal transport properties. For instance the Dirac-mass term that opens a gap in the spectrum. If this mass is not uniform in space, a long enough magnetic domain may suppress the tunneling for the propagating helical edge states. In order for this to happen, the magnetic domain must be larger than the characteristic length defined by

$$\xi_M = \frac{\hbar v_F}{Jm}, \tag{5.5}$$

being Jm the magnetic energy gap in the limit of uniform magnetization along infinite-length helical modes. To sum up, the inequality $L_m > \xi_M$ must be satisfied in order to show a clear suppression of the transmission probability due to the opening of the magnetic gap. Another interesting effect introduced by a non-uniform magnetization takes place in the case of two magnetic domains with exactly opposite orientations, i.e., $\theta = \pi$, which realizes the JR model [124–126], where two consecutive masses with different sign define a soliton domain wall in a one-dimensional Dirac system. This model, along with its Su-Schrieffer-Heeger discrete version [156] hosts a topological zero mode at the interface. The stability and robustness of this mode was already analyzed and explained in Ch. 4.

In combination with superconductivity, for a finite magnetization embedded in the junction between the two superconductors, a topological state develops, with Majorana zero modes (MZM) localized at the boundaries between the superconductors and the magnetic island [137, 138, 144]. Interestingly, a magneto-Josephson duality exists [138], such that the role of the magnetization can be interchanged with the superconducting potential. This can be understood by noticing that in the Hamiltonian for the device, Eqs.(5.2b) and (5.2c), the terms with the Pauli matrices acting on the spin degrees of freedom, $\vec{\sigma}$, have the same structure as those with Pauli matrices $\vec{\tau}$, which act on the particle-hole degrees of freedom. Due to the s-wave nature of the superconducting order parameter, the relevant physical parameter characterizing the orientation of the magnetic moments is the relative tilt θ. Furthermore, this angle is related through the above mentioned duality to the phase difference ϕ between the two superconductors.

Importantly, in the presence of the superconducting contacts, the other characteristic length in the problem is the superconducting coherence length $\xi_S = \hbar v_F/\Delta$. As it will be discussed, most of the interesting effects in the behavior of the thermal conductance arise from the interplay between the magnetic and superconducting spectral gaps. The conditions under which they are most remarkable correspond to comparable values for the two characteristic lengths ξ_M and ξ_S. Finally, it was sometimes convenient to characterize the strength of the magnetic coupling with respect the proximized superconducting gap Δ_0 through the dimensionless parameter

$$\Gamma = \frac{Jm}{\Delta_0} = \frac{\xi_S}{\xi_M}. \tag{5.6}$$

It is worth to notice that this parameter also defines the ratio between the magnetic and superconducting lengths.

5.1.1 Theoretical approach

The general framework to calculate the transport properties, is the scattering matrix as introduced in Sec.2.1. In particular in Sec. 2.1.1 the example of the scattering matrix of a NS interface with the superconducting edge at the right of the system was discussed. To be able to have the scattering matrix of the full system, i.e., superconductor at left, topological insulator, magnetic domains, topological insulator, superconductor at right, the scattering matrix for the left interface

is needed, in combination with the scattering matrix for the right junction and for the magnetic domain. After that, the rule to compose scattering matrices, explained in Sec.2.1, is applied. The notation $\mathbf{S}_L$ indicates the scattering matrix for the left interface of Fig. 5.1; $\mathbf{S}_M$ for the central part, where there are as many magnetic domains as needed and $\mathbf{S}_R$ for the right interface. Recall that the scattering matrix for a NS junction is written as

$$\begin{pmatrix} b_R^- \\ c_R^- \\ \tilde{b}_R^+ \\ \tilde{c}_R^+ \end{pmatrix} = \begin{pmatrix} 0 & r^R_{e,h} & t^R_{e,\tilde{e}} & 0 \\ r^R_{h,e} & 0 & 0 & t^R_{h,\tilde{h}} \\ t^R_{\tilde{e},e} & 0 & 0 & r^R_{\tilde{e},\tilde{h}} \\ 0 & t^R_{\tilde{h},h} & r^R_{\tilde{h},\tilde{e}} & 0 \end{pmatrix} \begin{pmatrix} b_R^+ \\ c_R^+ \\ \tilde{b}_R^- \\ \tilde{c}_R^- \end{pmatrix}, \tag{5.7}$$

where it was introduced the notation $c_R^{\pm}/b_R^{\pm}$ for the incoming and out going quasi-particles/quasi-holes (QPs/QHs) from the TI region and with $\tilde{c}_R^{\mp}/\tilde{b}_R^{\mp}$ for the incoming and outgoing QPs/QHs from the superconductor side. The label R indicates the interface, with the right superconductor and its direction of propagation is along the $\check{x}$ direction is indicated with the sign $\pm$ (+ for right movers and − for the left movers). The coefficients can be compactly written as

$$r^R_{\gamma,\bar{\gamma}} = \gamma \frac{V}{U} e^{i\alpha} e^{i\frac{\phi}{2}}, \tag{5.8a}$$

$$r^R_{\tilde{\gamma},\tilde{\bar{\gamma}}} = -\frac{V}{U} e^{-i\beta} \Theta(\varepsilon - \Delta), \tag{5.8b}$$

$$t^L_{\gamma,\tilde{\gamma}} = \frac{\sqrt{U^2 - V^2}}{U} e^{\frac{i}{2}(\alpha-\beta)} e^{-i\gamma\frac{\phi}{4}} \Theta(\varepsilon - \Delta), \tag{5.8c}$$

$$t^R_{\tilde{\gamma},\gamma} = \bar{\gamma} \frac{\sqrt{U^2 - V^2}}{U} e^{\frac{i}{2}(\alpha-\beta)} e^{i\bar{\gamma}\frac{\phi}{4}} \Theta(\varepsilon - \Delta), \tag{5.8d}$$

where the QP/QH index ($\gamma = e, h$) in the LHS is converted in a simple sign ($\gamma = +, -$) in the RHS and the bar represents the opposite element (for instance, $\bar{e} = h$). Note that unlike the situation presented in Sec. 2.1.1 the superconducting phase ϕ has to be taken into account. Recall that the functions U and V were defined as

$$U = \sqrt{\frac{\Delta}{2\varepsilon}}\, e^{\frac{1}{2}\arccos\frac{\varepsilon}{\Delta}}; \tag{5.9a}$$

$$V = \sqrt{\frac{\Delta}{2\varepsilon}}\, e^{-\frac{1}{2}\arccos\frac{\varepsilon}{\Delta}}, \tag{5.9b}$$

and the phases $\alpha = 2\frac{\varepsilon}{\Delta}\frac{l_S}{\xi_S}$, $\beta = 2\frac{l_S}{\xi_S}\sqrt{\left(\frac{\varepsilon}{\Delta}\right)^2 - 1}$, with $\xi_S = \hbar v_F/\Delta$ the coherence length, Δ is the superconducting gap and l_S the length of the 2DTI measured from the superconductor as depicted in Fig. 5.1. A similar result for the scattering matrix S_L at the left interface is obtained by replacing $\left(r^R_{\alpha,\beta}, t^R_{\alpha,\beta}\right) \to \left(r^L_{\beta,\alpha}, t^L_{\beta,\alpha}\right)$ and $\phi \to -\phi$ in Eqs. (5.8).

For the magnetic domain it was already presented that its evolution operator for the electrons is written as

$$\mathbf{U}(\varepsilon) = \begin{pmatrix} \cos\lambda - i\frac{\varepsilon/\varepsilon_\perp \sin\lambda}{\sqrt{\left(\frac{\varepsilon}{\varepsilon_\perp}\right)^2 - 1}} & -i\frac{\varepsilon/\varepsilon_\perp \sin\lambda}{\sqrt{\left(\frac{\varepsilon}{\varepsilon_\perp}\right)^2 - 1}} e^{i\theta} \\ i\frac{\varepsilon/\varepsilon_\perp \sin\lambda}{\sqrt{\left(\frac{\varepsilon}{\varepsilon_\perp}\right)^2 - 1}} e^{-i\theta} & \cos\lambda + i\frac{\varepsilon/\varepsilon_\perp \sin\lambda}{\sqrt{\left(\frac{\varepsilon}{\varepsilon_\perp}\right)^2 - 1}} \end{pmatrix}, \tag{5.10}$$

where its inverse is the transfer operator and is related to the scattering matrix via Eq. (2.7), satisfying the following scattering equation

$$\begin{pmatrix} c_L^- \\ c_R^+ \end{pmatrix} = \mathbf{S}_M^e \begin{pmatrix} c_L^+ \\ c_R^- \end{pmatrix}. \tag{5.11}$$

A similar relation links the incoming and outgoing holes;

$$\begin{pmatrix} b_L^- \\ b_R^+ \end{pmatrix} = \mathbf{S}_M^h \begin{pmatrix} b_L^+ \\ b_R^- \end{pmatrix}, \tag{5.12}$$

where $\mathbf{S}_M^h(\varepsilon) = -\sigma_z \mathbf{S}_M^{e*}(-\varepsilon)\sigma_z$[144]. By combining Eqs. (5.11) and (5.12), it is obtained the scattering matrix for the magnetic island, which reads

$$S_M = \begin{pmatrix} r_M & t'_M \\ t_M & r'_M \end{pmatrix} = \begin{pmatrix} S^e_{M,11} & 0 & S^e_{M,12} & 0 \\ 0 & S^h_{M,11} & 0 & S^h_{M,12} \\ S^e_{M,21} & 0 & S^e_{M,22} & 0 \\ 0 & S^h_{M,21} & 0 & S^h_{M,22} \end{pmatrix}, \tag{5.13}$$

satisfying the scattering equation

$$\left(c_L^-, b_L^-, c_R^+, b_R^+\right)^T = S_M \left(c_L^+, b_L^+, c_R^-, b_R^-\right)^T. \tag{5.14}$$

Here it is seen that each sub-matrix take a block diagonal form highlighting the fact that in the magnetic domain an electron cannot be converted into a hole and vice-versa, in contrast to the case of the SC-2DTI interface which only allows an electron (hole) to be reflected as a hole (electron) or be transmitted as a QP (QH) (see for instance Eq. (5.7)).

5.2 Andreev bound states

It was already stated in Sec. 2.1.1 and can be noted in the set of Eqs. 5.8(a)-(d), that in a NS interface if the energy is below the superconducting gap, then it is reflected with amplitude one. If there are two superconductors, one in each end of the device, like in a SNS juncture as it is in the present case, then an electron is captured and remains in the N region. These are the so-called Andreev bound states (ABS). Mathematically, this can be shown as follows; recall that in the non-superconducting region the amplitudes of the outgoing and incoming states

are related through the scattering matrix as described in Eq. (5.14). On the other hand, the Andreev reflection from the superconductor converts electrons to holes and vice-versa, having a complementary relation between c and b states

$$S_A \left(c_L^-, b_L^-, c_R^+, b_R^+\right)^T = \left(c_L^+, b_L^+, c_R^-, b_R^-\right)^T. \tag{5.15}$$

with

$$S_A = \exp\left[2i\frac{\varepsilon}{\Delta}\frac{l_S}{\xi_S} - i\arccos(\frac{\varepsilon}{\Delta})\right]\begin{pmatrix} 0 & \text{Diag}[e^{i\phi/2}, e^{-i\phi/2}] \\ \text{Diag}[e^{-i\phi/2}, e^{i\phi/2}] & 0 \end{pmatrix}. \tag{5.16}$$

In order to have a non-null solution, the relation

$$\det(\mathbb{1} - S_A S_M) = 0 \tag{5.17}$$

must be satisfied yielding to the ABS. This is the so-called compatibility equation [157]. and will be studied further in the following section.

5.2.1 ABS for one and two magnetic domains

The ABS for a single magnetic domain was already analyzed in Refs. [137, 140, 144]. Here the main results will be reviewed. Figure 5.2 shows the ABS as function of the superconducting phase difference ϕ for several lengths. The left panel of the figure corresponds to $\Gamma = 0$, which in turn corresponds to the situation with no magnetization, i.e., the junction with bare HES between the superconductors contacts. Two degenerate states corresponding to a Kramers' pair at the time-reversal symmetric case $\phi = 0, \text{mod}(2\pi)$ can be identified. The degeneracy is broken as ϕ advances with one of the states evolving to a higher energy and hybridizing with the QP continuum for $|\varepsilon| > \Delta$. A crossing point at zero energy takes place at $\phi = \pi$. For $\Gamma \neq 0$ time-reversal-symmetry is broken even for $\phi = 0$, and the degeneracy is consequently lifted. According to calculations [137, 144], Majorana modes are stabilized at the boundaries of the magnetic domain in the present case. Hence, the Andreev states with lowest absolute value of the energy result from the hybridization of these Majorana modes. These two states have different parity and cross at $\phi = \pi$. Since they are completely decoupled from the QP continuum, the spectrum is effectively 4π-periodic and so does the ac Josephson current if parity is conserved, in contrast to the $\Gamma = 0$ case, which is 2π-periodic due to the hybridization of the sub-gap states with the continuum.

An interesting feature to highlight is the fact that the Andreev spectra are qualitatively different in the case $\Gamma < 1$ (panel (b) of Fig. 5.2) and $\Gamma \geq 1$ (panel (c) of Fig. 5.2). For $\Gamma < 1$, several ABS may exist in the gap for large enough junctions, in addition to the ones with lowest absolute energy. Instead, for $\Gamma \geq 1$ the spectrum has only two Andreev states, which result from the hybridization of the two MZMs.

Let's turn now to the situation with two magnetic domains. Its spectra is presented in Fig. 5.3 for the situation where $L_{1,2} = L_m/2$, equal magnetization $\Gamma_{1,2} = \Gamma = Jm/\Delta$ and relative tilt orientation $\theta = \pi$.

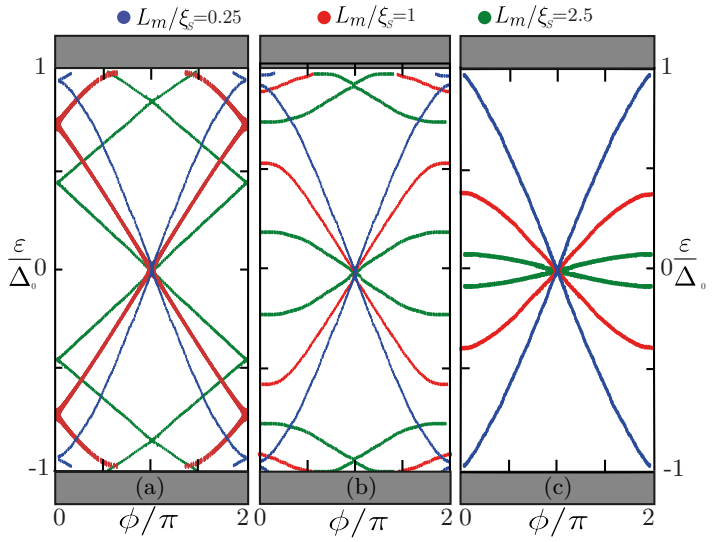

Figure 5.2: The Andreev spectra of the junction for a single magnetic domain of different lengths. Panel (a), (b) and (c) correspond to $\Gamma = 0; 0.5$ and 1 respectively. Grey bands indicate the continuum. Different colors correspond to different lengths $L_m/\xi_S = 0.25$(blue); 1 (red); 2.5 (green).

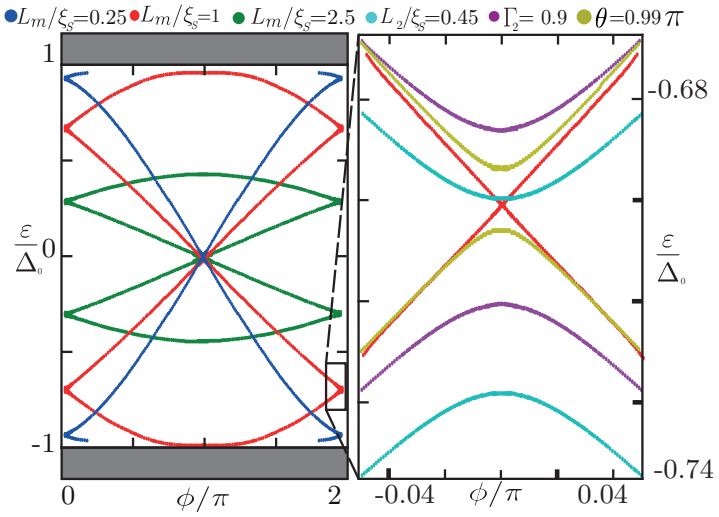

Figure 5.3: The Andreev spectra of the junction for two magnetic domain. Left panel correspond to $\Gamma = 1$ and $\theta = \pi$ and each domain of length $L_1 = L_2 = L_m/2$. Different colors correspond to different lengths, $L_m/\xi_S = 0.25, 1, 2.5$ of the full magnetic island. Grey band indicates the continuum spectrum. Black box indicates zoom on spectrum around $\phi = 0, \mathrm{mod}(2\pi)$ for two domains. Right panel correspond to Andreev spectra for two domains, in the range covered by the box of the left panel. Different lines correspond to a single parameter variation: $L_2 = 0.45\xi_S$ (light blue), $\theta = 0.99\pi$ (yellow) and $\Gamma_2 = 0.9$ (violet). Red line is the same in both panels.

Note that at $\phi = 0$, the system turns out to be invariant under spatial inversion symmetry with the point $x = x_S/2$, that is, the middle of the junction if at the same time the magnetic moments and spin are inverted. Therefore, the ABS turn out to be degenerated at $\phi = 0, \mathrm{mod}(2\pi)$ only in this very particular configuration (see the level crossing in the left panel of Fig. 5.3). A more general situation is presented in the right panel of Fig. 5.3 where the degeneracy is broken and a gap appears in the spectrum. This panel shows a zoom at $\phi = 0, \mathrm{mod}(2\pi)$ for configurations which slightly depart from the symmetric case with $L_m/\xi_S = 1$ (red plot in both panels of Fig. 5.3). Namely, for the light blue plot it was set $L_2 = 0.45\xi_S$, for the yellow plot $\theta = 0.99\pi$ and for the violet one we set $\Gamma_2 = 0.9$ while all the other parameters are equal to the symmetric case. The plot in red lines is for a reference and it is equal to the red one in the left panel. For all the configurations examined, the crossing at $\phi = \pi$ is topologically protected, as in the case of a single magnetic domain. The behavior, as a function of the coupling Γ, is also similar to the case of a single magnetic domain analyzed in Fig. 5.2. Namely, for $\Gamma > 1$ the spectrum is composed of only two Andreev states crossing at $\phi = \pi$, which can be identified as hybridized Majorana states.

5.3 Transmission function and thermal conductance

The thermal conductance can be obtained from the transmission function calculated via the **P**-matrix, as it was explained in Sec.2.2. The pairing potential as function of the temperature is modeled in the usual way as in the BCS theory [50, 158] with the interpolation formula, $\Delta(T) = \Delta_0 \tanh\left(1.74\sqrt{\frac{T_C}{T} - 1}\right)$, where T_C is the critical temperature and Δ_0 is the gap induced by proximity effect on the 2DTI, whose value is expected to be smaller than the corresponding in the bulk of the superconducting contact since it is the result of the proximity effect. For simplicity, we assume that the magnetic gap does not change in magnitude within the temperature range that it will be considered hereafter. Note that due to the temperature dependence on Δ, the transmission function depends also on T as well as on the other parameters, such as the amplitude of the magnetic coupling governed by the dimensionless parameter, Γ, the length of each magnet $L_{1,2}$, the superconducting phase difference ϕ and the relative tilt on the magnetic moment θ. An illustrative example of the transmission function is presented in Fig. 5.4 for the situation with one magnetic domain as function of ε and a magnetic coupling $\Gamma = 2(\xi_M = \xi_S/2)$. Each color represents a different length. Solid lines are for $T = 0.44T_C$ and dashed ones are for $T = 1.1T_C$. In the latter situation, the superconducting gap is closed and the transmission function coincides with the one for a magnetic island contacting the HES without superconductivity already presented in Ch. 4.

An interesting feature to notice is that the transmission of the QP is strongly suppressed when $L_m = 2\xi_S$ (corresponding to $L_m = 4\xi_M$) up to energies $\varepsilon \simeq 2\Delta_0$, for both temperatures. This stands as a clear manifestation that a gap is opened in the spectrum of the edge states when the length of the island is $L_m \gg \xi_M$, while for $T > T_C$ the gap is not fully developed for islands of length $L_m \simeq \xi_M$ or shorter. When the magnetic gap is not fully formed, the superconductivity can suppress

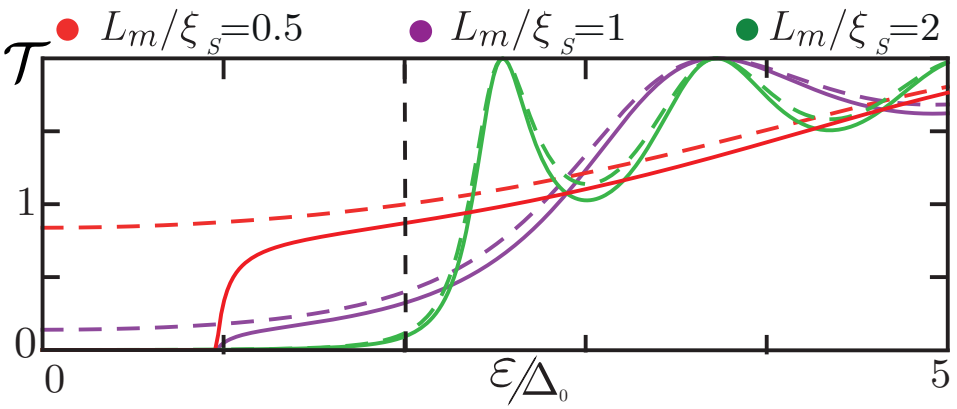

Figure 5.4: Transmission function for a single magnetic domain of length L_m embedded in the Josephson-junction with $\Gamma = 2$ ($\xi_M = \xi_S/2$) and $\phi = 0$. Solid lines correspond to $T = 0.44T_C$ while dashed lines correspond to $T = 1.1T_C$. Vertical line indicates the magnetic gap. Other details are in the figure.

the transmission. Indeed, within the low temperature regime (solid lines), superconductivity dominates, and the superconducting gap erases all the spectral features with energies $\varepsilon < \Delta(T)$. This implies that for the short magnets considered in the figure (with length $L_m < \xi_M$), the spectrum is still gapped, while there is a finite spectral weight at higher temperatures when the superconductivity is suppressed. On the other hand at energies $\varepsilon > \Delta(T)$, the transmission function has a structure of peaks and minima that depends on L_m. For low temperatures, the features above $\Delta(T)$ also depend on the superconducting phase difference ϕ (that was set to zero in the Fig. 5.4 for sake of simplicity). In conclusion, the longer the magnetic domain is, the more dominates the magnetic gap over the superconducting one. In fact, note that for the green plot, corresponding to $L_m = 2\xi_S = 4\xi_M$, there is a gap of amplitude $\Gamma\Delta_0$ (indicated with a vertical dashed line) regardless the temperature regime, while this is not the situation for the shorter magnetic domains, with $L_M = \xi_M,\ 2\xi_M$. This will be reflected in the behavior of the thermal conductance, to be discussed in the next section.

5.3.1 Thermal conductance of single magnetic domain

The take-home message of the previous section was that the temperature plays a key role in the competition of the two gaps. Namely, for $T \simeq T_C$, the higher the temperature is, the smaller the superconducting is and the magnetic gap becomes dominant. Focusing on the linear-response regime and only applying a temperature bias the thermal conductance calculated as Eq. (2.40) of Sec.2.2 reduces to

$$\kappa_{\rm th} = -\frac{1}{G_T}\int_{\Delta}^{\infty} d\varepsilon \varepsilon^2 \frac{\partial f}{\partial \varepsilon}\mathcal{T}(\varepsilon), \tag{5.18}$$

where the transmission function is

$$\mathcal{T}(\varepsilon) = \sum_{\alpha,\beta=e,h} P_{L,R}^{\alpha,\beta}, \tag{5.19}$$

and κ_{th} is the reduced thermal conductance normalized by the quantum bound $G_T = \pi^2 k^2 T/3h$ with k_B being the Boltzmann constant [68, 69, 159].

Figure 5.5 presents the reduced thermal conductance κ_{th} as a function of the temperature (solid lines). The top panel of the figure is for the situation $\Gamma = 1$ (where $\xi_M = \xi_S$) and the bottom panel for $\Gamma = 2$ (where $\xi_M = \xi_S/2$). A common feature, present in all the situations, is the exponentially vanishing values at $T = 0$, whereas at high temperatures it tends to saturate to the quantum bound $\kappa_{\text{th}} = 1$ [160–162]. Note that the situation $L = 0$ corresponds to a junction without TI with all the channels fully open when $T > T_C$.

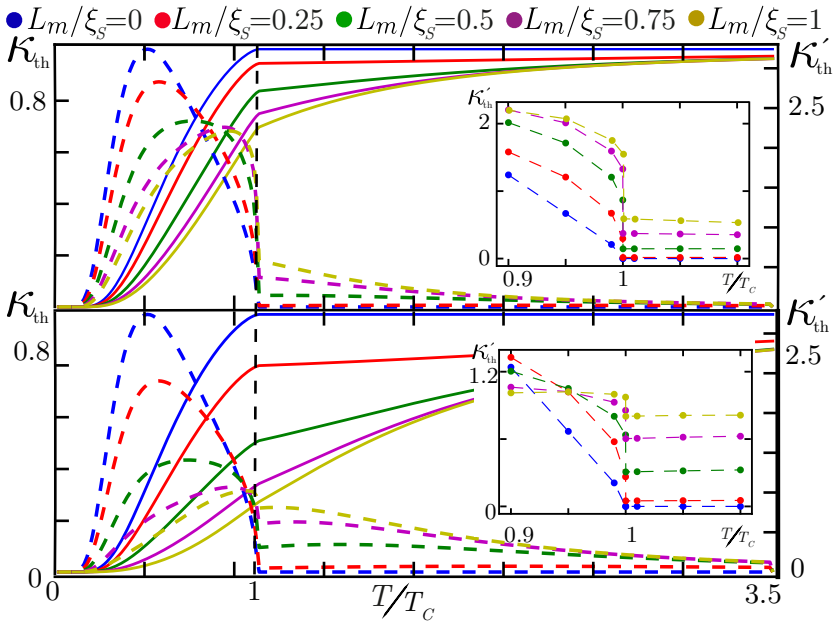

Figure 5.5: Relative thermal conductance $\kappa_{\text{th}}(T)$ (left axis, solid line) and its temperature derivative $\frac{d\kappa_{\text{th}}}{dT} = \kappa'_{\text{th}}$(right axis, dashed line) for a magnet with a single magnetic domain embedded in the Josephson-junction with $\phi = 0$. Top panel corresponds to $\Gamma = 1$ and bottom panel corresponds to $\Gamma = 2$. Black dashed vertical line indicates $T = T_C$. Inset: zoom of κ' near $T = T_C$. Other details are on the figure.

At finite length of the magnetic domain, the magnetic gap remains open regardless whether the superconducting gap is open or not, as stated when the transmission function was discussed. But at finite length, the quantum bound is achieved at higher temperatures. This feature is enhanced with increasing Γ (compare both panels of the figure). The changes in κ_{th} as the superconducting gap closes are more visible in the behavior of its derivative $\kappa'_{\text{th}} = d\kappa_{\text{th}}/dT$, which is shown in each panel with dashed lines. At $T = T_C$ the derivative presents a discontinuity, as expected when the phase transition happens between the superconducting and the non-superconducting regime. For $T > T_C$ the derivative of the thermal conductance monotonically increases with both Γ and L_m, while the opposite behavior takes place for $T < T_C$.

Another interesting features that can be analyzed are the interference patterns generated as a function of the superconducting phase ϕ, naturally for $T < T_C$ (recall that when $T > T_C$ there

is no superconductivity and therefore it can not be defined a phase difference). This quantum interference in the Josephson-junction is analyzed in Fig. 5.6. It presents $\kappa_{\rm th}$ as function of ϕ and L_m for a fixed T and each panel for a different value of Γ.

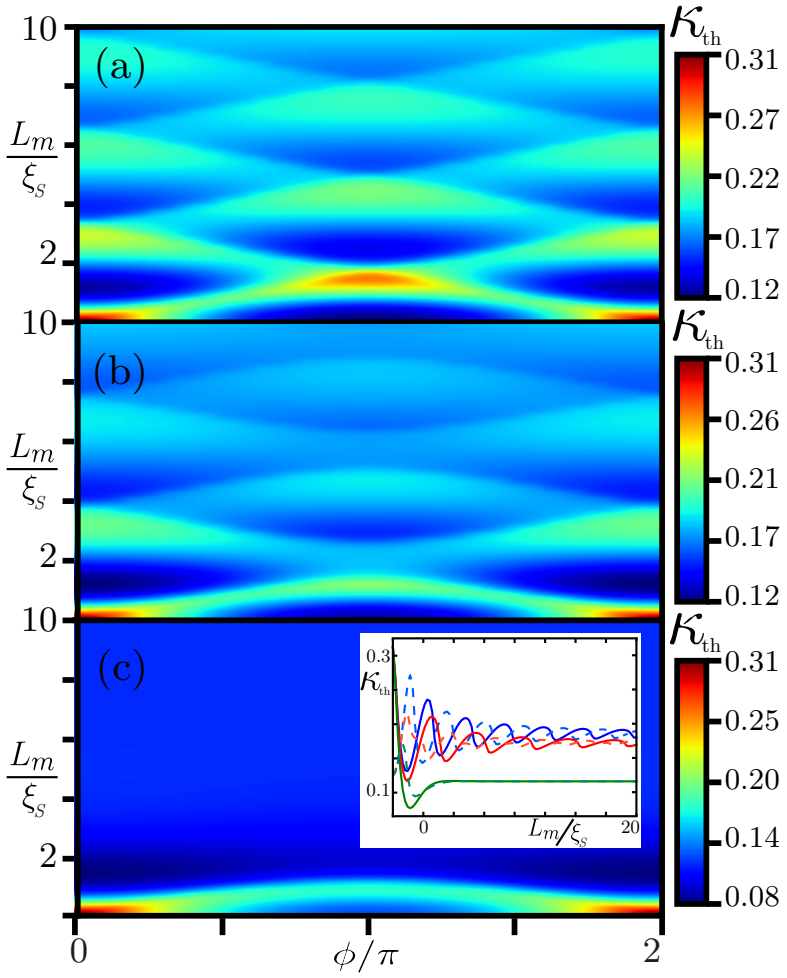

Figure 5.6: Relative thermal conductance of the junction with a single magnetic domain with temperature $T = 0.44T_C$. Different panels correspond to different ratios $\Gamma = Jm/\Delta_0$. Panel (a) corresponds to $\Gamma = 0$, panel (b) to $\Gamma = 0.5$ and panel (c) to $\Gamma = 1$. Inset in panel (c) is $\kappa_{\rm th}$ as function of L_m/ξ_S, blue line corresponds to $\Gamma = 0$, red line corresponds to $\Gamma = 0.5$ and green line corresponds to $\Gamma = 1$. Solid lines are for $\phi = 0$ and dashed lines are for $\phi = \pi$.

The limit where $\Gamma = 0$, is presented in panel (a). It corresponds to the junction without magnetic island and has been previously analyzed in Refs. [163–165] Some features to highlight are the oscillatory response; which is even and $2\pi-$ periodic in ϕ and the decreasing damping on L_m/ξ_S, as shown in panel (b) for $\Gamma = 0.5$. An inset is presented in panel (c) where $\kappa_{\rm th}$ is presented for $\phi = 0, \pi$ for $\Gamma = 0, 0.5$ and 1.

We see that for finite $\Gamma < 1$, the pattern of damped oscillations is very similar to the one without magnet (red and blue lines respectively in the inset). Notice, in particular, that besides a shift and a smaller amplitude, the period of the oscillations is basically the same in the cases with

$\Gamma = 0,\ 0.5$. Albeit, as the strength of the magnetic coupling is increased and overcomes $\Gamma = 1$, this response is much less sensitive to ϕ and decreases very fast with the length. This is consistent with a behavior dominated by the magnetic gap, even for temperatures below T_C, where the superconducting gap is finite. In the inset of panel (c) it can be appreciated how the thermal conductance tends to some limit when $L_m \gg \xi_S$ that depends on Γ but does not depend on ϕ. This saturation value is achieved as a limit of the damped oscillations for $\Gamma < 1$, while it is approached fast and without oscillations for $\Gamma \geq 1$.

5.3.2 Thermal conductance of two magnetic domains: appearance of a resonance

It was already explained in Sec. 4.2 that, in absence of superconductivity, two magnetic domains can generate a resonance inside the magnetic gap and this resonance is a manifestation of JR soliton. This feature is again, present when this system is at $T > T_C$. The transmission function of the superconducting junction with two magnetic domains is presented in Fig. 5.7 where both domains are of equal length and opposite magnetic orientation. The situation for $T < T_C$ is presented in solid lines and, the one for $T > T_C$ in dashed lines for $\Gamma = 2$. Again, as it

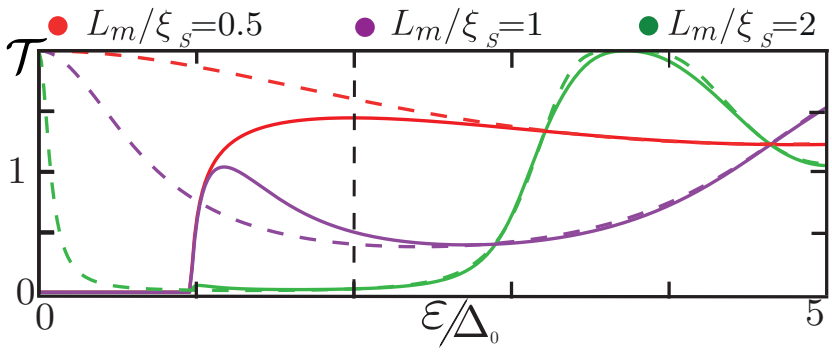

Figure 5.7: Transmission function for two magnetic domains of length $L_1 = L_2 = L_m/2$ with opposite orientation, $\theta = \pi$, and equal magnetization m, embedded in the Josephson-junction for $\Gamma = 2$ and $\phi = 0$. Solid lines correspond to $T = 0.44T_C$ while dashed lines correspond to $T = 1.1T_C$. Vertical dashed line indicates the magnetic gap. Other details are on the figure.

was presented in Sec. 4.2, the resonance that develops inside the gap at $T > T_C$ has a width that decreases with the length of the magnetic domain and for this parameters corresponds again to a realization of the JR zero mode. Due to the fact that for $T < T_C$ the superconducting gap dominates, there is no sign of the JR resonance in the transmission function for this range of temperatures. Despite this, there is a remarkable behavior in the reduced thermal conductance presented in Fig. 5.8.

As in the case of one magnetic domain, κ_{th} saturates at the quantum bound for $T > T_C$ and for all the situations presented, is exponentially small at low temperatures. But the main difference between both cases is the negative value of the derivative κ'_{th} right above T_C.

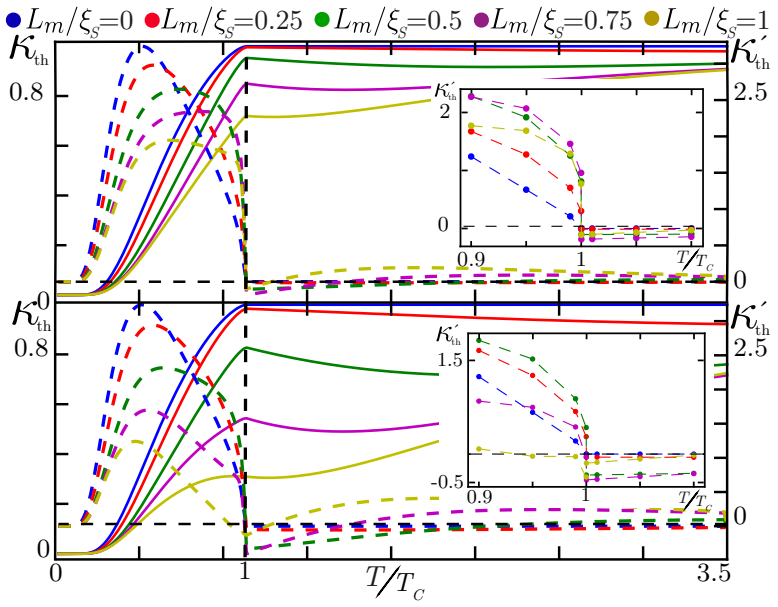

Figure 5.8: Relative Thermal conductance $\kappa_{\text{th}}(T)$ (left axis, solid lines) and its derivative κ'_{th} (right axis, dashed line) for two magnetic domains with opposite orientations, equal length $L_m/2$ and equal magnetizations $m_1 = m_2 = m$ for $\phi = 0$. Top panel corresponds to $\Gamma = 1$ and bottom panel corresponds to $\Gamma = 2$. Black dashed horizontal line on both panels indicates $\kappa'_{\text{th}} = 0$ while vertical line indicates $T = T_C$. Inset shows a zoom of κ' near $T = T_C$. Other details are on the figure.

This peculiar behavior can be traced back to the development of the resonant peak in the gap as the temperature overcomes the critical temperature. From the mathematical point of view, this can be understood by calculating the derivative with respect to the temperature on Eq. (5.18) which leads to

$$\kappa'_{\text{th}} = \frac{2\kappa_{\text{th}}}{T} - \frac{1}{G_T T}\int_0^\infty \varepsilon^3 \frac{\partial f}{\partial \varepsilon}\frac{\partial \mathcal{T}}{\partial \varepsilon} d\varepsilon, \tag{5.20}$$

when $T > T_C$. The first term on RHS is due to the contribution of G_T (recall that this quantity is linear with T) and is always positive. Instead, the sign of the second term depends on the sign of the derivative of the transmission function. Therefore, since $-\partial f/\partial \varepsilon > 0$, if $\partial \mathcal{T}/\partial \varepsilon$ is negative and the contribution of the second term is large enough, the derivative of the relative thermal conductance may be negative. This is precisely the case of the configuration with two magnetic domains due to the resonance where, within the window defined by the function $-\partial f/\partial \varepsilon$, the transmission function $\mathcal{T}(\varepsilon)$ has a negative slope, which leads to a large contribution to the integral when multiplied by ε^3. But this contribution becomes small as the length of the island increases and the resonance becomes narrow enough.

This property is not exclusive of the anti-parallel orientation, as it can be seen in Fig. 5.9, where κ'_{th} is shown as function of the relative orientation of the islands and the length for fixed Γ in each panel at a temperature just above T_C. Note that there is a wide range of lengths and orientations close to $\theta = \pi$ where κ'_{th} is negative. These cases, coincide with configurations leading

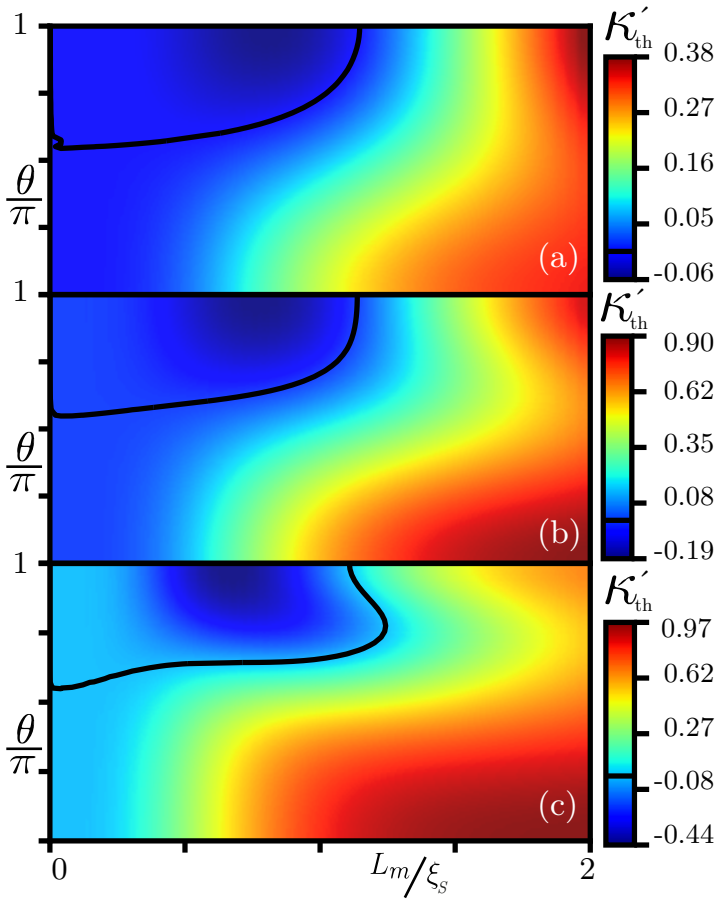

Figure 5.9: Derivative of the relative thermal conductance, κ'_{th} at $T = 1.01T_C$ as function of the relative tilt θ in the orientation of the magnetic moments with $L_m/2 = L_1 = L_2$ and $\phi = 0$. Panels (a), (b) and (c) correspond to $\Gamma = 0.5, 1, 2$, (with $\xi_M = 2\xi_S, \xi_S, \xi_S/2$) respectively. The black line in each panel indicates the boundary for the region with $\kappa'_{\text{th}} < 0$.

to resonant peaks of the transmission function inside the magnetic gap. Importantly, the width of the resonant peak scales with the inverse of the length of the magnetic island (see plots in dashed lines in Fig. 5.7). Hence, the impact of this feature in generating a negative derivative of the relative thermal conductance just above T_C becomes negligible as the length of the magnetic island increases. From these two results it can be concluded that, having $\kappa'_{\text{th}} < 0$ just above T_C can be regarded as an indication of the presence of a JR peak in a Josephson-junction. But this can be done only if $L_m \leq \xi$, that is, for sufficiently short magnetic domains.

As in the case of a single domain configuration, it is expected an interference patron in the thermal conductance as function on ϕ for temperatures below the critical value. This is presented in Fig. 5.10 for the case of two magnetic domains with opposite orientations of the magnetic moments ($\theta = \pi$). The interference pattern is still even and $2\pi-$ periodic in ϕ, but different from the one observed in Fig. 5.6 for a single domain. However, like in that case, as the length of the magnetic island increases and becomes significantly larger than ξ_M, the magnetic gaps dominates,

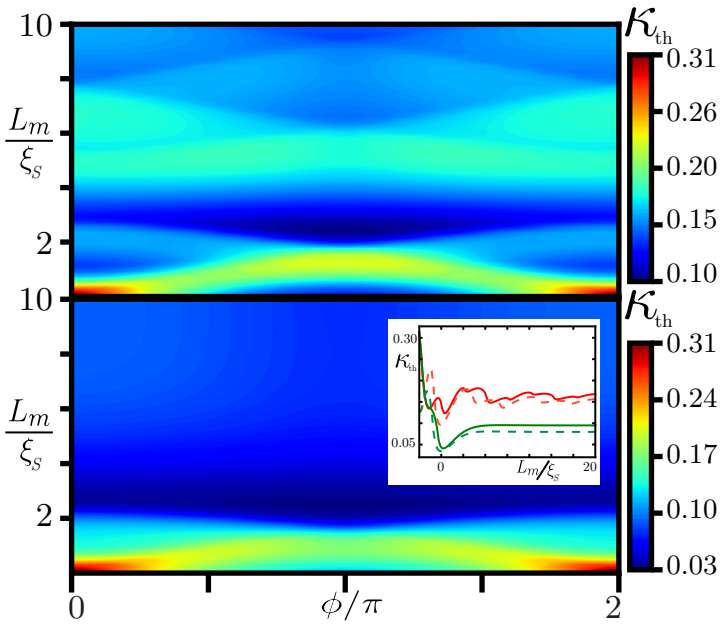

Figure 5.10: Relative thermal conductance of the junction with two magnetic domain with opposite magnetic moments and $L_1 = L_2 = L_m/2$ at temperature $T = 0.44T_C$. Upper and lower panels correspond to $\Gamma = J_m/\Delta_0 = 0.5,\ 1$ ($\xi_M = 2\xi_S,\ \xi_S$). The inset in the lower panel shows $\kappa_{\rm th}$ as function of L_m/ξ_S. Red line is for $\Gamma = 0.5$ and green line is $\Gamma = 1$ for $\phi = 0,\ (\pi)$ in solid (dashed) lines.

and the interference patron is suppressed. This is highlighted in the inset shown in the bottom panel of the figure and we can pose similar observations as in the case of the single magnetic domain. Namely, for $\Gamma \geq 1$, where the magnetic gap dominates, the conductance is practically non-sensitive to the superconducting phase ϕ and it decreases rapidly with L_m. Instead, for $\Gamma < 1$, the thermal conductance depends on ϕ and displays oscillations as a function of L_m. The pattern of such oscillations is very different and much less regular than the one observed in the junction without magnetic island (corresponding to $\Gamma = 0$). Hence, in the regime of $\Gamma < 1$, the interference pattern of the thermal conductance provides clear signatures of the domain structure of the magnetic island. Instead, for $\Gamma \geq 1$, the rapid suppression of the thermal conductance is an indication of the effect of the magnetic island, but no information on the domain structure can be extracted from that behavior.

To end this section, the combined effect of both ϕ and θ is analyzed for different lengths of the magnetic domain presented in Fig. 5.11. Results are shown for $\Gamma = 1$ ($\xi_M = \xi_S$), where it is expected the maximal interplay between both superconductor and magnetic scales when $T < T_C$. The figure highlights the fact that not only the superconducting phase bias ϕ generates interference patterns, but also the tilting angle θ. Furthermore, it can be observed that the specific features as function of ϕ are similar to those as function of θ. This is not surprising in the view of the duality relation between these two parameters [138].

Notice that such duality implies that similar physical properties should be observed if the magnetic islands are interchanged with the superconductors, with θ playing the role of ϕ and

vice-versa, due the similar structure of the massive terms, as is explicit in Eqs. (5.2). In the Josephson-junction configuration studied here, signatures of the aforementioned duality can be observed, in a context where the superconductors have infinite length, while the magnetic islands are finite. In fact, notice that panel (a), which corresponds to a purely superconducting junction has a pattern of straight vertical features, reflecting the sensitivity of the thermal conductance only with the phase bias ϕ. In the opposite limit of a long enough magnetic island shown in panel (d), the magnetic effect becomes dominant and the pattern tends to follow horizontal straight lines, indicating a sensitivity on the tilt θ but loosing the dependence on ϕ. Configurations between these two cases can be observed in panels (b) and (c). These results show that the interplay of the tilting angle and phase difference may be an interesting phenomenology in the studied system.

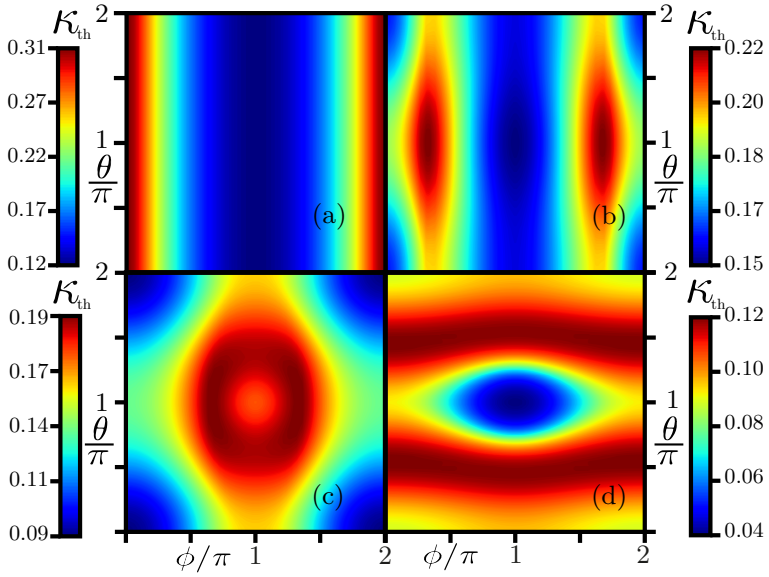

Figure 5.11: Relative thermal conductance $\kappa_{\rm th}(T = 0.44T_C)$ as function of the tilting angle in the orientation of the magnetic domains θ and the phase difference of the superconducting potentials ϕ for $\Gamma = 1$ ($\xi_M = \xi_S$) and $L_1 = L_2 = L_m/2$. Panel (a) corresponds to $L_m/\xi_S = 0$, panel (b) to $L_m/\xi_S = 0.5$, panel (c) to $L_m/\xi_S = 1$ and panel (d) to $L_m/\xi_S = 2$.

5.4 Conclusions of this chapter

As an extension of the study presented in chapter 4, in this chapter a two-dimensional topological insulator hosting magnetic domains with superconducting terminals was presented. The Andreev spectrum was found to be qualitatively similar in the two configurations analyzed here, consisting in one and two magnetic domains. On the other hand, it was analyzed the thermal conductance as a function of the temperature and the superconducting phase. It was shown that the concomitant behaviour is a result of the competition between the magnetic and superconducting gaps. The temperature dependence in the superconducting gap leads to a discontinuity in the derivative of the thermal conductance. With one magnetic domain it is always positive. But when there are

two magnetic domains this derivative may be negative for a set of orientations for temperatures a little higher than T_C. This behavior could be identified as a consequence of the presence of Jackiw-Rebbi modes and therefore studying the thermal conductance this system could be used as a method to identify the Jackiw-Rebbi resonances. So far, no experimental signatures of Jackiw-Rebbi resonances have been reported.

The Josephson current is not sensitive to the existence of this resonant state. Recall that the Josephson current is the derivative of the negative energies of the spectrum with respect the phase bias, including the quasiparticle continuum and the subgap Andreev states. It was found that regardless the configuration or orientation of the magnetic domain, the Andreev spectra remain quite similar and also similar to configurations without magnet. These results rule out the Josephson current as an appropriate witness quantity of the existence of a Jackiw-Rebbi mode. More importantly, the peak in the transmission probability associated to the Jackiw-Rebbi resonance develops when the superconducting gap closes, in which case there is no Josephson effect at all. Because of this, the thermal conductance is a more appropriated quantity to study it. It is a non-equilibrium quantity and depends not only on the spectrum, but more importantly on the transmission properties of the system, regardless its nature. The development of the Jackiw-Rebbi resonance above the critical temperature is associated to a large transmission probability at low energy and κ_{th} turns out to be sensitive to this changes.

The interference patterns of the reduced thermal conductance for temperatures below the critical one in both configurations were also analyzed as function of the superconducting phase bias. One and two magnetic domains have similar features, but in the latter situation, changing the superconducting phase with the magnetic orientation presents a similar pattern revealing the existing symmetry between the superconductor and magnetic domain.

According to the estimates presented in chapter 4, the magnetic domains are in the state of the art for fabrication having a length below $\xi_M \sim 10\,\mu\text{m}$ to $20\,\mu\text{m}$, which is of the same order of magnitude of the superconducting coherence length ξ_S and energy gaps of $J_m \sim 1.2\,\text{K}$ to $2.4\,\text{K}$ corresponding to a regime with $\Gamma \sim 1,2$ similar to the situation presented here, where the different features of κ_{th} as a function of ϕ below T_C, as well as the corresponding behavior as a function of temperature close to T_C, clearly distinguish the different type junctions.

CHAPTER 6

RESUMEN, CONCLUSIONES Y PERSPECTIVA A FUTURO

El objetivo de esta tesis fue estudiar las propiedades de transporte en sistemas en estado Hall cuántico y spin Hall cuántico con hipótesis muy simples pero poderosas como respuesta linear y transporte balístico, principalmente en el marco de la teoría de la matriz de scattering y la teoría de Landauer-Büttiker. Cada capítulo fue dedicado al estudio de diferentes nanoestructuras con el foco en las propiedades térmicas y termoeléctricas.

En el capítulo 3, se presentó un sistema en régimen de Hall cuántico con geometría circular llamado disco Corbino. Esta geometría particular resulto ser útil para desacoplar los componentes radial y angular de las direcciones de transporte, dejando solamente la corriente radial cuando un calentador (heater) es aplicado en el centro de la muestra. Se propuso una función de transmisión, elemento clave en la teoría de Landauer-Büttiker, la cual predice la conductancia eléctrica y la respuesta termoeléctrica. Se encontró también que, a diferencia con las barras Hall, no fue necesario considerar en esta teoría arrastre por fonones (phonon-drag). A su vez, se pudo predecir muy bien el gradiente térmico desarrollado, estando de acuerdo con estimaciones previas. Se encontró una gran figura de mérito, mucho mayor que otros dispositivos en el análisis de la performance termoeléctrica.

En el capítulo 4, se estudió un sistema en estado de spin Hall cuántico que presenta canales de borde contra-propagantes con diferente orientación de spin acoplados a dominios magnéticos. Se mostró que esta configuración reúne las condiciones necesarias para alcanzar gran performance termoeléctrica. Esto es una consecuencia de la apertura del gap en el espectro de energías de los modos propagantes. Dependiendo del rango de energía y de la configuración de los dominios magnéticos, la función de transmisión tiene características similares a una función Θ-Heaviside, así también como a una función Lorentziana, similares a una función Δ-Dirac, que se sabe que son óptimos para la producción de alta potencia y la figura de mérito respectivamente. Se mostró

también que, en la presencia de dos dominios con orientaciones antiparalelas en los momentos magnéticos, aparece una resonancia en el gap. Esto es una realización de los modos de energía cero de Jackiw-Rebbi y es robusto frente a perturbaciones en los parámetros.

Finalmente, en el capítulo 5, al sistema anterior se le agregaron dos terminales superconductoras. Este ingrediente agrega un gap superconductor que compite con el gap magnético generado por el dominio. Se mostró que, notablemente, la conductancia térmica tiene información sobre la estructura. En particular, si hay un solo dominio magnético, la derivada de la conductancia térmica con respecto de la temperatura es siempre positiva, mientras que, si hay dos, la derivada puede ser negativa, justo por encima de la temperatura crítica de la terminal superconductora revelando la existencia de los estados resonantes de Jackiw-Rebbi.

A pesar de este intenso trabajo, hay mucho para hacer en cada dirección. Por ejemplo, una posible continuación del trabajo desarrollado en el capítulo 3 podría focalizarse en tratar de entender las grandes señales observadas en el V_{TP} desde un punto de vista teórico diferente y realizando otro tipo de mediciones para probar el modelo. Otra posible continuación podría ser usar el dispositivo Corbino como un termómetro, usando la conductancia y relacionando como cambia en un punto, por ejemplo, en un mínimo, cuando se cambia la temperatura. Después de esto, el Corbino podría ser usado para probar si un sistema puede ser refrigerado como se predice. Algunos avances en esta dirección desde un punto de vista teórico ya se han hecho en Ref. [102] y el estudio se extendió fuera de la respuesta lineal. Con respecto a la investigación desarrollada el capítulo 4, el capítulo 5, es en si una continuación. Sin superconductividad una continuación ya se hizo en la Ref. [117] donde el estudio se extendió fuera de la respuesta lineal y se focalizó en la potencia de enfriamiento y en el coeficiente de performance del dispositivo. Otra posible continuación podría ser agregar una interacción entre los canales de borde. De esta forma con superconductividad, extendiendo la investigación del capítulo 5, fuera de la respuesta lineal e introduciendo algún mecanismo para romper la simetría partícula agujero, por ejemplo, un polarizador de spin, se podría llegar a fenómenos termoeléctricos interesantes.

BIBLIOGRAPHY

[1] K. von Klitzing, G. Dorda, and M. Pepper, "New method for high-accuracy determination of the fine-structure constant based on quantized Hall resistance," *Phys. Rev. Lett.*, vol. 45, no. 6, p. 494, 1980.

[2] K. von Klitzing, "The quantized Hall effect," *Rev. M. Phys.*, vol. 58, no. 3, p. 519, 1986.

[3] J. Fröhlich and T. Kerler, "Universality in quantum Hall systems," *Nucl. Phys. B*, vol. 354, no. 2-3, pp. 369–417, 1991.

[4] W. Li, G. Csáthy, D. Tsui, L. Pfeiffer, and K. West, "Scaling and universality of integer quantum Hall plateau-to-plateau transitions," *Phys. Rev. Lett.*, vol. 94, no. 20, p. 206807, 2005.

[5] A. Hartland, "The quantum Hall effect and resistance standards," *Metrologia*, vol. 29, no. 2, p. 175, 1992.

[6] K. Novoselov, Z. Jiang, Y. Zhang, S. Morozov, H. Stormer, U. Zeitler, J. Maan, G. Boebinger, P. Kim, and A. Geim, "Room-temperature quantum hall effect in graphene," *Science*, vol. 315, no. 5817, pp. 1379–1379, 2007.

[7] Z. Jiang, Y. Zhang, Y. Tan, H. Stormer, and P. Kim, "Quantum Hall effect in graphene," *Solid State Commun.*, vol. 143, no. 1-2, pp. 14–19, 2007.

[8] R. Ribeiro-Palau, F. Lafont, J. Brun-Picard, D. Kazazis, A. Michon, F. Cheynis, O. Couturaud, C. Consejo, B. Jouault, W. Poirier, and F. Schopfer, "Quantum Hall resistance standard in graphene devices under relaxed experimental conditions," *Nature Nanotech.*, vol. 10, no. 11, pp. 965–971, 2015.

[9] R. Tao and F. Haldane, "Impurity effect, degeneracy, and topological invariant in the quantum Hall effect," *Phys. Rev. B*, vol. 33, no. 6, p. 3844, 1986.

[10] H. Aoki and T. Ando, "Universality of quantum Hall effect: topological invariant and observable," *Phys. Rev. Lett.*, vol. 57, no. 24, p. 3093, 1986.

[11] D. Thouless, M. Kohmoto, M. Nightingale, and M. den Nijs, "Quantized Hall conductance in a two-dimensional periodic potential," *Phys. Rev. Lett.*, vol. 49, no. 6, p. 405, 1982.

[12] K. Ishikawa and T. Matsuyama, "A microscopic theory of the quantum Hall effect," *Nucl. Phys. B*, vol. 280, pp. 523–548, 1987.

[13] T. Gerster, A. Müller, L. Freise, D. Reifert, D. Maradan, P. Hinze, T. Weimann, H. Marx, K. Pierz, H. Schumacher, *et al.*, "Robust formation of quantum dots in GaAs/AlGaAs heterostructures for single-electron metrology," *Metrologia*, vol. 56, no. 1, p. 014002, 2018.

[14] D. Newell, F. Cabiati, J. Fischer, K. Fujii, S. Karshenboim, H. Margolis, E. de Mirandes, P. Mohr, F. Nez, K. Pachucki, T. Quin, B. Taylor, M. Wang, W. B., and Z. Zhang, "The CODATA 2017 values of h, e, k, and N_A for the revision of the SI," *Metrologia*, vol. 55, no. 1, p. L13, 2018.

[15] E. Fradkin, *Field theories of condensed matter physics*.
Cambridge University Press, 2013.

[16] Z. Ezawa, *Quantum Hall effects: Field theoretical approach and related topics*.
World Scientific Publishing Company, 2008.

[17] K. von Klitzing, "Quantum Hall effect: discovery and application," *A. Rev. Cond. Matt. Phys.*, vol. 8, pp. 13–30, 2017.

[18] K. von Klitzing, T. Chakraborty, P. Kim, V. Madhavan, X. Dai, J. McIver, Y. Tokura, L. Savary, D. Smirnova, A. Rey, C. Felser, J. Gooth, and X. Qi, "40 years of the quantum Hall effect," *Nat. Rev. Phys.*, vol. 2, no. 8, pp. 397–401, 2020.

[19] M. Cage, K. von Klitzing, A. Chang, F. Duncan, M. Haldane, R. Laughlin, A. Pruisken, and D. Thouless, *The quantum Hall effect*.
Springer Science & Business Media, 2012.

[20] C. Cohen-Tannoudji, B. Diu, and F. Laloe, *Quantum Mechanics*.
Wiley-Interscience, 2006.

[21] R. Laughlin, "Quantized Hall conductivity in two dimensions," *Phys. Rev. B*, vol. 23, no. 10, p. 5632, 1981.

[22] R. Nakai, S. Ryu, and K. Nomura, "Laughlin's argument for the quantized thermal Hall effect," *Phys. Rev. B*, vol. 95, no. 16, p. 165405, 2017.

[23] B. Halperin, "Quantized Hall conductance, current-carrying edge states, and the existence of extended states in a two-dimensional disordered potential," *Phys. Rev. B*, vol. 25, no. 4, p. 2185, 1982.

[24] T. Ando, Y. Matsumoto, and Y. Uemura, "Theory of Hall effect in a two-dimensional electron system," *J. Phys. Soc. Japan*, vol. 39, no. 2, pp. 279–288, 1975.

[25] B. Bernevig, *Topological insulators and topological superconductors*.
Princeton university press, 2013.

[26] J. Asbóth, L. Oroszlány, and A. Pályi, *A short course on topological insulators*.
Springer, 2016.

[27] M. Franz and L. Molenkamp, *Topological insulators*.
Elsevier, 2013.

[28] A. Bohm, A. Mostafazadeh, H. Koizumi, Q. Niu, and J. Zwanziger, *The Geometric phase in quantum systems: foundations, mathematical concepts, and applications in molecular and condensed matter physics*.
Springer Science & Business Media, 2013.

[29] C. Kane and E. Mele, "Quantum spin Hall effect in graphene," *Phys. Rev. Lett.*, vol. 95, no. 22, p. 226801, 2005.

[30] B. Bernevig and S. Zhang, "Quantum spin Hall effect," *Phys. Rev. Lett.*, vol. 96, no. 10, p. 106802, 2006.

[31] C. Kane and E. Mele, "Z_2 topological order and the quantum spin Hall effect," *Phys. Rev. Lett.*, vol. 95, no. 14, p. 146802, 2005.

[32] B. Bernevig, T. Hughes, and S. Zhang, "Quantum spin Hall effect and topological phase transition in HgTe quantum wells," *Science*, vol. 314, no. 5806, pp. 1757–1761, 2006.

[33] M. König, S. Wiedmann, C. Brüne, A. Roth, H. Buhmann, L. Molenkamp, X. Qi, and S. Zhang, "Quantum spin Hall insulator state in HgTe Quantum Wells," *Science*, vol. 318, no. 5851, pp. 766–770, 2007.

[34] M. König, H. Buhmann, L. W. Molenkamp, T. Hughes, C. X. Liu, X. L. Qi, and S. C. Zhang, "The quantum spin Hall effect: theory and experiment," *J. Phys. Soc. Japan*, vol. 77, no. 3, p. 031007, 2008.

[35] C. Brüne, A. Roth, H. Buhmann, E. M. Hankiewicz, L. W. Molenkamp, J. Maciejko, X. L. Qi, and S. C. Zhang, "Spin polarization of the quantum spin Hall edge states," *Nature Phys.*, vol. 8, no. 6, pp. 485–490, 2012.

[36] A. Roth, C. Brüne, H. Buhmann, L. Molenkamp, J. Maciejko, X. Qi, and S. Zhang, "Nonlocal transport in the quantum spin Hall state," *Science*, vol. 325, no. 5938, pp. 294–297, 2009.

[37] J. Sinova, D. Culcer, Q. Niu, N. Sinitsyn, T. Jungwirth, and A. MacDonald, "Universal intrinsic spin Hall effect," *Phys. Rev. Lett.*, vol. 92, no. 12, p. 126603, 2004.

[38] F. D. M. Haldane, "Model for a quantum Hall effect without Landau levels: Condensed-matter realization of the parity anomaly," *Phys. Rev. Lett.*, vol. 61, no. 18, p. 2015, 1988.

[39] J. Maciejko, T. L. Hughes, and S. Zhang, "The quantum spin Hall effect," *Ann. Rev. Cond. Matt. Phys.*, vol. 2, no. 1, pp. 31–53, 2011.

[40] K. Nowack, E. Spanton, M. Baenninger, M. König, J. Kirtley, B. Kalisky, C. Ames, P. Leubner, C. Brüne, H. Buhmann, M. L., G.-G. D., and M. K., "Imaging currents in HgTe quantum wells in the quantum spin Hall regime," *Nature Mat.*, vol. 12, no. 9, pp. 787–791, 2013.

[41] D. Sheng, Z. Weng, L. Sheng, and F. Haldane, "Quantum spin-Hall effect and topologically invariant Chern numbers," *Phys. Rev. Lett.*, vol. 97, no. 3, p. 036808, 2006.

[42] C. Kane, "Graphene and the quantum spin Hall effect," *Int. J. Mod. Phys. B*, vol. 21, pp. 1155–1164, 2007.

[43] C. Xu and J. Moore, "Stability of the quantum spin Hall effect: Effects of interactions, disorder, and Z_2 topology," *Phys. Rev. B*, vol. 73, no. 4, p. 045322, 2006.

[44] R. Shindou and S. Murakami, "Effects of disorder in three-dimensional Z 2 quantum spin Hall systems," *Phys. Rev. B*, vol. 79, no. 4, p. 045321, 2009.

[45] J. Bardeen, L. Cooper, and J. Schrieffer, "Theory of superconductivity," *Phys. Rev.*, vol. 108, no. 5, p. 1175, 1957.

[46] H. Kamerlingh Onnes, "Further experiments with liquid helium. C. On the change of electric resistance of pure metals at very low temperatures etc. IV. The resistance of pure mercury at helium temperatures," *Comm. Phys. Lab. Univ. Leiden*, vol. 120b, 1991.

[47] W. Meissner and R. Ochsenfeld, "Ein neuer effekt bei eintritt der supraleitfähigkeit," *Naturwissenschaften*, vol. 21, no. 44, pp. 787–788, 1933.

[48] P. Kapitza, "Viscosity of liquid helium below the λ-point," *Nature*, vol. 141, no. 3558, pp. 74–74, 1938.

[49] N. Bogoliubov, "On the theory of superfluidity," *J. Phys*, vol. 11, no. 1, p. 23, 1947.

[50] M. Tinkham, *Introduction to superconductivity*.
Courier Corporation, 2004.

[51] J. Keterson and S. Song, *Superconductivity*.
Cambridge Press, 1999.

[52] Y. Blanter and M. Büttiker, "Shot noise in mesoscopic conductors," *Phys. Rep.*, vol. 336, no. 1-2, pp. 1–166, 2000.

[53] J. Schrieffer, *Theory of superconductivity*.
CRC press, 2018.

[54] A. L. Fetter and J. D. Walecka, *Quantum theory of many-particle systems*.
Courier Corporation, 2012.

[55] G. Blonder, M. Tinkham, and T. Klapwijk, "Transition from metallic to tunneling regimes in superconducting microconstrictions: Excess current, charge imbalance, and supercurrent conversion," *Phys. Rev. B*, vol. 25, no. 7, p. 4515, 1982.

[56] M. Moskalets, *Scattering matrix approach to non-stationary quantum transport*.
World Scientific, 2011.

[57] Y. Nazarov and Y. Blanter, *Quantum transport: introduction to nanoscience*.
Cambridge university press, 2009.

[58] P. Jacquod, R. Whitney, J. Meair, and M. Büttiker, "Onsager relations in coupled electric, thermoelectric, and spin transport: The tenfold way," *Phys. Rev. B*, vol. 86, no. 15, p. 155118, 2012.

[59] J. Krommes and G. Hu, "General theory of Onsager symmetries for perturbations of equilibrium and nonequilibrium steady states," *Phys. Fluids B*, vol. 5, no. 11, pp. 3908–3941, 1993.

[60] A. Altland and M. R. Zirnbauer, "Nonstandard symmetry classes in mesoscopic normal-superconducting hybrid structures," *Phys. Rev. B*, vol. 55, no. 2, p. 1142, 1997.

[61] S. Datta, *Electronic transport in mesoscopic systems*.
Cambridge University Press, 1997.

[62] Y. Imry, "Introduction to Mesoscopic Physics Oxford UP," *New York*, 1997.

[63] J. Sauls, "Andreev bound states and their signatures," *Phil. Trans. R. Soc. A.*, vol. 376, 2018.

[64] J. Zhu, *Bogoliubov-de-Gennes method and its applications*, vol. 924.
Springer, 2016.

[65] B. Pannetier and H. Courtois, "Andreev reflection and proximity effect," *J. Low Temp. Phys.*, vol. 118, no. 5, pp. 599–615, 2000.

[66] A. Martín-Rodero and A. Levy Yeyati, "Josephson and andreev transport through quantum dots," *Advances in Physics*, vol. 60, no. 6, pp. 899–958, 2011.

[67] A. Zazunov, R. Egger, and A. Levy Yeyati, "Low-energy theory of transport in Majorana wire junctions," *Phys. Rev. B*, vol. 94, no. 1, p. 014502, 2016.

[68] G. Benenti, G. Casati, K. Saito, and R. Whitney, "Fundamental aspects of steady-state conversion of heat to work at the nanoscale," *Phys. Rep.*, vol. 694, pp. 1–124, 2017.

[69] C. Lambert and R. Raimondi, "Phase-coherent transport in hybrid superconducting nanostructures," *J. Phys.: Cond. Matt.*, vol. 10, no. 5, p. 901, 1998.

[70] C. Beenakker, "Random-matrix theory of quantum transport," *Rev. Modern Phys.*, vol. 69, no. 3, p. 731, 1997.

[71] N. Claughton and C. Lambert, "Thermoelectric properties of mesoscopic superconductors," *Phys. Rev. B*, vol. 53, no. 10, p. 6605, 1996.

[72] S. Pershoguba, T. Veness, and L. Glazman, "Landauer Formula for a Superconducting Quantum Point Contact," *Phys. Rev. Lett.*, vol. 123, no. 6, p. 067001, 2019.

[73] S. Pershoguba and L. Glazman, "Thermopower and thermal conductance of a superconducting quantum point contact," *Phys. Rev. B*, vol. 99, no. 13, p. 134514, 2019.

[74] S. Carnot, "Réflexions sur la puissance motrice du feu et sur les machines propres à développer cette puissance," in *Annales scientifiques de l'École Normale Supérieure*, vol. 1, pp. 393–457, 1872.

[75] N. Read and G. Moore, "Fractional quantum Hall effect and Non-Abelian statistics," *Progress of Theoretical Physics Supplement*, vol. 107, pp. 157–166, 1992.

[76] A. Stern, "Non-Abelian states of matter," *Nature*, vol. 464, no. 7286, pp. 187–193, 2010.

[77] Y. Barlas and K. Yang, "Thermopower of quantum Hall states in Corbino geometry as a measure of quasiparticle entropy," *Phys. Rev. B*, vol. 85, no. 19, p. 195107, 2012.

[78] K. Yang and B. Halperin, "Thermopower as a possible probe of non-Abelian quasiparticle statistics in fractional quantum Hall liquids," *Phys. Rev. B*, vol. 79, no. 11, p. 115317, 2009.

[79] S. Maximov, M. Gbordzoe, H. Buhmann, L. Molenkamp, and D. Reuter, "Low-field diffusion magnetothermopower of a high-mobility two-dimensional electron gas," *Phys. Rev. B*, vol. 70, no. 12, p. 121308, 2004.

[80] B. Tieke, U. Zeitler, R. Fletcher, S. Wiegers, A. Geim, J. Maan, and M. Henini, "Even-denominator filling factors in the thermoelectric power of a two-dimensional electron gas," *Phys. Rev. Lett.*, vol. 76, no. 19, p. 3630, 1996.

[81] T. Fromhold, P. Butcher, G. Qin, B. Mulimani, J. Oxley, and B. Gallagher, "Phonon-drag magnetothermopower oscillations in GaAs/As x Ga 1- x As heterojunctions," *Phys. Rev. B*, vol. 48, no. 8, p. 5326, 1993.

[82] R. Fletcher, M. D'Iorio, W. Moore, and R. Stoner, "A search for trends in the thermopower of GaAs-Ga1-xAlxAs heterojunctions," *J. Phys. C*, vol. 21, no. 14, p. 2681, 1988.

[83] V. Dolgopolov, A. Shashkin, N. Zhitenev, S. Dorozhkin, and K. von Klitzing, "Quantum Hall effect in the absence of edge currents," *Phys. Rev. B*, vol. 46, no. 19, p. 12560, 1992.

[84] W. Chickering, L. Eisenstein, J.and Pfeiffer, and K. West, "Thermopower of two-dimensional electrons at filling factors $\nu = 3/2 and 5/2$," *Phys. Rev. B*, vol. 81, no. 24, p. 245319, 2010.

[85] W. Chickering, J. Eisenstein, L. Pfeiffer, and K. West, "Thermoelectric response of fractional quantized Hall and reentrant insulating states in the $N = 1$ Landau level," *Phys. Rev. B*, vol. 87, no. 7, p. 075302, 2013.

[86] J. Wolfe, *Imaging phonons: acoustic wave propagation in solids*.
Cambridge University Press, 2005.

[87] P. Märki, B. Braem, and T. Ihn, "Temperature-stabilized differential amplifier for low-noise DC measurements," *Rev. Sci. Instrum.*, vol. 88, no. 8, p. 085106, 2017.

[88] K. Seeger, *Semiconductor physics*.
Springer Science & Business Media, 2013.

[89] J. Harris, J. Pals, and R. Woltjer, "Electronic transport in low-dimensional structures," *Reports on progress in Physics*, vol. 52, no. 10, p. 1217, 1989.

[90] K. von Klitzing, J. Nieder, R. Haug, G. Muller, S. Koch, D. Weiss, and K. Ploog, "Influence of ohmic contacts on the amplitude of Shubnikov-de Haas oscillations," *Semicond. Sci. Technol.*, vol. 7, no. 1, p. 82, 1992.

[91] L. Chang, H. Sakaki, C. Chang, and L. Esaki, "Shubnikov—de Haas oscillations in a semiconductor superlattice," *Phys. Rev. Lett.*, vol. 38, no. 25, p. 1489, 1977.

[92] R. Haug, K. von Klitzing, and K. Ploog, "Analysis of the asymmetry in Shubnikov-de Haas oscillations of two-dimensional systems," *Phys. Rev. B*, vol. 35, no. 11, p. 5933, 1987.

[93] S. Kobayakawa, A. Endo, and Y. Iye, "Diffusion thermopower of quantum Hall states measured in Corbino geometry," *J. Phys. Soc. Japan*, vol. 82, no. 5, p. 053702, 2013.

[94] M. Johnson and S. Girvin, "Thermoelectric effect in a weakly disordered inversion layer subject to a quantizing magnetic field," *Phys. Rev. B*, vol. 29, no. 4, p. 1939, 1984.

[95] W. Pan, J. Xia, V. Shvarts, D. Adams, H. Stormer, D. Tsui, L. Pfeiffer, K. Baldwin, and K. West, "Exact quantization of the even-denominator fractional quantum Hall state at ν= 5/2 Landau level filling factor," *Phys. Rev. Lett.*, vol. 83, no. 17, p. 3530, 1999.

[96] W. Pan, J. Xia, H. Stormer, D. Tsui, C. Vicente, E. Adams, N. Sullivan, L. Pfeiffer, K. Baldwin, and K. West, "Experimental studies of the fractional quantum Hall effect in the first excited Landau level," *Phys. Rev. B*, vol. 77, no. 7, p. 075307, 2008.

[97] H. Choi, W. Kang, S. Das Sarma, L. Pfeiffer, and K. West, "Activation gaps of fractional quantum Hall effect in the second Landau level," *Phys. Rev. B*, vol. 77, no. 8, p. 081301, 2008.

[98] P. Roura-Bas, L. Arrachea, and E. Fradkin, "Helical spin thermoelectrics controlled by a side-coupled magnetic quantum dot in the Quantum Spin Hall state," *Phys. Rev. B*, vol. 98, no. 19, p. 195429, 2018.

[99] P. Roura-Bas, L. Arrachea, and E. Fradkin, "Enhanced thermoelectric response in the fractional quantum Hall effect," *Phys. Rev. B*, vol. 97, no. 8, p. 081104, 2018.

[100] J. He and T. M. Tritt, "Advances in thermoelectric materials research: Looking back and moving forward," *Science*, vol. 357, no. 6358, 2017.

[101] A. Ozaeta, P. Virtanen, F. Bergeret, and T. Heikkilä, "Predicted very large thermoelectric effect in ferromagnet-superconductor junctions in the presence of a spin-splitting magnetic field," *Phys. Rev. Lett.*, vol. 112, no. 5, p. 057001, 2014.

[102] J. Herrera Mateos, M. Real, C. Reichl, A. Tonina, W. Wegscheider, W. Dietsche, and L. Arrachea, "Thermoelectric cooling properties of a quantum Hall Corbino device," *Phys. Rev. B*, vol. 103, no. 12, p. 125404, 2021.

[103] G. Benenti, K. Saito, and G. Casati, "Thermodynamic bounds on efficiency for systems with broken time-reversal symmetry," *Phys. Rev. Lett.*, vol. 106, no. 23, p. 230602, 2011.

[104] R. Whitney, "Finding the quantum thermoelectric with maximal efficiency and minimal entropy production at given power output," *Phys. Rev. B*, vol. 91, no. 11, p. 115425, 2015.

[105] G. Granger, J. Eisenstein, and J. Reno, "Observation of chiral heat transport in the quantum Hall regime," *Phys. Rev. Lett.*, vol. 102, no. 8, p. 086803, 2009.

[106] S. Nam, E. Hwang, and H. Lee, "Thermoelectric detection of chiral heat transport in graphene in the quantum Hall regime," *Phys. Rev. Lett.*, vol. 110, no. 22, p. 226801, 2013.

[107] A. Cappelli, M. Huerta, and G. Zemba, "Thermal transport in chiral conformal theories and hierarchical quantum Hall states," *Nuc. Phys. B*, vol. 636, no. 3, pp. 568–582, 2002.

[108] E. Grosfeld and S. Das, "Probing the neutral edge modes in transport across a point contact via thermal effects in the Read-Rezayi non-Abelian quantum Hall states," *Phys. Rev. Lett.*, vol. 102, no. 10, p. 106403, 2009.

[109] T. Karzig, G. Refael, L. Glazman, and F. von Oppen, "Energy Partitioning of Tunneling Currents into Lüttinger Liquids," *Phys. Rev. Lett.*, vol. 107, no. 17, p. 176403, 2011.

[110] H. Aita, L. Arrachea, C. Naón, and E. Fradkin, "Heat transport through Quantum Hall edge states: Tunneling versus capacitive coupling to reservoirs," *Phys. Rev. B*, vol. 88, no. 8, p. 085122, 2013.

[111] G. Viola, S. Das, E. Grosfeld, and A. Stern, "Thermoelectric probe for neutral edge modes in the fractional quantum hall regime," *Phys. Rev. Lett.*, vol. 109, no. 14, p. 146801, 2012.

[112] D. Rothe, E. Hankiewicz, B. Trauzettel, and M. Guigou, "Spin-dependent thermoelectric transport in HgTe/CdTe quantum wells," *Phys. Rev. B*, vol. 86, no. 16, p. 165434, 2012.

[113] L. Arrachea and E. Fradkin, "Chiral heat transport in driven quantum Hall and quantum spin Hall edge states," *Phys. Rev. B*, vol. 84, no. 23, p. 235436, 2011.

[114] S. Jezouin, F. Parmentier, A. Anthore, U. Gennser, A. Cavanna, Y. Jin, and F. Pierre, "Quantum limit of heat flow across a single electronic channel," *Science*, vol. 342, no. 6158, pp. 601–604, 2013.

[115] X. Qi, T. Hughes, and S. Zhang, "Fractional charge and quantized current in the quantum spin Hall state," *Nature Phys.*, vol. 4, no. 4, pp. 273–276, 2008.

[116] L. Arrachea and F. von Oppen, "Nanomagnet coupled to quantum spin Hall edge: An adiabatic quantum motor," *Physica E*, vol. 74, pp. 596–602, 2015.

[117] F. Hajiloo, P. Alonso, N. Dashti, L. Arrachea, and J. Splettstoesser, "Detailed study of nonlinear cooling with two-terminal configurations of topological edge states," *Phys. Rev. B*, vol. 102, no. 15, p. 155434, 2020.

[118] Q. Meng, S. Vishveshwara, and T. Hughes, "Spin-transfer torque and electric current in helical edge states in quantum spin Hall devices," *Phys. Rev. B*, vol. 90, no. 20, p. 205403, 2014.

[119] R. Sánchez, B. Sothmann, and A. Jordan, "Chiral thermoelectrics with quantum hall edge states," *Phys. Rev. Lett.*, vol. 114, no. 14, p. 146801, 2015.

[120] P. Samuelsson, S. Kheradsoud, and B. Sothmann, "Optimal quantum interference thermoelectric heat engine with edge states," *Phys. Rev. Lett.*, vol. 118, no. 25, p. 256801, 2017.

[121] S. Kheradsoud, N. Dashti, M. Misiorny, P. Potts, J. Splettstoesser, and P. Samuelsson, "Power, efficiency and fluctuations in a quantum point contact as steady-state thermoelectric heat engine," *Entropy*, vol. 21, no. 8, p. 777, 2019.

[122] R. Bustos-Marún, G. Refael, and F. von Oppen, "Adiabatic quantum motors," *Phys. Rev. Lett.*, vol. 111, no. 6, p. 060802, 2013.

[123] R. Whitney, "Most efficient quantum thermoelectric at finite power output," *Phys. Rev. Lett.*, vol. 112, no. 13, p. 130601, 2014.

[124] R. Jackiw and C. Rebbi, "Solitons with fermion number 1/2," *Phys. Rev. D*, vol. 13, no. 12, p. 3398, 1976.

[125] W. Su, J. Schrieffer, and A. Heeger, "Soliton excitations in polyacetylene," *Phys. Rev. B*, vol. 22, no. 4, p. 2099, 1980.

[126] S.-Q. Shen, *Topological insulators*, vol. 174.
Springer, 2012.

[127] J. Goldstone and F. Wilczek, "Fractional Quantum Numbers on Solitons," *Phys. Rev. Lett.*, vol. 47, pp. 986–989, 1981.

[128] X. Qi, T. Hughes, and S. Zhang, "Fractional charge and quantized current in the quantum spin Hall state," *Nat. Phys.*, vol. 4, no. 4, pp. 273–276, 2008.

[129] C. Fleckenstein, N. Traverso Z., and B. Trauzettel, "Chiral anomaly in real space from stable fractional charges at the edge of a quantum spin hall insulator," *Phys. Rev. B*, vol. 94, p. 241406, 2016.

[130] G. Scheunert, O. Heinonen, R. Hardeman, A. Lapicki, M. Gubbins, and R. Bowman, "A review of high magnetic moment thin films for microscale and nanotechnology applications," *Appl. Phys. Rev.*, vol. 3, no. 1, p. 011301, 2016.

[131] T. D. Stanescu, J. Sau, R. Lutchyn, and S. Sarma, "Proximity effect at the superconductor-topological insulator interface," *Phys. Rev. B*, vol. 81, no. 24, p. 241310, 2010.

[132] N. Sedlmayr and A. Levchenko, "Hybridization mechanism of the dual proximity effect in superconductor-topological insulator interfaces," *Solid State Comm.*, vol. 327, p. 114221, 2021.

[133] S. Zhang and B. Trauzettel, "Perfect crossed Andreev reflection in Dirac hybrid junctions in the quantum Hall regime," *Phys. Rev. Lett.*, vol. 122, no. 25, p. 257701, 2019.

[134] A. Michelsen, T. Schmidt, and E. Idrisov, "Current correlations of Cooper-pair tunneling into a quantum Hall system," *Phys. Rev. B*, vol. 102, no. 12, p. 125402, 2020.

[135] F. Ronetti, M. Carrega, D. Ferraro, J. Rech, T. Jonckheere, T. Martin, and M. Sassetti, "Polarized heat current generated by quantum pumping in two-dimensional topological insulators," *Phys. Rev. B*, vol. 95, no. 11, p. 115412, 2017.

[136] F. Ronetti, M. Carrega, and M. Sassetti, "Levitons in helical liquids with Rashba spin-orbit coupling probed by a superconducting contact," *Phys. Rev. Res.*, vol. 2, no. 1, p. 013203, 2020.

[137] L. Fu and C. Kane, "Josephson Current and Noise at a Superconductor/Quantum-Spin-Hall-Superconductor junction," *Phys. Rev. B*, vol. 79, p. 161408, 2009.

[138] L. Jian, D. Pekker, J. Alicea, G. Refael, Y. Oreg, A. Brataas, and F. von Oppen, "Magneto-Josephson Effects in Junctions with Majorana Bound States," *Phys. Rev. B*, vol. 87, p. 075438, 2013.

[139] Q. Meng, V. Shivamoggi, T. Hughes, M. Gilbert, and S. Vishveshwara, "Fractional spin Josephson effect and electrically controlled magnetization in quantum spin Hall edges," *Phys. Rev. B*, vol. 86, no. 16, p. 165110, 2012.

[140] M. Houzet, D. Meyer, J.and Badiane, and L. Glazman, "Dynamics of Majorana states in a topological Josephson junction," *Phys. Rev. Lett.*, vol. 111, no. 4, p. 046401, 2013.

[141] S. Barbarino, R. Fazio, M. Sassetti, and F. Taddei, "Parity dependent Josephson current through a helical Lüttinger liquid," *N. J. of Phys.*, vol. 15, no. 8, p. 085025, 2013.

[142] G. Tkachov and E. Hankiewicz, "Helical Andreev bound states and superconducting Klein tunneling in topological insulator Josephson junctions," *Phys. Rev. B*, vol. 88, no. 7, p. 075401, 2013.

[143] S. Lee, K. Michaeli, J. Alicea, and A. Yacoby, "Revealing topological superconductivity in extended quantum spin Hall Josephson junctions," *Phys. Rev. Lett.*, vol. 113, no. 19, p. 197001, 2014.

[144] F. Crépin, B. Trauzettel, and F. Dolcini, "Signatures of Majorana Bound States in Transport Properties of Hybrid Structures Based on Helical Liquids," *Phys. Rev. B*, vol. 89, p. 205115, 2014.

[145] F. Keidel, P. Burset, and B. Trauzettel, "Tunable hybridization of Majorana bound states at the quantum spin Hall edge," *Phys. Rev. B*, vol. 97, no. 7, p. 075408, 2018.

[146] S. Hart, H. Ren, T. Wagner, P. Leubner, M. Mühlbauer, C. Brüne, H. Buhmann, L. Molenkamp, and A. Yacoby, "Induced superconductivity in the quantum spin Hall edge," *Nature Phys.*, vol. 10, no. 9, pp. 638–643, 2014.

[147] E. Bocquillon, R. Deacon, J. Wiedenmann, P. Leubner, T. Klapwijk, C. Brüne, K. Ishibashi, H. Buhmann, and L. Molenkamp, "Gapless Andreev bound states in the quantum spin Hall insulator HgTe," *Nature Nanotech.*, vol. 12, no. 2, pp. 137–143, 2017.

[148] G. Blasi, F. Taddei, V. Giovannetti, and A. Braggio, "Manipulation of Cooper pair entanglement in hybrid topological Josephson junctions," *Phys. Rev. B*, vol. 99, no. 6, p. 064514, 2019.

[149] H. Ren, F. Pientka, S. Hart, A. Pierce, M. Kosowsky, L. Lunczer, R. Schlereth, B. Scharf, E. Hankiewicz, L. Molenkamp, B. Halperin, and A. Yacobi, "Topological superconductivity in a phase-controlled Josephson junction," *Nature*, vol. 569, no. 7754, pp. 93–98, 2019.

[150] P. Marra, R. Citro, and A. Braggio, "Signatures of topological phase transitions in Josephson current-phase discontinuities," *Phys. Rev. B*, vol. 93, no. 22, p. 220507, 2016.

[151] N. Ziani Traverso, C. Fleckenstein, L. Vigliotti, B. Trauzettel, and M. Sassetti, "From fractional solitons to Majorana fermions in a paradigmatic model of topological superconductivity," *Phys. Rev. B*, vol. 101, no. 19, p. 195303, 2020.

[152] C. Malciu, L. Mazza, and C. Mora, "4 π and 8 π dual Josephson effects induced by symmetry defects," *Phys. Rev. B*, vol. 99, no. 12, p. 125153, 2019.

[153] J. Maciejko, C. Liu, Y. Oreg, X. Qi, C. Wu, and S. Zhang, "Kondo effect in the helical edge liquid of the quantum spin Hall state," *Phys. Rev. Lett.*, vol. 102, no. 25, p. 256803, 2009.

[154] F. Zhang and C. Kane, "Time-reversal-invariant Z_4 fractional Josephson effect," *Phys. Rev. Lett.*, vol. 113, no. 3, p. 036401, 2014.

[155] N. Ziani Traverso, F. Crépin, and B. Trauzettel, "Fractional Wigner crystal in the helical Lüttinger liquid," *Phys. Rev. Lett.*, vol. 115, no. 20, p. 206402, 2015.

[156] W. Su, J. Shrieffer, and A. Heeger, "Soliton excitations in polyacetylene," *Phys. Rev. B*, vol. 22, p. 2099, 1980.

[157] C. Beenakker, "Universal limit of critical-current fluctuations in mesoscopic Josephson junctions," *Phys. Rev. Lett.*, vol. 67, no. 27, p. 3836, 1991.

[158] K. Kajimura and H. Hayakawa, *Advances in Superconductivity III: Proceedings of the 3rd International Symposium on Superconductivity (ISS'90), November 6–9, 1990, Sendai*. Springer Science & Business Media, 2012.

[159] P. Butcher, "Thermal and electrical transport formalism for electronic microstructures with many terminals," *J. Phys.: Condens. Matter*, vol. 2, no. 22, p. 4869, 1990.

[160] J. Pendry, "Quantum limits to the flow of information and entropy," *J. Phys. A: Math. and Gen.*, vol. 16, no. 10, p. 2161, 1983.

[161] J. Bekenstein, "Energy cost of information transfer," *Phys. Rev. Lett.*, vol. 46, no. 10, p. 623, 1981.

[162] J. Bekenstein, "Entropy content and information flow in systems with limited energy," *Phys. Rev. D*, vol. 30, no. 8, p. 1669, 1984.

[163] B. Sothmann and E. Hankiewicz, "Fingerprint of topological Andreev bound states in phase-dependent heat transport," *Phys. Rev. B*, vol. 94, no. 8, p. 081407, 2016.

[164] B. Sothmann, F. Giazotto, and E. Hankiewicz, "High-efficiency thermal switch based on topological Josephson junctions," *New J. Phys.*, vol. 19, no. 2, p. 023056, 2017.

[165] G. Blasi, F. Taddei, L. Arrachea, M. Carrega, and A. Braggio, "Nonlocal thermoelectricity in a topological Andreev interferometer," *Phys. Rev. B*, vol. 102, no. 24, p. 241302, 2020.